Investigation of Acceptor Dopants in ZrNiSn Half-Heusler Materials

Dissertation
zur Erlangung des Grades
"Doktor der Naturwissenschaften"
dem Fachbereich Chemie, Pharmazie und Geowissenschaften
der Johannes Gutenberg-Universität Mainz
vorgelegt von

Jennifer Schmitt
geboren in Frankfurt / Höchst

Mainz 2014

Für meine Familie

Dekan:

1. Berichterstatter:
2. Berichterstatter:

Tag der mündlichen Prüfung: 11.09.2014

Contents

List of Figures

1 List of Symbols and Abbreviations

A	Mobility parameter
α	Seebeck coefficient
c	Absorbtion coefficient
D	Diffusivity
Θ_D	Debey temperature
η	Thernoelectric efficiency
e	elemental charge
E_F	Fermi level
eV	electron Volt
PF	Power factor
I	Electrical current
K	Kelvin
κ	Thermal conductivity
κ_e	Electrical thermal conductivity
κ_L	Lattice thermal conductivity
l	Mean free path
L	Lorenz number
m^*	Effective mass
n	Carrier concentration
N_ν	Band degeneracy
μ	Carrier mobility
ρ	Electrical resistivity
σ	Electrical conductivity
τ	Relaxation time
υ	group velocity
E_g	Energy gap
R_H	Hall coefficient
T	Temperature
V	Voltage
DOS	Density of states
HH	Half-Heusler
PPMS	Physical properties measurement system
SEM	Scanning electron microscopy
TE	Thermoelectric
TM	Transition metal
TEG	Thermoelectric generator
XRD	X-ray diffraction
zT	Material figure of merit
ZT	Device figure of merit

2 Zusammenfassung

Thermoelektrische Generatoren (TEG) sind halbleitende Materialien, die in der Lage sind, thermische Energie in elektrischen Strom umzuwandeln. Damit spielen diese Materialien eine wichtige Rolle in der zukünftigen Abwärmenutzung.

Halb-Heusler (HH) Verbindungen mit der allgemeinen Formel MNiSn (M = Ti, Zr, Hf), sind vielversprechende thermoelektrische Materialien, da sie einen hohen Seebeck-Koeffizienten besitzen, umweltfreundlich sind und einen Kostenvorteil gegenber herkömmlichen thermoelektrischen Materialien besitzen. Ein großer Teil der existierenden Literatur zu HH beschreibt die Charakterisierung von *n*-Typ MNiSn und *p*-Typ MCoSb Verbindungen. Studien zu *p*-Typ MNiSn sind rar. Zur Herstellung hocheffizienter thermoelektrischer Module auf Basis von HH Verbindungen, müssen jedoch hocheffiziente *p*-Typ MNiSn Systeme entwickelt werden, die kompatibel mit den vorhandenen *n*-Typ HH Verbindungen sind.

Die vorliegende Arbeit untersucht Synthesestrategien für hocheffiziente *p*-Typ MNiSn basierende Materialien. Besonders Augenmerk wird hierbei auf die Wirksamkeit von Übergangs- (Sc, La) und Hauptgruppenelemente (Al, Ga, In) als Akzeptoren gelegt, welche auf der Sn-Position und der Zr-Position in ZrNiSn substituiert wurden. Anschließend wurden die thermoelektrischen Eigenschaften dieser neuen Verbindungen untersucht.

Die vielversprechendsten *p*-Typ Materialien entstanden durch eine Dotierung mit Übergangsmetallen, wobei die Substitution von Zr mit Sc den höchsten bis jetzt gemessenen Seebeck-Koeffizienten im ternren MNiSn System ergab. Hall-Effekt- und Bandlücken-Messungen dieser Verbindungen zeigten, dass die hohe Mobilität der Minoritätsladungsträger (hier Elektronen) die Transporteigenschaften bei Temperaturen ber 500K dominieren. Es konnte gezeigt werden, dass dies der Grund ist (hohe Mobilität der Elektronen), weshalb *n*-Typ HH die erfolgreichsten TE Materialien für Hochtemperaturanwendungen sind und das bei *p*-Typen bipolare Effekten zu einer Verminderung der thermoelektrischen Effizienz bei hohen Temperaturen führt. Um die experimentellen Untersuchungen (den Einfluss verschiedener Dopanten auf die thermoelektrischen Eigenschaften von HH-Verbindungen) zu vervollständigen, wurden numerische Lösungen der Boltzmann Transportgleichung verwendet, um die optimale Ladungsträgerkonzentration vorherzusagen, bei der die maximale Effizienz thermoelektrischer Materialien zu finden ist. Die Ergebnisse für *p*-Typen zeigten, dass deren physikalische Daten nicht durch eine einfache parabolische Band Theorie beschrieben werden können, aufgrund von bipolaren Effekten und multiplen Bändern. Das parabolische Band Modell wird häufig für Bulk TE Materialien verwendet. Es ist am genauesten, wenn die Transporteigenschaften von einem einzigen Ladungsträgertyp über einen breiten Temperaturbereich dominiert werden. Da die Transporteigenschaften der *n*-Typ HH nur von einem Ladungsträgertyp dominiert werden, konnte gezeigt werden, dass die Verwendung eines einfachen parabolischen Bändermodells zu einer erfolgreichen Vorhersage der Ladungsträgerkonzentration und Effizienz für *n*-Typ HH Verbindungen führt.

3 Abstract

Thermoelectric generators (TEG) are solid state devices and are able to convert thermal energy directly into electricity and thus could play an important role in waste heat recovery in the near future. Half-Heusler (HH) compounds with the general formula *M*NiSn (M = Ti, Zr, Hf) built a promising class of materials for these applications because of their high Seebeck coefficients, their environmentally friendliness and their cost advantage over conventional thermoelectric materials.

Much of the existing literature on HH deals with thermoelectric characterization of *n*-type *M*NiSn and *p*-type *M*CoSb compounds. Studies on *p*-type *M*NiSn-based HHs are far fewer in number. To fabricate high efficient thermoelectric modules based on HH compounds, high performance *p*-type *M*NiSn systems need to be developed that are compatible with the existing *n*-type HH compounds. This thesis explores synthesis strategies for *p*-type *M*NiSn based compounds. In particular, the efficacy of transition metals (Sc, La) and main group elements (Al, Ga, In) as acceptor dopants on the Sn-site in ZrNiSn, was investigated by evaluating their thermoelectric performance. The most promising *p*-type materials could be achieved with transition metal dopants, where the introduction of Sc on the Zr side, yielded the highest Seebeck coefficient in a ternary NiSn-based HH compound up to this date. Hall effect and band gap measurements of this system showed, that the high mobility of minority carrier electrons dominate the transport properties at temperatures above 500 K. It could be shown that this is the reason, why *n*-type HH are successful TE materials for high temperature applications, and that *p*-types are subjected to bipolar effects which will lead to diminished thermoelectric efficiencies at high temperatures.

To complement the experimental investigations on different metal dopants and their influence on the TE properties of HH compounds, numerical solutions to the Boltzmann transport equation were used to predict the optimum carrier concentration where the maximum TE efficiency occurs for *p*-type HH compounds. The results for *p*-type samples showed that can not be treated within a simple parabolic band model approach, due to bipolar and multi-band effects. The parabolic band model is commonly used for bulk TE materials. It is most accurate when the transport properties are dominated by one single carrier type. Since the transport properties of *n*-type HH are dominated by only one carrier type (high mobility electrons), it could be shown, that the use of a simple parabolic band model lead to a successful prediction of the optimized carrier concentration and thermoelectric efficiency in *n*-type HH compounds.

4 List of Publications

1. **J. Schmitt**, Z.M. Gibbs, G.J. Snyder and C. Felser, Resolving the true band gap of ZrNiSn half-Heusler thermoelectric materials, 2014 accepted

2. J. Krez, **J. Schmitt**, G.J. Snyder, C. Felser, W. Hermes and M. Schwind, Optimization of the carrier concentration on phase-separated half-Heusler compounds, **2014** accepted

3. L. Schoop, L. Mchler, **J. Schmitt**, V. Ksenofontov, S. Medvedev, J. Nuss, F. Casper, M. Jansen, R.J. Cava and C. Felser, Effect of pressure on superconductivity in NaAlSi, *PRB*, 86, 174522, **2012**

4. L. Schoop, S. Medvedev, V. Ksenofontov, A. Williams, T. Palasyuk, I.A. Troyan, **J. Schmitt**, C. Wang, M. Eremets, R.J. Cava and C. Felser Pressure-restored superconductivity in Cu-substituted FeSe, *PRB*, 84, 174505, **2011**

5 Introduction

Efficient energy utilization and means to harvest and store renewable energy sources is the main focus of sustainable energy research today. Our dependence on fossil fuels continues to grow by the day, yet the reserves are diminishing faster than they are being replenished. Over 50% of the energy consumed in the form of fossil fuels is lost in the form of waste heat. Thermoelectrics (TE), a class of materials that has been known for nearly 200 years, can theoretically recover a fraction of the waste heat by converting it to electricity. The thermoelectric effect was first discovered by T.J. Seebeck 1821, when he showed that an electric potential can be produced by heating the junction between two different metals [1]. This physical phenomenon is called the Seebeck effect or thermopower (see Fig. 5.1). If the junction between these two metals A and B is heated to impose a temperature gradient ΔT, the thermal energy is transported by the charge carriers from the hot to the cold side, resulting in a voltage difference ΔV between the ends of the metal.

$$\alpha = \frac{\Delta V}{\Delta T}, \tag{5.1}$$

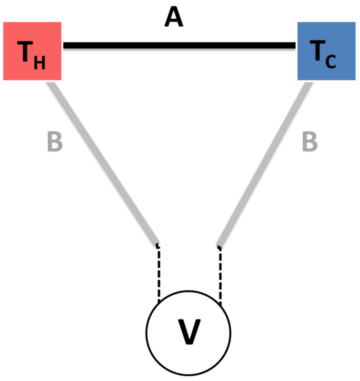

Figure 5.1: Arrangement of two different metals A and B [1]. When the junction between this two materials is heated a voltage will be generated between the ends. This principle is the basis for thermocouples, which are commonly used in temperature measurements.

The second thermoelectric effect was discovered by J. Peltier, who showed that when a current is made to flow through a thermocouple, there is a heating or cooling effect produced at the junction depending on the direction of flow of the current. The relationship between the Seebeck and the Peltier effect is known as the Thomson effect. It describes the mechanism of reversible heating or cooling by applying a current and a temperature gradient [1].

These effects provide the foundation to study the energy conversion efficiencies of TE materials. A quality factor describing the efficiency of an individual TE material is the figure of merit, *zT*.

$$zT = \frac{\alpha^2\sigma}{\kappa}T = \frac{\alpha^2}{\kappa\rho}T, \tag{5.2}$$

where α is the Seebeck coefficient, T is the temperature and κ is the total thermal conductivity (consisting of an electronic and a lattice contribution). According to this equation, high TE efficiencies are achieved for high Seebeck coefficients and electrical conductivities and low thermal conductivities. The influence of the individual transport propertieson the thermoelectric efficiency will be discussed in detail later.

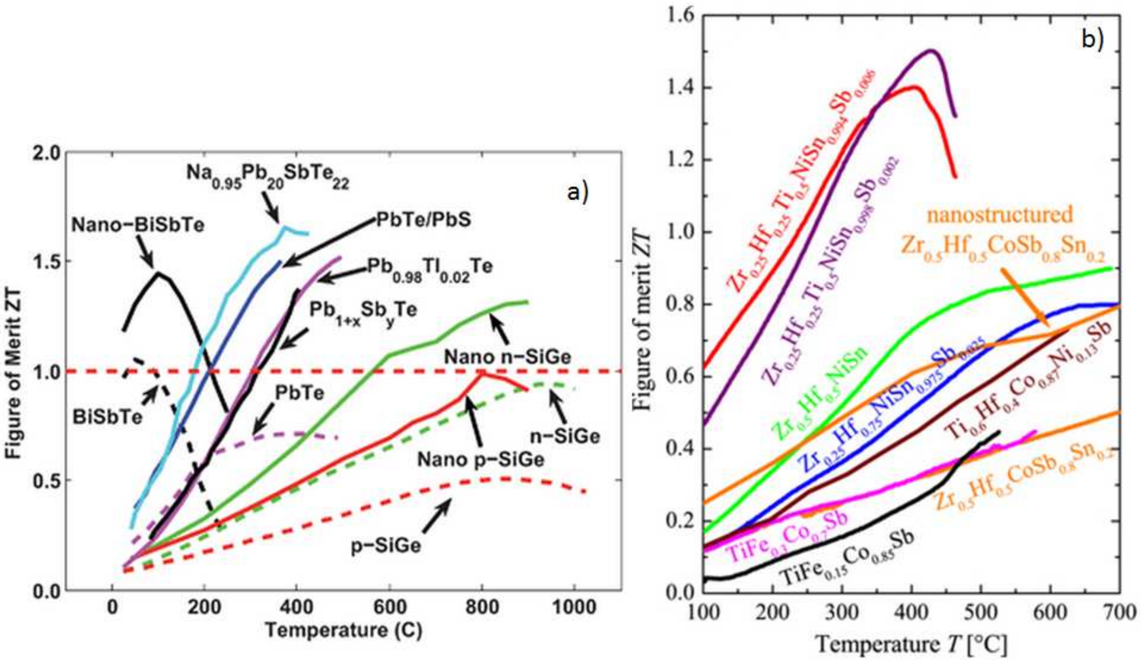

Figure 5.2: Overview of *zT versus* temperature for different state of the art thermoelectric materials [2] a) and a comparison of different state of the art half-Heusler materials [3] b). Generally zT is reaching its maximum at different temperatures for different materials, so these materials find applications in various temperature ranges.

T.J. Seebeck used metals to exploit the high mobilities of carriers and, consequently, the generated voltage. However, due to high carrier concentrations, metals possess high electrical conductivities and low Seebeck coefficients (see Eq. 5.7), which consequently leads to low figure of merits, *zT* (Eq. 5.3). As a result, TE research stagnated until Ioffe realized that doped semiconductors show more promising TE properties [4, 5]. His research opened the pathway for the investigation of whole new material classes and their TE properties like Skutterudites, Clathrates, Zintls, Chalcogenides and half-Heusler (HH) compounds [1, 5, 6]. From all these materials, the most promising candidates for thermoelectric applications are narrow band gap semiconductors. A comparison of these materials and their *zTs* are shown in Fig. 5.2 a) and b). The figure of merit for a single material does not say much about the performance of a TE device, since an array of many *p*- and *n*-type TE couples is used [7], shown in Fig. 5.3. The matching of the thermal and mechanical properties of these dissimilar materials is critical for the successful operation of a TEG. The Seebeck effect and the device efficiency, *ZT*, is exploited in such devices where a temperature gradient results in a diffusion of carriers from hot to cold side, resulting in an electrical potential ΔV that could be used to drive a current through a load.

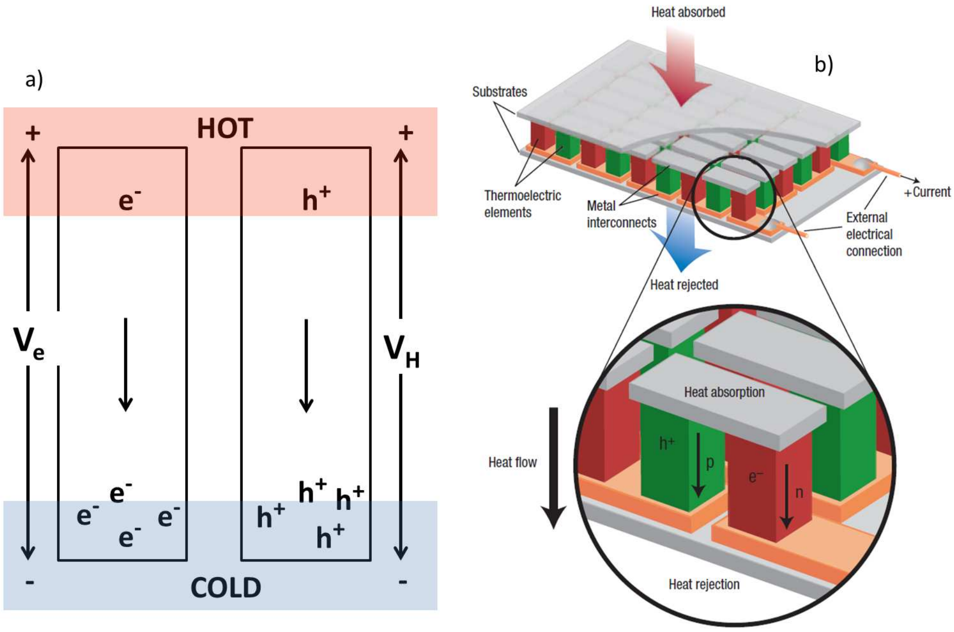

Figure 5.3: Carrier diffusion from hot to cold side for an arbitary *p*- and *n*-type material a), resulting in an electrostatic potential at the cold end. In b) a sample thermoelectric module is shown, where the thermocouples are connected electrically in series and thermally in parallel. These devices have reliably provided auxiliary power in deep space missions by NASA and JPL *Voyager* [8].

The device efficiency depends not just on the power factor, but also the temperature dependence of the Seebeck coefficient, electrical and thermal conductivity. To distinguish between the material performance *zT*, *ZT* is used to describe the device performance [9]. For a TEG this means:

$$\eta = \frac{\Delta T}{T_h} \cdot \frac{\sqrt{1+ZT}-1}{\sqrt{1+ZT}+\frac{T_c}{T_h}}, \tag{5.3}$$

where T_h and T_c denote the temperature of the hot and cold side of the device respectively. The efficiency of a TEG is limited by the Carnot efficiency. One method to increase the module efficiency η is by segmenting the TE legs [10]. This takes advantage of the fact that different TE materials exhibit their maximum in their TE efficiency at different operating temperatures, thus broadening the temperature range of applicability. Another method is to improve the inherent thermoelectric properties of the material, which forms the crux of Sec. 5.2.

5.1 Thermoelectric Properties

5.1.1 Electronic Properties

Electrons are involved in both charge and heat transport and hence play a key role in determining the Seebeck coefficient and electrical conductivity. The availability of charge carriers is determined by the electronic band gap. In metals a large number of carriers is available for electronic conduction ($> 10^{22}$ cm^{-3}), thus the electrical conductivity is high. The electrical conductivity is a function of the carrier concentration n and the carrier mobility μ. Thus, the same conductivity can come from a sample with a high carrier mobility, but a same number of carriers, or a large number of carriers with small mobilities.

$$\sigma = \frac{1}{\rho} = ne\mu, \tag{5.4}$$

$$n_H = \frac{1}{R_H}, \tag{5.5}$$

with e being the elementary charge, σ the electrical conductivity and ρ the electrical resistivity. For semiconductors, carriers need to be excited across the band gap, leading to lower carrier concentrations E_g (10^{18}-10^{21} cm^{-3}) and lower conductivity values compared to metals (see Eq. 5.4). In order to reach high electrical conductivities in these materials the mobility of the charge carriers and the carrier concentration need to be high. Both properties are defined by the electronic structure of the material.

The relationship between electrical conductivity and Seebeck coefficient (Eq. 5.7) can be derived from the Mott equation [11]:

$$\alpha = \frac{\pi^2 k_B^2}{3e} T \left\{ \frac{d\left[ln(\sigma(E))\right]}{dE} \right\}_{E=E_F}, \tag{5.6}$$

where σ(E) is the energy dependent electrical conductivity and k_B the Boltzmann constant. For degenerately doped semiconductors, the Seebeck coefficient can be expressed as:

$$\alpha = \frac{8\pi^2 k_B^2}{3eh^2} m_{DOS}^* T \left(\frac{\pi}{3n}\right)^{2/3}, \tag{5.7}$$

with h being the Planck constant and m_{DOS}^* the density of states (DOS) effective mass. Eq. 5.7 shows that the Seebeck coefficient is not only proportional to $1/n$ but also depends linearly on the effective mass m^*. Where a large effective mass results in high Seebeck coefficients, but low electrical conductivities (see Eq. 5.4) and *vice versa* for high carrier densities n.

The carrier mobility [1] depends on the band effective mass m^* and the relaxation time τ roughly as:

$$\mu = \frac{e\tau}{m^*}. \tag{5.8}$$

An estimate of m^* can be obtained from *ab-initio* calculations of the electronic band structure [12] or from experimental Seebeck and Hall measurements (usually by applying the parabolic band approximation [13]). Since the effective mass varies inversely with the curvature of the bands, a high effective mass is the result of shallow or flat bands, whereas a small effective mass is typical for highly dispersed bands. Thus, a balance between the carrier concentration, to maintain high Seebeck coefficients, electrical conductivities and the carrier effective mass (influencing the carrier mobility) must be found. Unlike for the carrier concentration, the optimal m^* to achieve high electrical conductivity, but also high Seebeck coefficients [9], is not known. It is fundamental to enhance the efficiency of thermoelectric materials by optimizing a variety of conflicting parameters. Fig. 5.5 illustrates the behavior of the different parameters as a function of carrier concentration. Optimized materials usually show carrier concentration in the range of 10^{19} - 10^{21} cm^{-3} carriers. This range is in between the carrier density for intrinsic semiconductors and metals. The power factor optimizes at higher carrier concentrations than the figure of merit (see Fig. 5.6). PF is the product of the Seebeck coefficient α and the electrical conductivity σ:

$$PF = \alpha^2 \sigma. \tag{5.9}$$

5.1.2 Phononic Properties

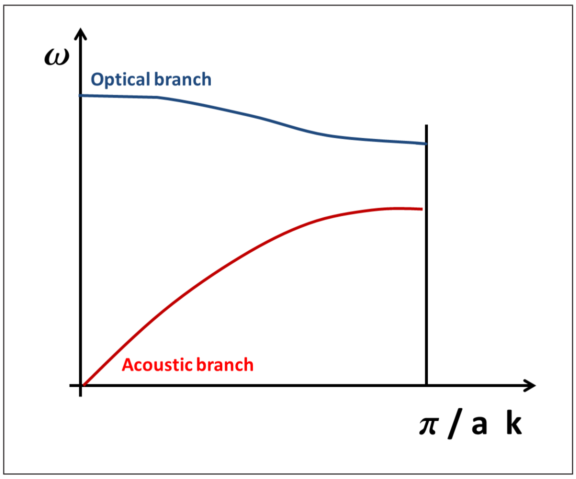

Figure 5.4: Schematic phonon dispersion curve for a given direction k in a diatomic case. The allowed frquencies are split into an optical and an acoustic branch. The gap between the two branches depends on the mass difference between the atoms. If the atoms are equal in mass the branches join each other.

Heat can be transported in a solid through electronic carriers (electrons or holes) or through lattice vibrations (phonons). The total conductivity is the sum of these two contributions,

$$\kappa = \kappa_e + \kappa_L, \tag{5.10}$$

where subscripts e and L denote the lattice and thermal contributions. As mentioned earlier, κ_e is strongly correlated to the electrical conductivity and its dependence is described by the Wiedemann-Franz-law [9]:

$$\kappa_e = L\sigma T = ne\mu LT, \tag{5.11}$$

with L being the Lorenz number with a value of $2.44 \cdot 10^{-8}$ WΩ/K^2 for metals and degenerately doped semiconductors [1]. For non-degenerately doped semiconductors, this value can differ because L is not a constant and depends on the temperature and carrier concentration. Exact knowledge of L is necessary for accurate determination of κ_L from κ_e and κ [9].

Heat is predominantly carried by lattice vibrations of various frequencies. Depending on their frequency, these phonons can be categorized into low frequency (acoustic/harmonic) and high frequency (optical/anharmonic) phonons (Fig. 5.4). In a crystal with N atoms per unit cell, there are

$3N$ acoustic and $3N-3$ optical branches [1, 14].

For the understanding of the heat transfer in solids, the lattice vibrations are treated as a gas of phonons and can be described by the Debye equation for the heat tranfer in gases, which is based on classical kinetic gas theory [15], thus the lattice thermal conductivity can be shown to be

$$\kappa_L = \frac{1}{3} C_v \nu l, \tag{5.12}$$

with ν being the group velocity, l being the mean free path and C$_v$ being the heat capacity. The dependence of κ_L on the group velocity of the phonons is rather complicated due to a broad spectrum of available phonons. For example, high energy optical phonons have low group velocities and conduct heat less effectively [1, 14], whereas acoustic phonons dominate the phonon heat conduction as they possess a greater energy dispersion, resulting in a much greater distribution of the phonon velocieties.

5.2 Optimum Material Properties

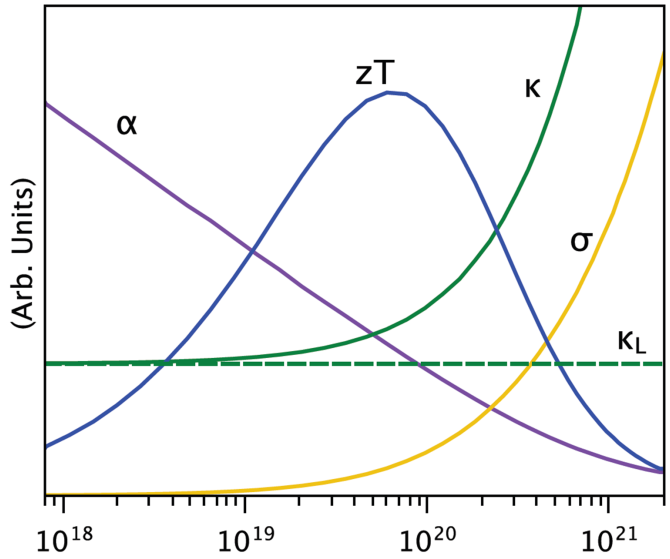

Figure 5.5: The control of the carrier concentration can lead to an optimization of the thermoelectric performance [16]. This involves a compromise between conflicting thermoelectric parameters shown here.

High TE efficiency can be achieved in semiconductors with a sufficiently high energy gap E_g ($>$ 0.25 eV), where the carrier concentration can be tailored through doping. According to Eq. 5.3 a high figure of merit, zT, is achieved through a compromise between the Seebeck coefficient α, electrical conductivity σ and the thermal conductivity κ [9]. For any given material, these parameters are coupled by their dependence on the carrier concentration (see Fig. 5.5). Hence, controlling the carrier concentration is very important when trying to control the transport properties in a thermoelectric material. If the carrier concentration n is too large, the Seebeck coefficient will be diminished (Eq. 5.7) and the electronic part of the thermal conductivity will be increased resulting in a higher total thermal conductivity and ultimately, low zT values. As can bee seen from Fig. 5.6, the maximum figure of merit and power factor increase with increasing temperature and vary with the carrier concentration. For materials with small E_g the carrier concentration is temperature dependent, leading to bipolar conduction at elevated temperatures, leading to a diminished Seebeck coefficient and an increase in the thermal conductivity. Thus, a careful adjustment of the thermoelectric properties is necessary to achieve the highest material performance in the desired temperature range.

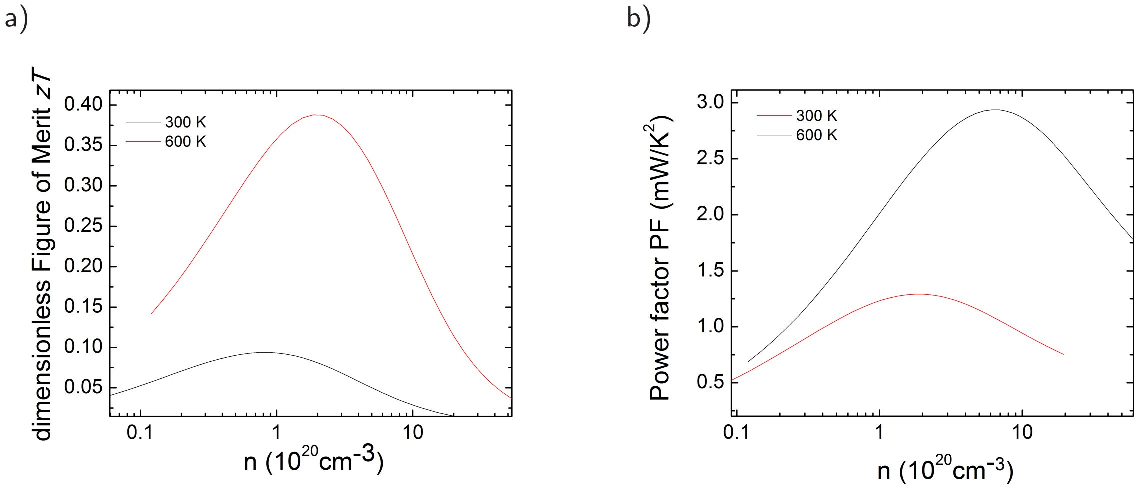

Figure 5.6: Dependence of zT and PF as a function of the carrier concentration n : a) dimensionless figure of merit zT and b) the powerfactor PF both exemplarily for n-type ZrNiSn at different temperatures.

From Eq. 5.4, it is evident that improving both carrier concentration and mobility will lead to high electrical conductivities. In the case of *M*NiSn HH, Krez *et al.* [17] reported that metallic Nb inclusions increase carrier concentration and hence, the electrical conductivity. The authors were able to show that the increased σ also leads to an overall improvement of the TE performance in the *M*NiSn-based HH systes.

Often the carrier concentration is influenced through introduction of dopants into the lattice

[7, 18, 19, 17, 20, 21, 22, 23] or through the size of the band gap, in which small band gap semiconductor show an increase in carrier concentration at high temperatures, resulting from bipolar contributions of different carriers. For materials containing both electron and holes the Seebeck coefficient is calculated as the weighted average of the electrical conductivity of each species:

$$\alpha = \frac{\alpha_n \sigma_n + \alpha_p \sigma_p}{\sigma_n + \sigma_p}, \tag{5.13}$$

where α is the effective Seebeck coefficient, $\alpha_{n,p}$ are the Seebeck coefficient for electrons/holes and the $\sigma_{n,p}$ is the electrical conductivity for the electrons/holes. For semiconductors with bipolar effects, where both α_n and α_p are large, the resulting net Seebeck coefficient will be lower than for semiconductors with one carrier type. Thus, materials with band gaps $>$ 0.5 eV are used for high temperature applications due to the late onset of bipolar effects, while materials with small band gaps will find use for cooling purposes, e.g. Bi_2Te_3 [24].

Aside from the obvious carrier effects, dopants also influence the electronic band structure by introducing resonant states at the band edge [11, 22, 25, 26, 27] or by shifting the Fermi energy. Fig. 5.7 shows the influence of 10 % donor or acceptor dopand concentration on NiSn-based HH compounds. Depending on the sublattice where the substitution takes place, the transport properties will be affected differently, due to the different origin of the electrons. For HH it is assumed that the subsitution on the *M*-site with a TM influences the TE properties the most, determined by the same origin of the electrons and the fact that M = Ti/Zr/Hf introduce additional features, like resonant states, at the band edges [27, 28]. These states are held responsible for the large Seebeck coefficients in half-Heuslers.

The widely employed route for improving zT is reduction of the total thermal conductivity. From Eq. 5.11, it can be expected that a change in κ_e will trigger a change in σ and vice versa. As a result, it is preferable to aim for a reduction in the lattice contribution. Here the model proposed by Slack *et al.* [29] illustrates a way for an efficient reduction of the total thermal conductivity. His idea was to develop a phonon-glass-electron-crystal (PGEC), with the thermal properties of a glass-like material and the electrical properties of a crystal. With this approach, only the phonons are scattered while the electrons are unaffected. This has been demonstrated successfully in materials with complex structures like Zintls [16], Skutterudites [30] and Clathrates [31].

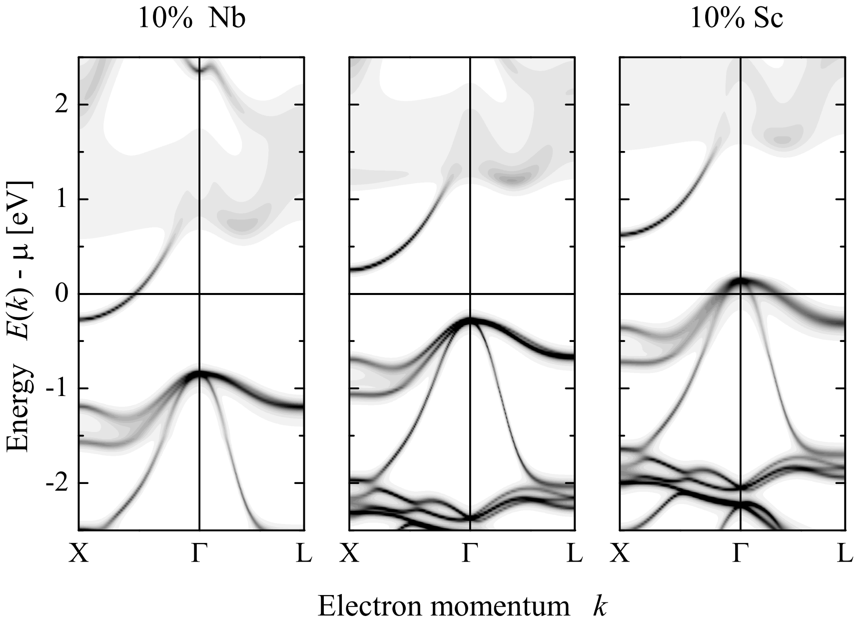

Figure 5.7: T*Ab-initio* calculations performed for an exemplary NiSn-based HH compound, substituted with 10 % Nb or Sc for M = Ti, Zr, Hf. Depending on the dopant the Fermi energy gets shifted either into the conduction or into the valence band compared to the undoped compound. The *ab-initio* calculations were provided by Dr. G. Fecher from the Max-Planck Institute for Chemical Physics of Solids.

5.3 Half-Heusler Compounds

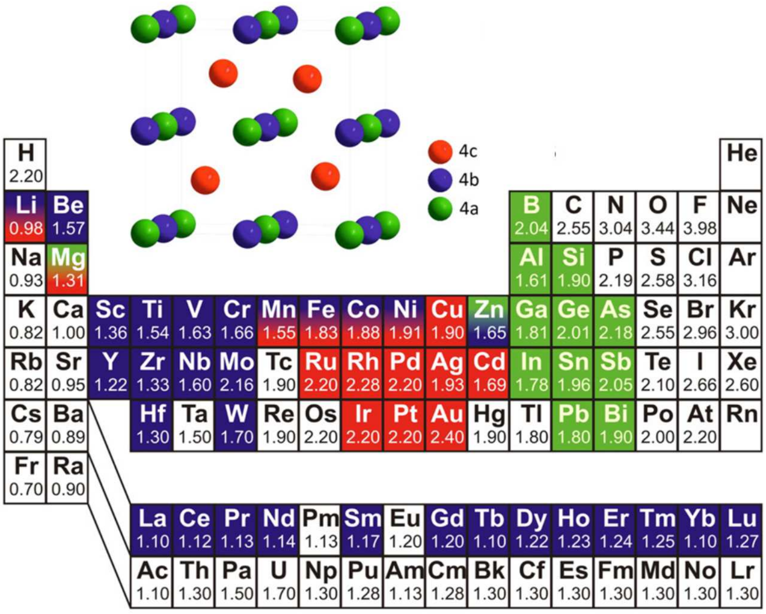

Figure 5.8: Periodic table of elements and the cubic $C1_b$ structure of *XYZ* half-Heusler compounds. As can be seen from the indicated colors, half-Heuslers can be formed through various combinations of different elements [21].

HH fulfill a lot of the criteria for promising thermoelectric materials - high Seebeck coefficients, electrical conductivities and an energy gap, which can be tailored through compositional changes[32]. Outside thermoelectrics, HH generate a lot of interest in research fields such as magnetocalorics, spintronic applications, shape-memory alloys and topological insulators as well [21].

HHs are ternary intermetallics with a 1:1:1 stoichiometry and crystallize in a cubic $C1_b$ (space-group 216) structure. Their structure consists of three interpenetrating sublattices *X*, *Y* and *Z*, where the *X* atoms (Ni/Co) correspond to the Wyckoff position 4c, the *Y* atoms (Sn/Sb) to 4b and the Z atoms (Ti, Zr, Hf) to 4a [21]. The Wyckoff position 4d is vacant in the case of HH, if 4d is occupied by Ni, than they are called full-Heusler alloys. It should be noted that each of these lattice sites can be manipulated independently, which provides an excellent opportunity to influence the electronic and thermal transport properties in these materials. Fig. 5.8 shows a typical HH structure and the periodic table, highlighting in a colored schematic the numerous possibilities to combine transition and main group elements to form 8 or 18 valence electron (VE) HH alloys.

All HH compounds can be derived from a *Zinkblende*-sublattice, in which the octahedral lattice

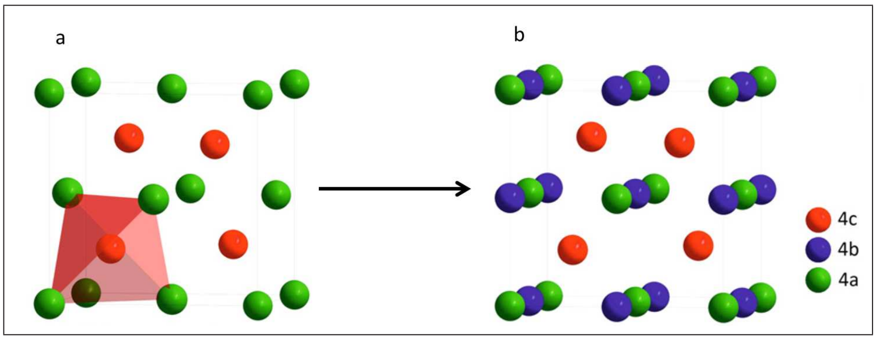

Figure 5.9: The cubic half-Heusler structure b) can be derived from a *Zinkblende*-substructure a) built from Y and Z and by filling the octahedral voids with X atoms [21].

sides are occupied by the most electropositive element X (Fig. 5.9). The bonding interaction within this *Zinkblende*-substructure is of covalent nature and formed by the elements with the smallest difference in electronegativity, usually Y and Z. The greater the difference in electronegativity within this substructure (Y and Z), the bigger the band gap will be [32]. The band gap arises from a repulsion of the Ni/Co *d*-orbitals and the M *d*-orbitals [33]. So by combining different elements, the band gap can be tuned from very small values like in *M*NiSn HH (0.1 eV) up to 4 eV in LiMgN (see Fig. 5.10).

The band gap is an essential factor when investigating the thermoelectric properties of a material. Small band gap semiconductors have the disadvantage that at high enough temperature the excitation of minority carriers will lead to a disruption of the thermoelectric properties.

The band gap can not only be influenced by the constituent elements, but also by the structural order of the atoms. It is believed that a structural disorder is the reasons for the discrepancy between the band gaps for ZrNiSn from *ab-initio* calculation (0.5 eV) [28] and the measured band gaps evaluated by Aliev *et al.* [34] from high temperature resistivity measurements (0.15 eV). The indirect band gap in HH occurs between the Γ and X-point (Fig. 5.11). Anti-side defects between Ni (4c) and the vacancy site (4d), seem to be the reason for the theoretically overestimated band gaps in NiSn-based systems [12, 35]. Not only anti-site defects will influence the size of the band gap but also the carrier density and mobility. These Ni defect states are believed to be the reason that ZrNiSn is an intrinsic *n*-type material and its high carrier density of $2.1*10^{19}$ cm^{-3} [18]. A reduction of this structural disorder is possible through a long term heat treatment.

The choice of elements is decisive not only for the band gap (see Fig. 5.10), but also the thermoelectric properties, since each of the sublattices can be manipulated individually. Doping in the case of HH involves substitution of an element with one valence electron more or less than the

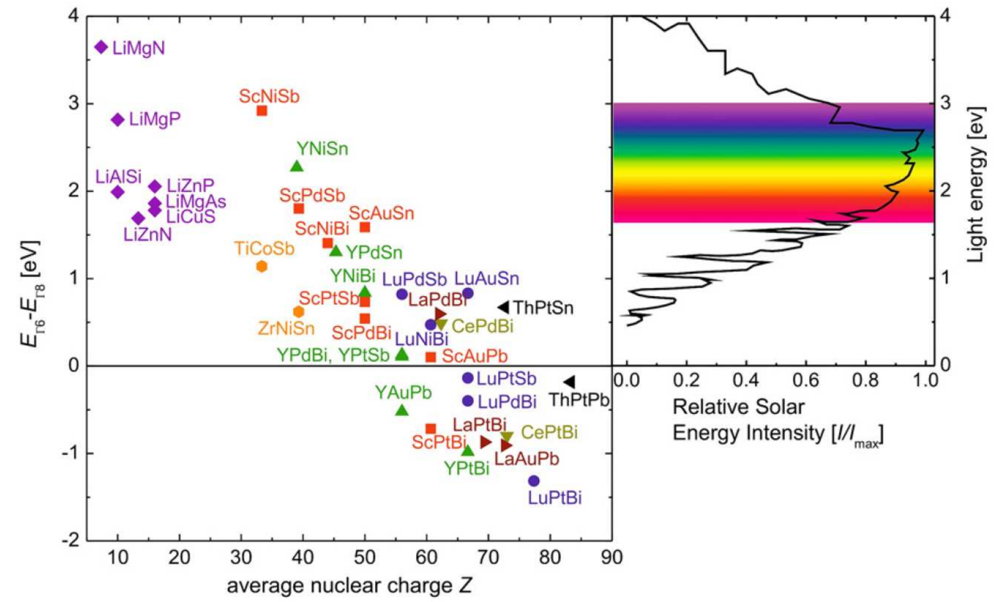

Figure 5.10: Band gaps of various half-Heusler as a function of their average nuclear charge. The solar energy spectrum is shown as well to emphasize the tunability of the band gaps [32].

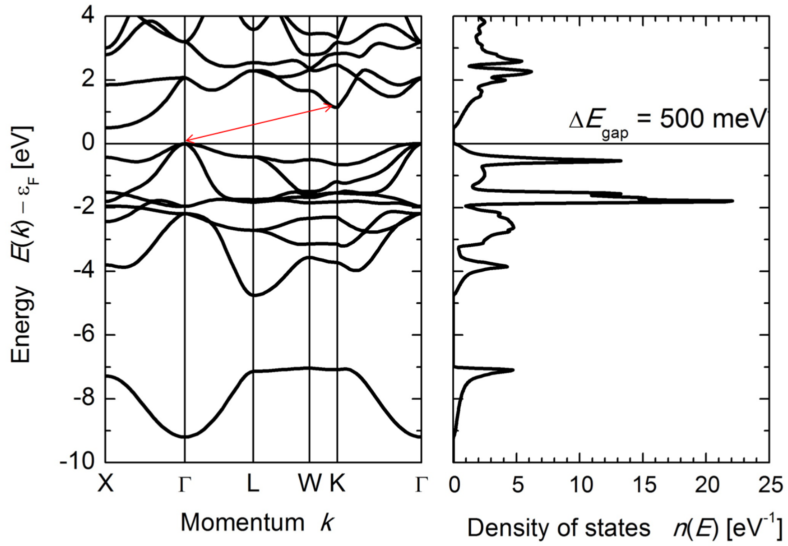

Figure 5.11: Calculated band structure $E(k)$ and density of states $n(E)$ for ordered ZrNiSn. The band gap estimated from the *ab-initio calculations* is found to be 0.5 eV. The red line is an indicator for the indirect band gap. The *ab-initio* calculations were provided by Dr. G. Fecher from the Max-Planck Institute for Chemical Physics of Solids.

original one. Other methods are either isoelectronic alloying, for example on the *M* site to increase mass-fluctuations, which lowers the thermal conductivity [19, 23, 36], or introduction of impurity atoms. In this context impurity doping refers to donor or acceptor elements being introduced into the pure system. Donor impurities (i.e. elements possessing more valence electrons (VE) than the parent atom), will create donor levels just below the conduction band (CB) and shift the Fermi level towards toward higher energies. Since the energy barrier for thermal excitation is substantially lowered, this causes an increase in the carrier density, which leads to a shift of the absolute Seebeck coefficient to higher temperatures.

Impurity atoms with lesser valence electrons tend to have empty states just above the valence band of the host material. As a result, electrons from the valence band populate the acceptor states, giving rise to holes as charge carriers in the former. The hole mobility tends to be typically lower than that of the electrons. Lower mobilities will result in a lower electrical conductivity for *p*-type materials (see Eq. 5.4). Contrary to the introduction of donor impurities, acceptor impurities will lead to a shift of the Fermi level to lower energies. As thermoelectric HH are constituted of three lattices, doping for instance on the Sn site by an acceptor impurity will not have the same effect as the substitution of an acceptor impurity on the *M*-site. This can be understood when looking at the band structure of ZrNiSn Fig. 5.11. A lower valence impurity at the *M*-site will generate acceptor levels above the valence band and can strongly interact with the VB, which has mainly *M* *d*-character, while the substitution on the Sn site, will have lesser impact, due to the fact that the Sn *p*-orbitals lie far below the Fermi energy (below -6 eV) and hence do not participate in conduction. It can be speculated that acceptor doping on the *M*-site will have a greater impact and should result in a good *p*-type material. However, as mentioned before, the *M*NiSn system is a strong intrinsic *n*-type material, as a result doping with small amounts of donor impurities should have a huge impact on the thermoelectric transport properties, like increasing the electrical conductivity significantly [18, 37] as well as the carrier concentration, thus resulting in an improved thermoelectric efficiency, zT, whereas doping with acceptor elements would need larger doping amounts, as the strongly intrinsic *n*-type properties caused by Ni disorder [38] need to be compensated to yield a *p*-type material.

5.4 Motivation

During the past decades the most intensively HH system study for thermoelectric applications were the *M*NiSn and the *M*CoSb system. Both ternary systems exhibit excellent transport properties, but the drawback is their relatively high thermal conductivity, which can be as high as 10 W/Km [18] at room temperature (RT). Yet these systems provide the perfect base for fundamental studies for a basic understanding of the influence of dopants on the thermoelectric transport properties. For example isoelectronic alloying on the *M* site showed a significant reduction of the thermal conductivity [22, 36, 39, 40, 41]. It was later found, that these multi-component HH systems show an intrinsic phase-separation into two HH phases, resulting in extremely high thermoelectric efficiencies [17, 36]. Therefore, the basic studies of site substitutions in ternary HH can help to further improve these phase-separated HHs. The *M*NiSn solid solution is the most intensively studied *n*-type half-Heusler system [7, 17, 18, 19, 20, 21, 22, 23].

Despite the enormous amount of experimental work toward developing high efficient *n*-type HH; studies on efficient *p*-types are far fewer in number. Generally, good *p*-type materials for operation at high temperatures are in particular short supply. The currently used *p*-type thermoelectric materials for power generation applications are based on SiGe-alloys [42]. In order to be compatible with *n*-type HH materials, which are currently investigated for thermoelectric modules [43] a suitable *p*-type in the *M*NiSn system needs to be explored. Some work has already been done to this end; Xie *et al.* [44] studied the substitutin of Ni by Co and demonstrated that a conversion from *n*- to *p*-type behavior for the *M*NiSn system could be achieved. Likewise Horyn' *et al.* [45] studied the effects of Sc substitution for Ti or Zr up to 350 K, which showed a promising positive Seebeck coefficient at room temperature. Most of the aforementioned work focused on the substitution at the *M*- or Ni-site with transition metals (TM).

The aim of this work is to extend the existing studies and perform a comprehensive investigation of possible *p*-type *M*NiSn HH systems through the investigation of different dopants on the *M*- and Sn-site, and subsequently, characterize the thermoelectric properties (see Fig. 5.12). Many of these aformentioned studies are based on experimental investigations on the influence of different dopants on the thermoelectric properties in half-Heuslers. Here, aside from the experimental investigation of different p-type dopants a simple parabolic dispersion relationship (free electron behavior) was used for the prediction of the optimum carrier concentration in p-type HHs. The results were then applied to phase-separated HH. For the improvement of the thermoelectric efficiency of these phase-separated HH the electron doping in the *n*-type $\mathrm{Ti}_{0.3-x}\mathrm{Zr}_{0.35}\mathrm{Hf}_{0.35}\mathrm{NiSn}$ compound was investigated, by developing an universal transport theory for these compounds. The obtained results prove the applicability of the used transport theory and is in good agreement with other results found for HH in the literature. The universal transport theory provides a guideline and a new starting point for future improvements whether by further engineering of the phase separation or by band structure engineering. It was used to compare various *n*- and *p*-type HH compounds found it the literature and to identify the optimum carrier concentration in these systems. Here the both most commonly used HH systems, the *M*NiSn and the *M*CoSb system, were compared.

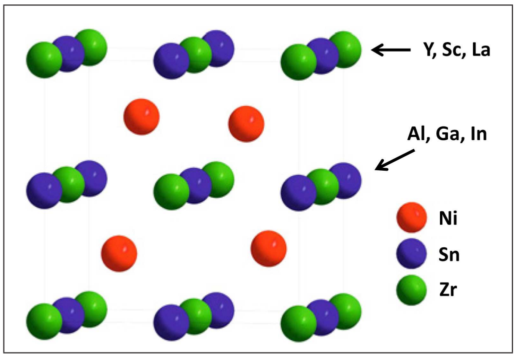

Figure 5.12: Manipulation of the different sublattices through either substitution of Y, Sc or La for Zr or through subsitution of Al, In or Ga for Sn.

6 Experimental Methods

6.1 Synthesis

HHs are composed of many elements with high melting points: Titanium 1168 °C, Zirconium 1852 °C, Hafnium 2227 °C, Nickel 1453 °C, Scandium 1541 °C, Yttrium 1523 °C and Lanthanum 920 °C. The presence of many elements with a range of different melting temperatures makes it inherently difficult to synthesize them through mechanical alloying and achieve compositional homogeneity. As a consequence, these compounds were prepared by arc melting stoichiometric amounts of the elements in Ti-gettered argon atmosphere [40, 46] (Fig. 6.1).For homogeneity the samples were flipped and crushed several times. Other methods used for the synthesis of HH are induction melting [19, 47], optical floating zone melting [48] and levitation melting [35].

For the preparation of the samples, discussed in this thesis, stoichiometric amounts the elements were weighted and arc melted 5 times within an argon atmosphere (Fig. 6.1). After each melting process the samples were weighted again, crushed and remelted to ensure homogeneity. A heat treatment after the alloying process was carried out to improve the structural order in these alloys. Therefore, the molten ingots where put into sealed quartz tubes and annealed at 950 °C for 7 days. After the thermal treatment the quartz tubes were quenched in ice water and prepared for further analysis.

Figure 6.1: Home made arcmelter set up with a water cooled copper plate including four indentations for three samples and a titanium sponge. The Ti sponge was used as oxygen gater during the melting process.

6.2 Characterization

The samples were characterized by powder *X*-ray diffraction *XRD* at room temperature, to examine the samples composition and purity. All *XRD* scans were performed on a D500 diffractometer by Siemens using *Cu* K_α radiation. To examine the sample's purity and structural order a Rietveld analysis of the obtained *XRD* patterns was performed using FullProf software.

Electronic transport measurements at low temperatures were carried out using a physical property measurement system (PPMS) from Quantum Design. Samples were cut and polished into bars measuring $\approx 2\times2\times10$ mm^3. Gold-coated copper contacts were attached with a two component silver epoxy paste (see Fig. 6.2). The measurements of the thermal conductivity, electrical resistivity and Seebeck coefficient were done simultaneously using the thermal transport option (TTO) of the PPMS with a four-point method, under a vacuum of $\approx 10^{-4}$ mbar in the temperature range from 10 - 350 K with temperatue steps of 5 K (see Fig. 6.2).

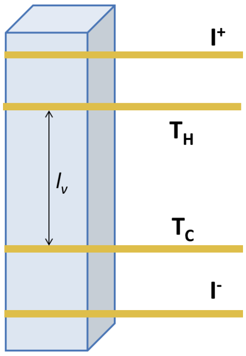

Figure 6.2: Common lead arrangement for bar shaped samples for PPMS measurements. A temperature gradient is applied between the top and the bottom of the sample and the voltage is measured between the middle contacts.

As illustrated in Fig. 6.2, the top contact (I_+) supplies the current needed for the measurement and the bottom contact (I_-) closes the circuit. The voltage is measured between the 2 middle contacts and is determined by:

$$\rho = R\frac{A}{l} = \frac{UA}{Il}, \tag{6.1}$$

where *R* as the resistance, *A* the cross-section area of the sample, *l* the lead-separation between T_H and T_C, *U* the voltage measured between T_H and T_C and *I* the applied current. For the determination of the Seebeck coefficient a temperature gradient is applied between I_+ and I_-, whereas I_+ is connected to a heater and T_H and T_C are connected to thermocouples for the temperature control.

The **high temperature thermal transport properties** were determined under a dynamic vacuum from room temperature up to 850 K. All high temperature measurements where done in Dr. Jeffery Synder's laboratory at Caltech and the set up is shown in Fig. 6.3.

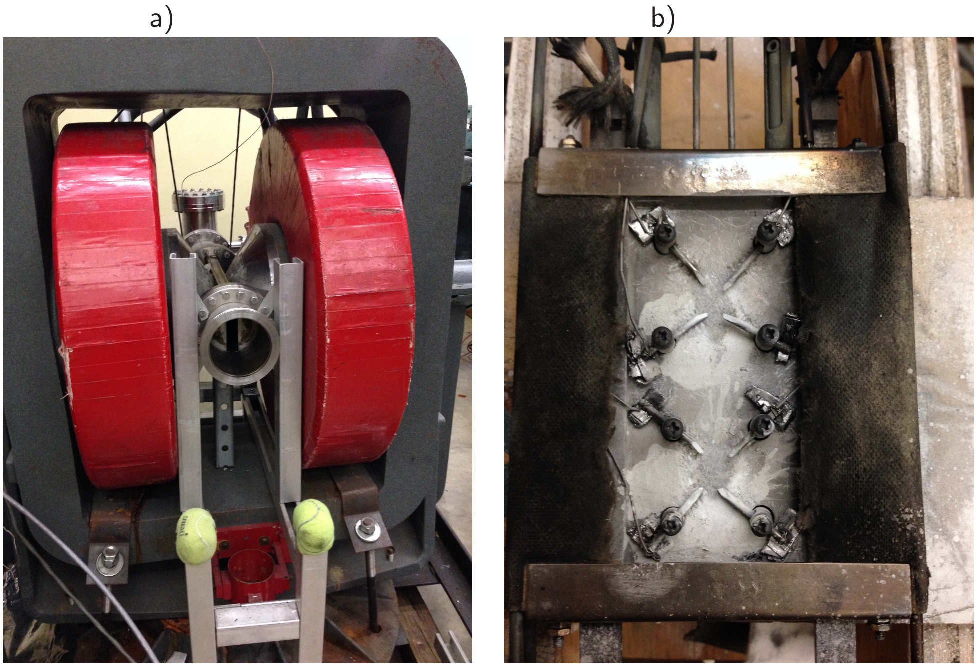

Figure 6.3: Hall system a) with the red magnet and the vacuum chamber, where the sample holder gets iserted after the samples are mounted onto the sample holder b). With this holder, it is possible to measure two samples simultaneously with the Van der Pauw technique. All Hall measurments where done at the California Institute of Technology, Pasadena, USA.

The Hall effect and the electrical resistivity were measured with the Van der Pauw technique using pressure-assisted niobium contacts [49] in a ± 2 Tesla field. From the Hall coefficient R_H the carrier concentration was calculated assuming a single carrier type:

$$n_H = -\frac{1}{eR_H}. \tag{6.2}$$

The Hall mobility was determined from the measured electrical conductivity and the carrier concentration:

$$\mu_H = \sigma e n_H. \tag{6.3}$$

The Seebeck coefficient α was calculated from the slope of V versus T measurement using

Chromel-Niobium thermocouples and by oscillating the temperature gradient in an intervall of 10 K [50] while maintaining a constant average temperature at each temperature point. The measurement set up, together with the resistive heaters is shown in Fig. 6.4. No special geometry is needed for the measurement, except two parallel surfaces. The disc shaped samples were placed between the two boron-nitride heating elements, with the thermocouples touching each side of the sample. To prevent any reaction of the thermocouples with the the sample, each of the sides were covered with graphite foil.

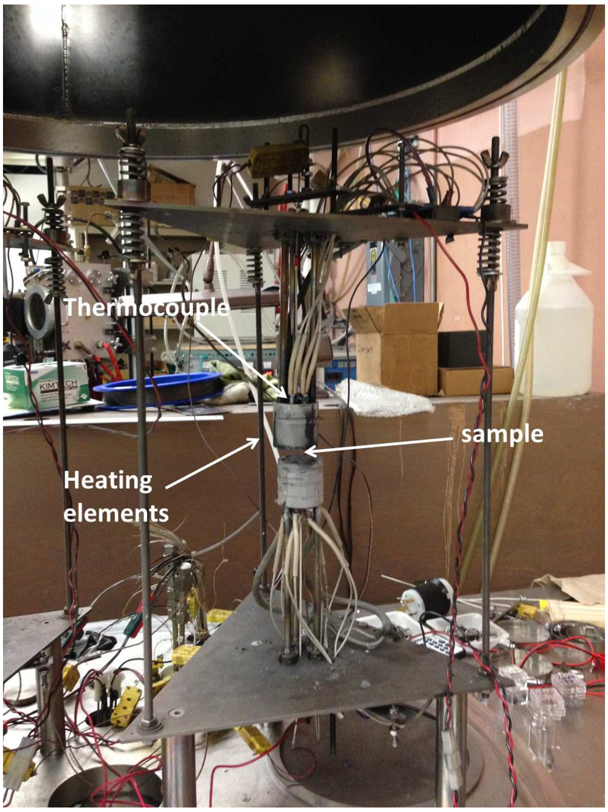

Figure 6.4: Seebeck system at the California Institute of Technology (Caltech), Pasadena, USA.

The **thermal conductivity measurements** were done using a Netzsch laser flash diffusivity instrument (LFA 457) with a Pyroceram standard. All the samples were coated with a thin layer of graphite to minimize emissivity errors. The data was analyzed using a Cowan model with pulse correction. The thermal conductivity κ was calculated by employing following relationship:

$$\kappa = DC_pd, \tag{6.4}$$

where D is thermal diffusivity, C_p is the heat capacity, and d is density.The heat capacity was estimated using the Dulong-Petit method and the sample densities were calculated from the molar mass and the lattice parameter for each sample obtained from *XRD*. While the Dulong-Petit model is commonly used above the Debye temperatue Θ_D, it can underestimate the thermal conductivity by $\sim$ 10 - 20 % [9].

Optical measurements were performed by Zachary M. Gibbs to characterize the electronic band gap of *n*-type ZrNiSn. The measurements were performed at room temperature using a diffuse reflectance infrared Fourier transform spectroscopy method (DRIFTS). A Nicolet 6700 Fourier transform infrared spectrophotometer and a Praying Mantis attachment was used. The detector used was a deuterated triglycine sulfate (DTGS) detector with a KBr beamsplitter. The absorption coefficient was obtained from a Kubelka Munk analysis:

$$F(R) = \frac{\epsilon}{K} = \frac{(1-R)^2}{2R} \tag{6.5}$$

where R is the fractional reflectance, ϵ is the absorption coefficient and K is the scattering coefficient. Because we expect that the particle size exceeds the light wave length measured typically 2 - 20 μm, the scattering coefficient is assumed to be independent of light frequency [51].

6.3 Analysis of the Transport Properties

For the analysis of the transport properties for *n*-type *M*NiSn half-Heuslers, solutions to the Boltzmann transport equation within the relaxation time approximation were used, with the assumption of a single parabolic band ($E(\vec{k}) \propto \frac{\hbar \vec{k}^2}{2m^*}$). This model is commonly used for bulk thermoelectric materials and referred to as SPB model. It is most accurate when the electronic transport is dominated by a single type of carriers and when the Fermi level is situated within a relatively parabolic and isotropic region of the band structure.

In this work, a differnet band model approaches was used, for samples with similar band structures and band gaps to estimate an effective mass *m**, using Eq. 6.6 - 6.9. The effective mass *m** is related to the Seebeck coefficient α, the carrier concentration *n* and the chemical potential η and can be determined from these values. $F_{j(\eta)}$ is the Fermi intergral (equation 6.8) with ς being the reduced carrier energy. From Seebeck measurements and by using eq.n 6.6, the chemical potential η can be determined. With η and the knowledge of the carrier concentraion n the effective mass *m** can be obtained from 6.7. These relations can be used to predict the dependency of the Seebeck coefficent, *zT*, $\alpha^2\sigma$ and *n* for samples with varying doping concentration, by assuming a rigid band behavior.

$$\alpha = \frac{k}{e}\left(\frac{(2+\lambda)F_{1+\lambda}(\eta)}{(1+\lambda)F_{\lambda}(\eta)} - \eta\right) \tag{6.6}$$

$$n = 4\pi\left(\frac{2m^{*}k_{B}T}{h^{2}}\right)^{3/2} F_{1/2(\eta)} \tag{6.7}$$

$$F_{j(\eta)} = \int_{0}^{\infty} \frac{\varsigma^{j}\,d\varsigma}{1+e^{\varsigma-\eta}} \tag{6.8}$$

$$\mu_{H} = \mu_{0}\frac{\pi^{1/2}F_{\lambda(\eta)}}{F_{1/2(\eta)}} \tag{6.9}$$

From Eq. 6.9 it can be seen, that the mobility of the carriers is related to the chemical potential, where the intrinsic mobility μ_0 is a fitting parameter, which can be solved for when the chemical potential and the carrier mobility are known. So with Eq. 6.6- 6.9 and by assuming a constant value for the thermal conductivity, the figure of merit and power factor can be estimated as a function of chemical potential. This leads to the estimation of the optimum carrier concentration for a given material at a given temperature. More details about this method can be found in the handout by May *et al* [52].

7 Acceptor Doping of ZrNiSn Half-Heuslers

The transport properties of thermoelectric HH alloys is sensitive to structural interferences like isoelectronic alloying or through substitutional effects. Here the influence of hole substitution on the thermoelectric properties of ZrNiSn will be discussed. Through substitution with acceptor dopants like Al, Ga or In or transition metals like Y, Sc or La transition from *n*- to *p*-type behavior can be achieved, accompanied by a drastic change in the thermoelctric properties.

7.1 Main Group Element Acceptor Dopant

7.1.1 Al as Acceptor Dopant

The triel elememt Al ($3s^2$ $3p$) with one valence electron (VE) less than Sn ($4d^{10}$ $4s^2$ $5p^2$) acts as a *p*-dopant on the Sn site, in the otherwise charged balanced ZrNiSn HH compound (VEC $= 18$). By substituting with one of the main group elements Al, Ga or In a compensation for the influence of the electrons dominating the thermoelectric properties is expected.

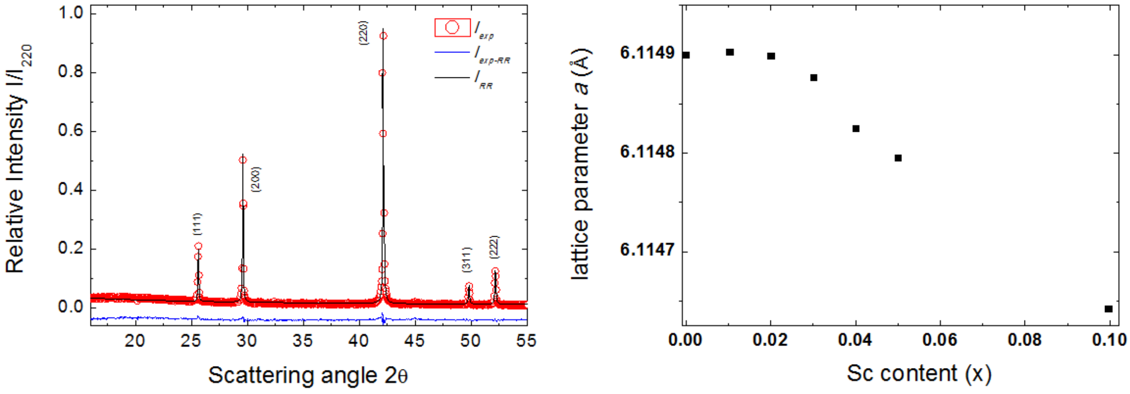

Figure 7.1: Shown are the powder *XRD* pattern for the ZrNiSn (I_{exp}) with Rietveld refinement *RR* (I_{RR}) and the difference profile (I_{exp-RR}) a) and the dependence of the lattice parameter a (Å) for Zr$_{1-x}$Al$_x$NiSn versus Al content (x) b). A rough decrease of the lattice constant with increasing Al content was observed, leading to the assumption, that Al was not completely substituted into the structure.

Fig. 7.1 shows a representative *XRD* pattern for ZrNiSn which conforms to the well-defined cubic structure typical for the HH phase containing negligible amounts of Sn metal. The calculation of the lattice parameter and the crystal structure refinements were done using the Rietveld method which yielded a lattice parameter of a = 6.1148 Å for the undoped sample. The reported value agrees with the one from the literature [53]. Fig. 7.1 shows a rough decrease of the lattice constant with increasing Al content. The radii for Sn and Al are respectively 1.40 and 1.43 Å, therefore an increase in the lattice parameter would have been expected. The total Al content is too less and therefore lies below the *XRD* detection limit to be visible. This leads to the assumption, that Al was not completely substituted into the structure, according to the corresponding radii of Al and Sn.

ZrNiSn$_{1-x}$Al$_x$ is a valence electron deficient compound. Undoped ZrNiSn was found to be highly electron doped with a carrier concentration n_H at room temperature (RT) of $2.3 * 10^{19}$ cm^{-3}. For the ZrNiSn$_{1-x}$Al$_x$ solid solution the room temperature carrier concentration n_H was measured and is shown in Fig. 7.2. The Hall coefficient R_H was negative for all the samples, assuming that electrons are the main charge carriers at *RT*. Upon low Al concentrations the carrier concentration increases slowly and above 4 at.% more drastically.

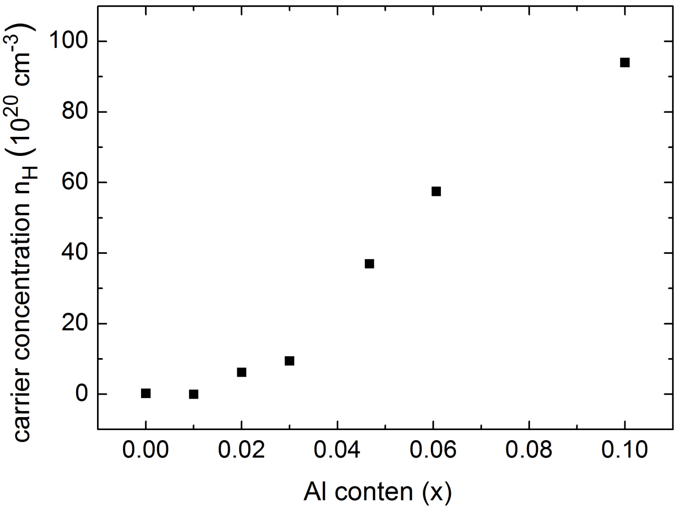

Figure 7.2: With increasing Al content, the absolute Hall carrier concentration n_H at 300 K in ZrNiSn$_{1-x}$Al$_x$ increases. Above 4 at.% Al, n_H increases more drastically ascribed to Al metal inclusions.

The increase from x = 0.03 to x = 0.05 is almost one order of magnitude. Correspondingly the resistivity decreases (Fig. 7.3). As seen from the powder *XRD* measurements (Fig. 7.1) Al does not substitute into the lattice, thus the fast increase of n_H is assumed to be correlated to Al metal inclusions contributing more electrons to the ZrNiSn solid solution.

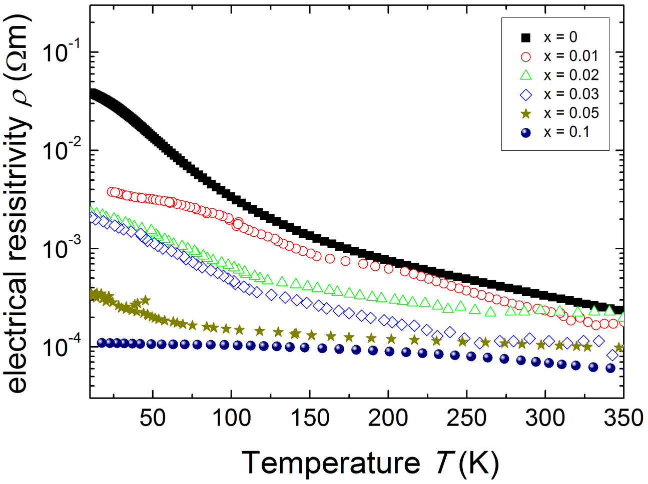

Figure 7.3: Temperature dependence of the electrical resistivity in the ZrNiSn$_{1-x}$Al$_x$ (x = 0 - 0.1) solid solution from 10 to 350 K.

The temperature dependence of the Seebeck coefficient α for the ZrNiSn$_{1-x}$Al$_x$ solid solutions exemplified in Fig. 7.4 a, revealed negative values over the whole temperature range, which indicates that electrons are the majority charge carriers in this system. The maximum Seebeck coefficient of -290 μV/K was measured for the parent compound ZrNiSn. The Al metal inclusions were responsible for the shift of the maximum Seebeck coefficient toward higher temperatures. While the electrical resistivity decreased with increasing Al content, the absolute Seebeck coefficient was reduced, according to the Mott formula [54]. Even though the electrical resistivity was decreased the power factor (Fig. 7.4 b) could not be improved, due to the diminution of the Seebeck coefficient with increasing Al content.

Fig. 7.5 a) shows the temperature dependence of the total thermal conductivity κ_{tot} ($\kappa_{tot} = \kappa_e + \kappa_e$) with increasing Al content. The slight decrease with increasing Al content is associated with additional phonon scattering centers due to the Al inclusions. This is supported by the fact, that the sample with the highest Al content shows the lowest thermal conductivity. The calculated dimensionless figure of merit, zT, according to Eq. 5.3 is shown in Fig. 7.5 b). Due to the degraded power factor caused by the Al doping, the zT values could not be improved as well. The reduction of the total thermal conductivity and the electrical resistivity was not enough to compensate for the diminution of the Seebeck coefficient. The maximum zT of 0.005 at 350 K was reached for the undoped ZrNiSn sample.

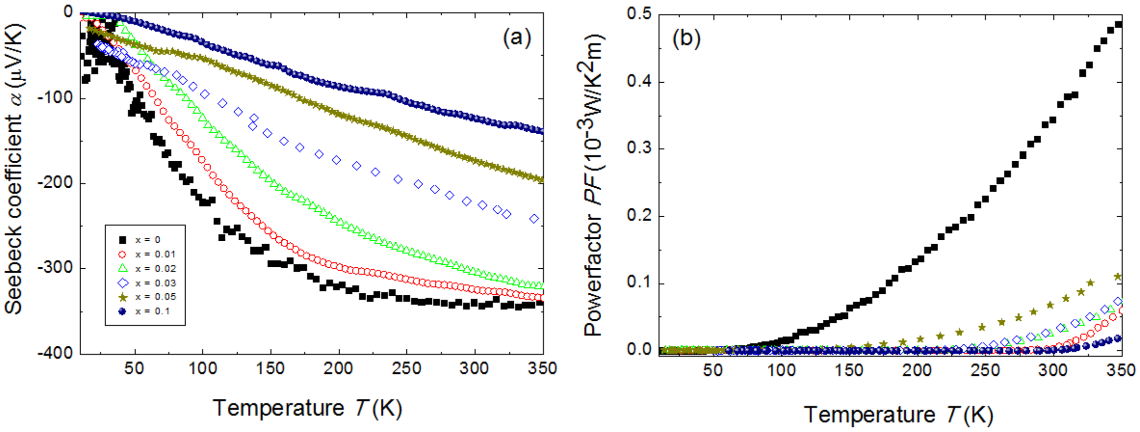

Figure 7.4: Temperature dependence of the Seebeck coefficient α a) and the power factor $\alpha^2\sigma$ b) in the ZrNiSn$_{1-x}$Al$_x$ (x = 0 - 0.1) solid solution from 10 to 350 K.

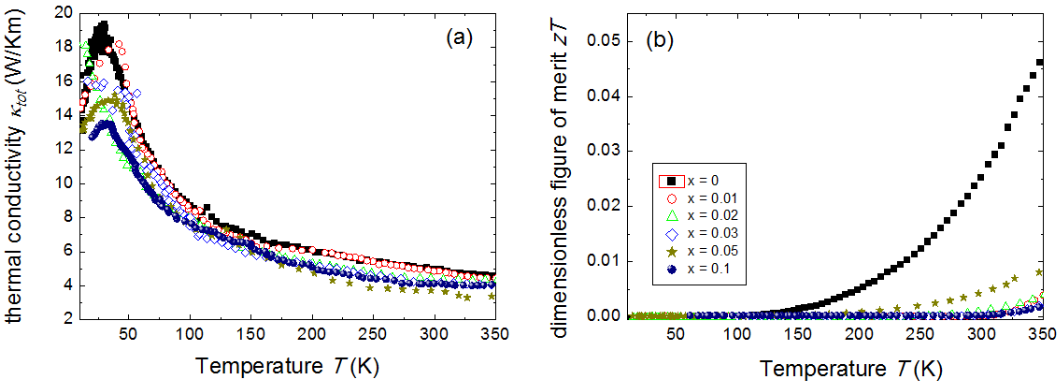

Figure 7.5: Temperature dependence of the total thermal conductivity κ_{tot} a) and the dimensionless figure of merit, zT, b) in the ZrNiSn$_{1-x}$Al$_x$ (x = 0 - 0.1) solid solution from 10 to 350 K.

The effect of Al substitution on the thermoelectric properties of the ZrNiSn$_{1-x}$Al$_x$ (x = 0 - 0.1) were systematically studied. *XRD* analysis lead to the assumption that Al was not completely substituted into the structure and might have segregated out as metal inclusions. Contrary to the expectations, the introduction of holes due to Al substitution on the Sn site could not be confirmed. The addition of Al lead to a diminished Seebeck coefficient, $\alpha^2\sigma$ and zT. This is the reason why Al is an inadequate *p*-type dopant for the ZrNiSn system.

7.1.2 Ga as Acceptor Dopant

The electronic and thermal properties of ZrNiSn$_{1-x}$Ga$_x$ (x = 0 - 0.1) were investigated in the temperature range from 10 to 350 K. The triel elememt Ga ($3d^{10}$ $4s^2$ $4p$) with one valence electron (VE) less than Sn ($4d^{10}$ $4s^2$ $5p^2$) is expected to act as a *p*-dopant on the Sn site.

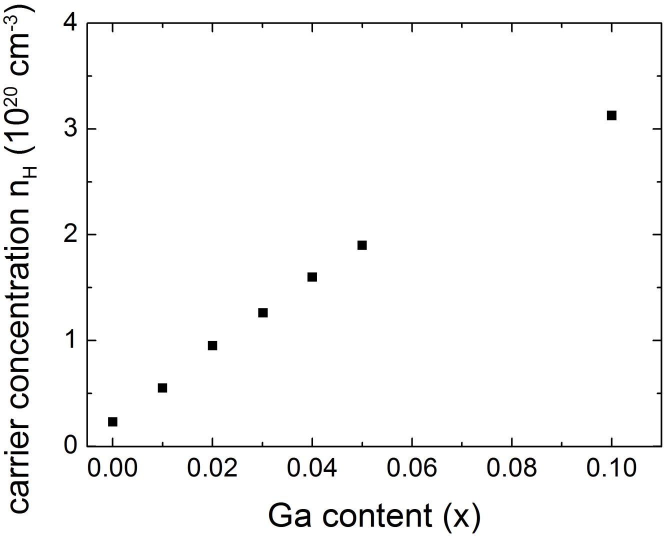

Figure 7.6: With increasing Ga content, the absolute Hall carrier concentration n_H at 300 K in ZrNiSn$_{1-x}$Ga$_x$ increased gradually. All samples exihibt a negative Hall coefficient R_H at room temperature.

The powder *XRD* pattern for the ZrNiSn$_{1-x}$Ga$_x$ (x = 0 - 0.1) solid solutions conform to the well-defined cubic structure typical for the half-Heusler phase containing negligible amounts of Sn metal. The calculation of the lattice parameter and the crystal structure refinements were done using the Rietveld method which yielded a lattice parameter of a = 6.1129 Å for the ZrNiSn$_{0.95}$Ga$_{0.05}$ sample. The radii for Sn and Ga are respectively 1.40 and 1.22 Å, therefore a decrease in the lattice parameter is expected. The samples geometric densities range from 95 - 97% of the theoretical density (7.9 g/cm^3).

ZrNiSn$_{1-x}$Ga$_x$ is a valence electron deficient compound. Pure ZrNiSn was found to be highly electron doped with a carrier concentration n_H at room temperature (*RT*) of 2.3*10^{19} cm^{-3}. For the ZrNiSn$_{1-x}$Ga$_x$ solid solution the room temperature carrier concentration n_H was measured and is shown in Fig. 7.6. The Hall coefficient R_H switched sign from negative to positive already for the sample containing x = 0.01 Ga at 150 K. All the samples show a positive Hall coefficient at

150 K with a later change in sign from positive to negative at around 200 K, indicating the *p*-type behavior at low temperatures. The room temperature carrier concentrations increases gradually with increasing Ga content, this influenced the electrical resistivity as well (Fig. 7.7). Above 200 K electrons become the dominant charge carriers.

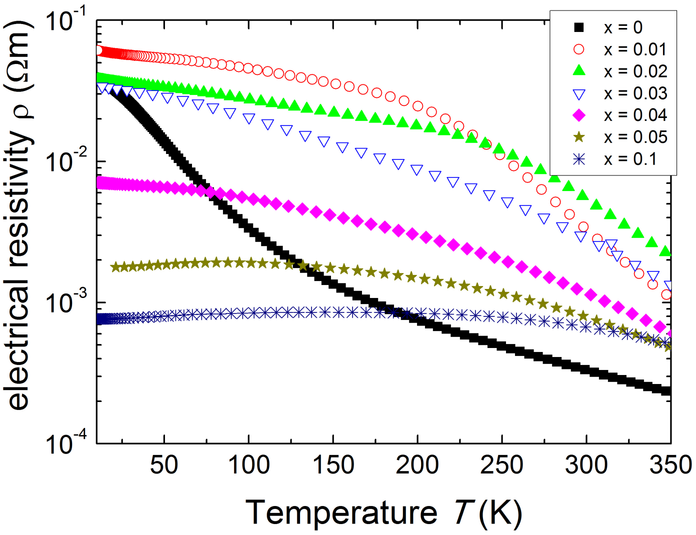

Figure 7.7: Temperature dependence of the electrical resistivity in the ZrNiSn$_{1-x}$Ga$_x$ (x = 0 - 0.1) solid solution from 10 to 350 K.

The temperature dependence of the Seebeck coefficient α for the ZrNiSn$_{1-x}$Ga$_x$ solid solutions are exemplified in Fig. 7.8. The Seebeck coefficient for the 1% Ga substituted sample switched sign at around 50 K from *n*- to *p*-type behavior. All other Ga substituted samples are *p*-types as well in this temperature regime. The sample with 3 at.% Ga content showed the highest Seebeck coefficient of this series of $+ 65\frac{\mu V}{K}$ at 150 K. With increasing hole carrier concentration the maximum of the Seebeck coefficient shifted to higher temperatures (according to the Mott Eq. [54]). At about 200 K all samples show a transition from *p*- to *n*-type behavior, where the thermal energy is high enough for the excitation of intrinsic carriers. Even though the electrical resistivity was decreased at room temperature for the substituted samples, the power factor (figure 7.9) could not be improved. This is ascribed to the fact, that the resistivity of the undoped sample is generally higher compared to the substituted samples and that the absolute Seebeck coefficient of the substituted samples is decreased at room temperature.

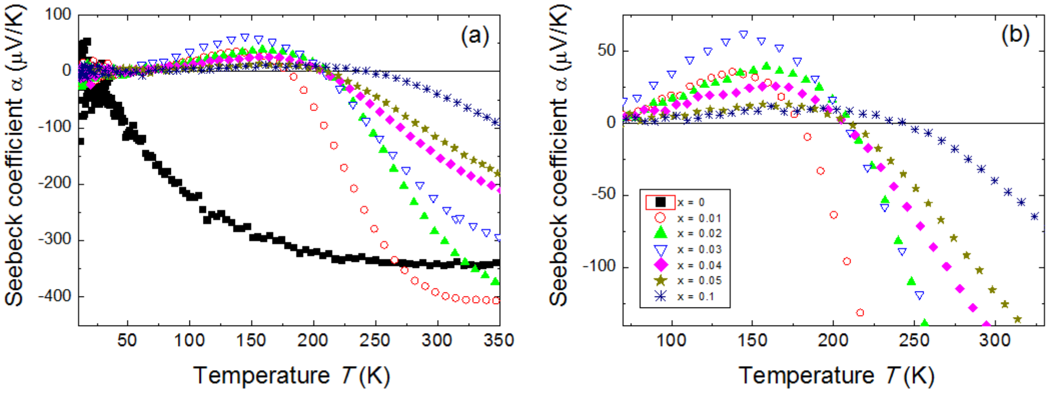

Figure 7.8: Temperature dependence of the Seebeck coefficient α a) within the temperature range 10-300 K and b) zoomed in Seebeck coefficients of the ZrNiSn$_{1-x}$Ga$_x$ (x = 0 - 0.1) solid solution.

Fig. 7.10 a) shows the temperature dependence of the total thermal conductivity κ_{tot} with increasing Ga content. The inrease with increasing Ga content is associated with increase in κ_e and the ρ. Therefore, the calculated dimensionless figure of merit, zT, according to Eq. 5.3 is shown in Fig. 7.10 b). Due to the increase in κ_{tot} and ρ with Ga substitution, the zT could not be improved. The maximum zT of 0.05 at 350 K was reached for the undoped ZrNiSn sample.

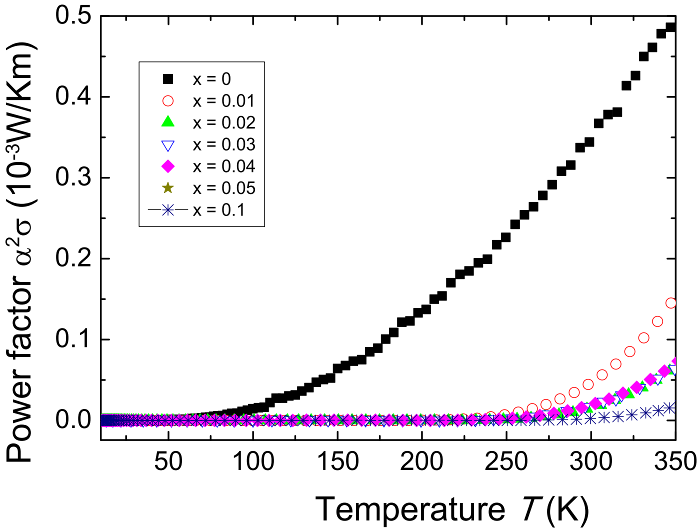

Figure 7.9: Temperature dependence of the power factor $\alpha^2\sigma$ in the ZrNiSn$_{1-x}$Ga$_x$ (x = 0 - 0.1) solid solution measured from 10 to 350 K.

The effect of Ga substitution on the thermoelectric properties of the ZrNiSn$_{1-x}$Ga$_x$ (x = 0 - 0.1) were systematically studied. *XRD* analysis lead to the assumption that Ga was completely substituted into the structure and therefore caused the change from *n*- to *p*-type behavior below 200 K. The highest Seebeck coefficient of + 65 μ V/K at 150 K was achieved for the sample containing 1 at.% Ga. All Ga samples show a roll-over in the Seebeck coefficient due to thermal excitation of intrinsic charge carriers at elevated temperatures. The addition of Ga increased the thermal conductivity drastically and therefore could not lead to a further improvement of the thermoelectric figure of merit, *zT*.

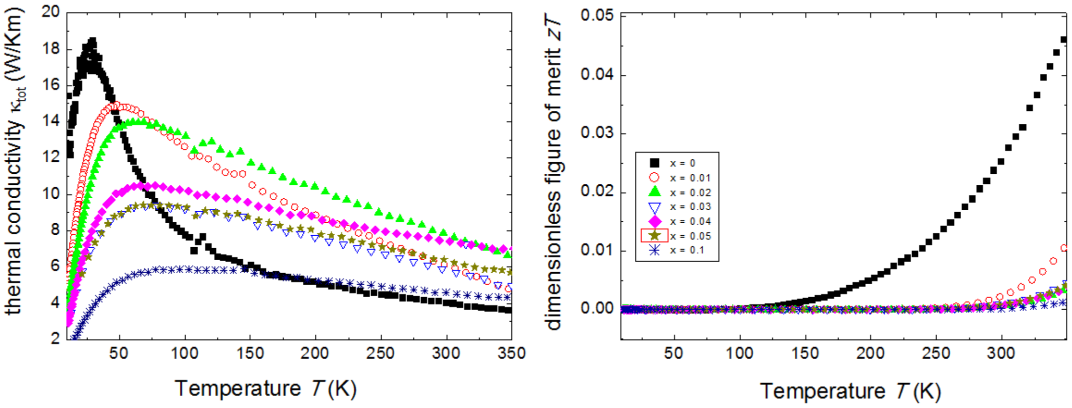

Figure 7.10: Temperature dependence of the total thermal conductivity κ_{tot} a) and the dimensionless figure of merit, *zT*, b) in the ZrNiSn$_{1-x}$Ga$_x$ (x = 0 - 0.1) solid solution from 10 to 350 K.

7.1.3 In as Acceptor Dopant

As Al the triel elememt In (4 d^{10} $5s^2$ $5p$) possesses one valence electron (VE) less than Sn ($4d^{10}$ $4s^2$ $5p^2$) and therefore acts as a *p*-dopant, when substituting for Sn.

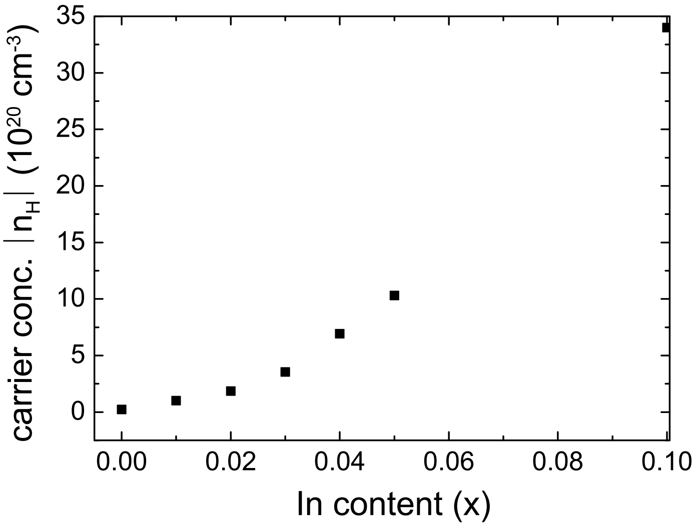

Figure 7.11: With increasing In content, the absolute Hall carrier concentration n_H at 300 K in ZrNiSn$_{1-x}$In$_x$ increases gradually. All samples exihibt a negative Hall coefficient R_H at room temperature.

The typical cubic structure of half-Heuslers of the ZrNiSn$_{1-x}$In$_x$ (x = 0 - 0.1) solid solution was confirmed by *XRD* measurements. The calculation of the lattice parameter and the crystal structure refinements were done using the Rietveld method which yielded a lattice parameter of a = 6.1132 Å for the ZrNiSn$_{0.95}$In$_{0.05}$ sample. The radii for Sn and In are respectively 1.40 and 1.63 Å, therefore an increase in the lattice parameter is expected, leading to the assumption that In was substituted into the lattice.

ZrNiSn$_{1-x}$In$_x$ is a valence electron deficient compound. Undoped ZrNiSn was found to be highly electron doped with a carrier concentration n$_H$ at room temperature (*RT*) of 2.3*10^{19} cm^{-3}. For the ZrNiSn$_{1-x}$In$_x$ solid solution the room temperature carrier concentration n_H was measured and is shown in Fig. 7.11. The Hall coefficient R_H switched sign from negative to positive for the sample containing x = 0.03 In at 100 K. All the samples with an In content of x > 0.03 show a positive Hall coefficient at 150 K with a later change in sign from positive to negative between 200 K and 300 K. Above 300 K electrons are dominating the transport properties. Whereas, below 200 K where holes are dominant a metal-semiconding transition in the electrical resisitvity data is observed (see Fig. 7.12). Generally the room temperature carrier concentrations increases slowly with increasing In content.

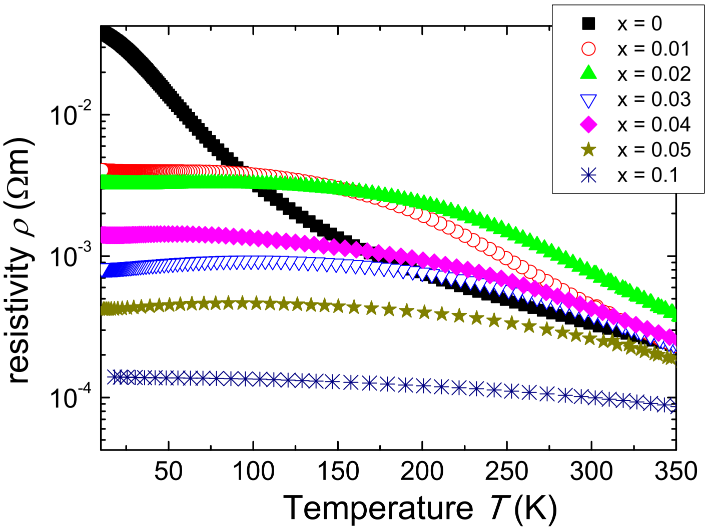

Figure 7.12: Temperature dependence of the electrical resistivity in the ZrNiSn$_{1-x}$In$_x$ (x = 0 - 0.1) solid solution from 10 to 350 K.

The temperature dependence of the Seebeck coefficient α for the ZrNiSn$_{1-x}$In$_x$ solid solutions are exemplified in Fig. 7.13 a) and b). The Seebeck coefficient for the 3 at.% In substituted sample switched sign at 100 K from *n*- to *p*-type behavior. As well as all In substituted samples thereafter. The sample with 4 at.% In content showed the highest Seebeck coefficient of + 20 μ V/K at 150 K. With increasing hole concentration the maximum of the Seebeck coefficient is shifted to higher temperatures (according to the Mott Eq. [54]). Between 200 K and 300 K all samples show the expected transition from *p*- to *n*-type, where the thermal energy is high enough for the excitation of intrinsic charge carriers. Even though the electrical resistivity was decreased at room temperature for the substituted samples, the power factor (Fig. 7.14) could not be improved. This is ascribed to the fact, that the resistivity of the undoped sample is generally lower compared to the substituted samples and that the absolute Seebeck coefficient of the substituted samples is generally decreased, due to bipolar effects.

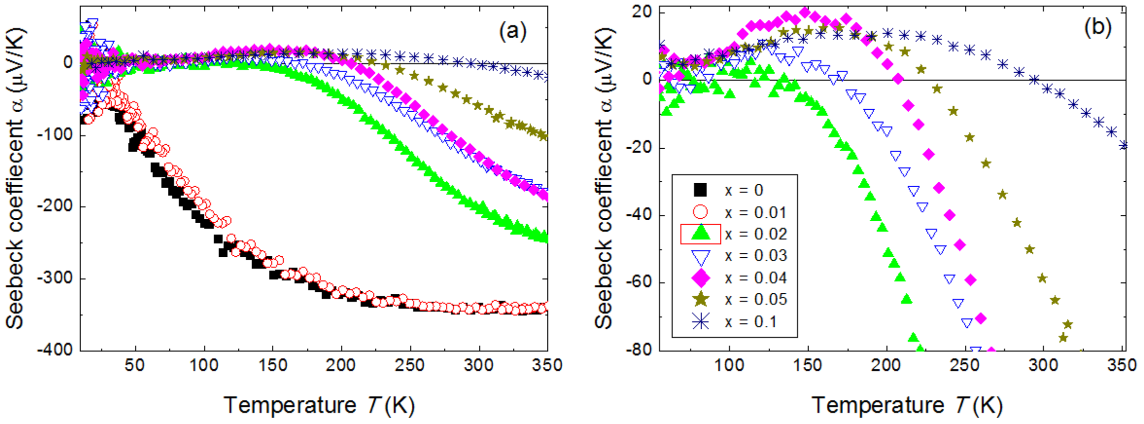

Figure 7.13: Temperature dependence of the Seebeck coefficient α of the ZrNiSn$_{1-x}$In$_x$ (x $=$ 0 - 0.1) solid solution measured from 10 to 350 K. And zoomed in to show the roll-overs of the samples at different temperatures.

Fig. 7.15 a) shows the temperature dependence of the total thermal conductivity κ_{tot} with increasing In content. The bump around 100 K is an artefact from the calibration of the thermometer. With increasing In content the total thermal conductivity is increasing as well. This is associated with an enhancement in κ_e and the ρ. Therefore, the calculated dimensionless figure of merit, *zT*, according to Eq. 5.3 is shown in Fig. 7.15 b). Due to the increase in κ_{tot} and ρ with In substitution, the *zT* could not be improved. The maximum *zT* of 0.05 at 350 K was reached for the undoped ZrNiSn sample.

The effect of In substitution on the thermoelectric properties of the ZrNiSn$_{1-x}$In$_x$ (x $=$ 0 - 0.1) were systematically studied. *XRD* analysis lead to the assumption that In was completely substituted into the structure and therefore caused the change from *n*- to *p*-type behavior below 200 K. The highest Seebeck coefficient of $+$ 20 μ V/K at 150 K was achieved for the sample containing 4 at.% In. Samples with an In content x $>$ 0.03 are *p*-type and show a roll-over in the Seebeck coefficient due to bipolar effects at elevated temperatures. The addition of In slightly increased the thermal conductivity, therefore a further improvement of the thermoelectric figure of merit, *zT*, could not be achieved.

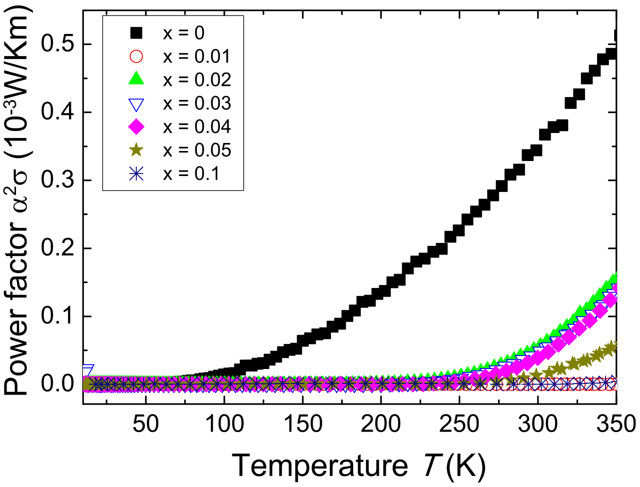

Figure 7.14: Temperature dependence of the power factor $\alpha^2\sigma$ of the ZrNiSn$_{1-x}$In$_x$ (x = 0 - 0.1) solid solution measured from 10 to 350 K.

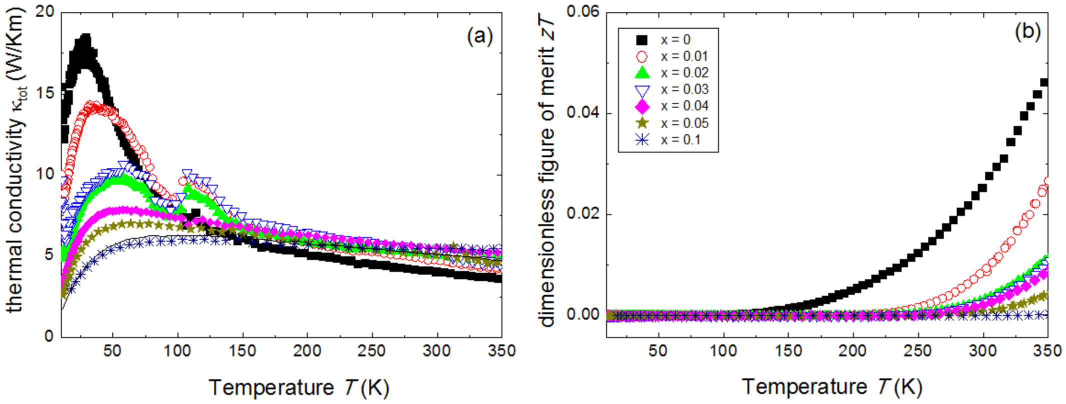

Figure 7.15: Temperature dependence of the total thermal conductivity κ_{tot} a) and the dimensionelss figure of merit, zT, b) in the ZrNiSn$_{1-x}$In$_x$ (x = 0 - 0.1) solid solution from 10 to 350 K.

7.2 Transition Metal Dopants

7.2.1 Y as Acceptor Dopant

Y has already been explored as an acceptor dopant in the temperature range from 10 to 350 K [18, 55, 56, 57]. It could be shown that the subtitution of Zr by Y led to a change from *n*- to *p*-type behavior. For Y concentration of x $>$ 0.05 the Seebeck coefficient is positive over the whole temperature range (10 - 350 K) [57], indicating a maximum around 350 K. Thus, the Seebeck coefficient will decline at higher temperatures, due to an early onset of bipolar conduction leading to a diminution of the Seebeck coefficient. This was proved by Krez *et al.*, who also showed that the introduction of Y lead to a reduction of the electrical conductivity leading to diminished values for the power facotr and the figure of merit [56]. Thus, Y substitution was not further explored as a suitable *p*-dopant.

7.2.2 Sc as Acceptor Dopant

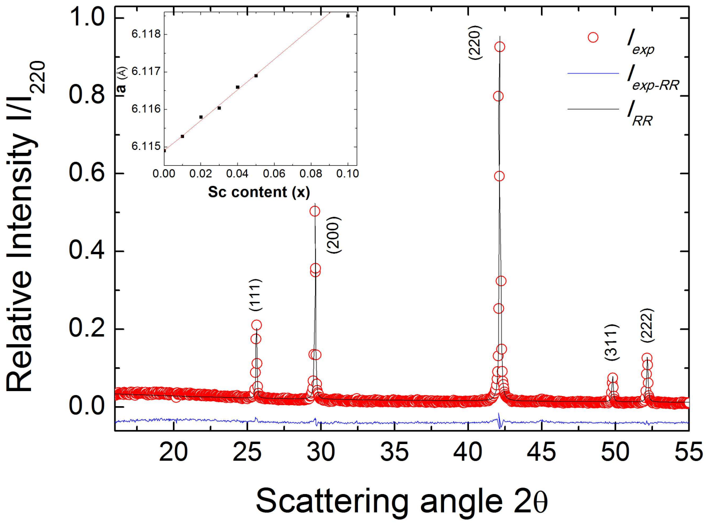

Figure 7.16: Powder XRD pattern for the Zr$_{0.95}$Sc$_{0.05}$NiSn sample (I_{exp}) with Rietveld refinement RR (I_{RR}) and the difference profile (I_{exp-RR}). The inset shows the dependence of the lattice parameter a (Å) for Zr$_{1-x}$Sc$_x$NiSn versus Sc content (x). The straight line is the result of a linear fit to Vegard's law [58].

Horyn' *et al* [45] started to investigate the effects of substituting Sc for Ti or Zr up to 350 K, which showed a promising positive Seebeck coefficient at room temperature. The current study will extend the already existing studies on Sc substitution and show that Sc can be an excellent *p*-type dopant with excellent transport properties. Thus, the findings of this study are significant due to the current lack of compatible *p*-tpe materials. At first we will discuss the low temperature thermoelectric properties of the $Zr_{1-x}Sc_xNiSn$ (x = 0 - 0.1) solid solution and then move on to the high temperature properties. Through Sc substitution, we successfully dope ZrNiSn to be *p*-type, and we measure the thermoelectric properties up to 850 K.

Fig. 7.16 shows a representative *XRD* pattern for $Zr_{0.95}Sc_{0.05}NiSn$ which conforms to the well-defined cubic structure typical for the half-Heusler phase containing negligible amounts of Sn metal. The calculation of the lattice parameter and the crystal structure refinements were done using the Rietveld method which yielded a lattice parameter of a $= 6.1148\ \mathring{A}$ for the undoped sample (this agrees with the values reported in the literature [53]). The inset in Fig. 7.16 shows a roughly monotonic increase with increasing Sc amount, which agrees well with Vegard's law [58]. The increase serves as evidence that the slightly larger Sc atoms (radius = 1.60 Å) substitute for Zr (radius = 1.55 Å).

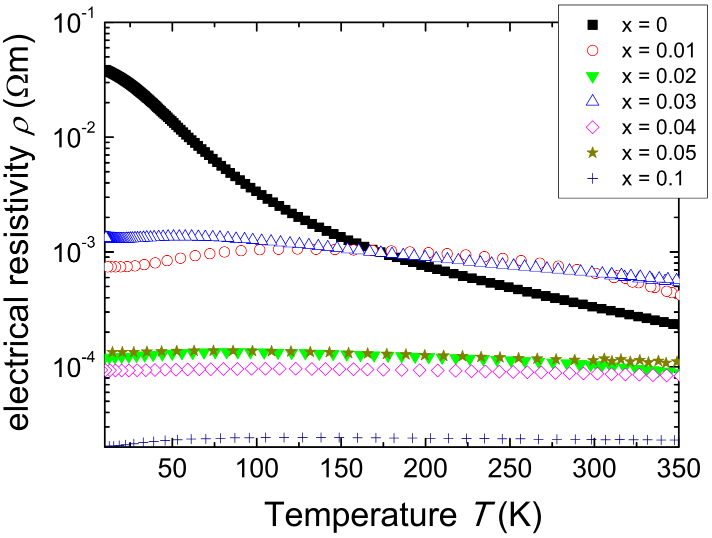

Figure 7.17: Temperature dependence of the electrical resistivity in the $Zr_{1-x}Sc_xNiSn$ (x = 0 - 0.1) solid solution from 10 to 350 K. With increasing Sc content the electrical resistivity gradually decreases.

The temperature dependence of the Seebeck coefficient α for the $Zr_{1-x}Sc_xNiSn$solid solutions are exemplified in Fig. 7.18 a) and b). The Seebeck coefficient already switched sign from *n*- to *p*-type behavior for 1 at.% Sc doping. Although the hole concentration is not high enough to compensate for the concentration of electrons in the system (see fig. 7.24). At substitution level of 3 at.% Sc the Seebeck coefficient is positive over the whole temperature range, indicating that holes are the dominant charge carriers in this system. The Seebeck coefficient changes sign at 350 K from - 350 μV/K to + 120 μV/K for 4 at.% Sc substitution. Whereas low Sc levels clearly show a maximum in the Seebeck coefficient. This maximum get shifted to high temperatures, with increasing Sc content.

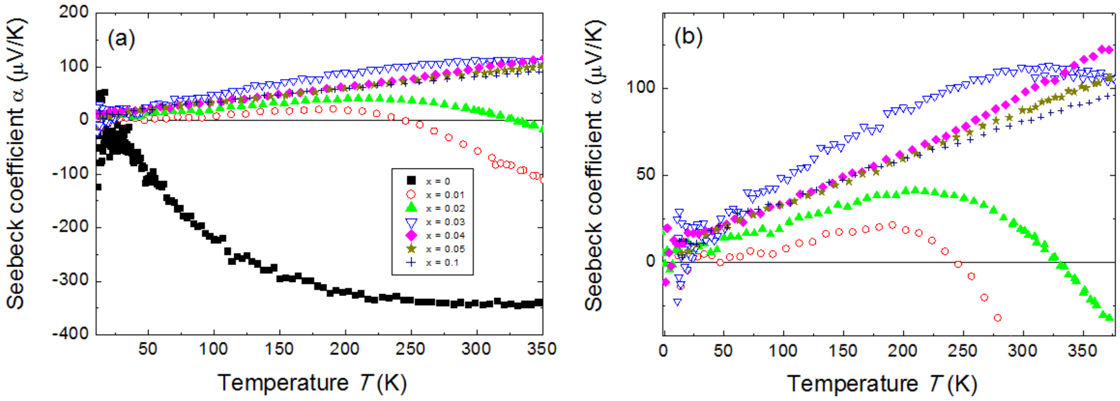

Figure 7.18: Temperature dependence of the Seebeck coefficient α of the $Zr_{1-x}Sc_xNiSn$ (x = 0 - 0.1) solid solution measured from 10 to 350 K. And zoomed in to show the roll-overs of the samples at different temperatures.

The electrical resistivity was decreased for the substituted samples. The power factor (Fig. 7.19) could not be improved. The thermal conductivity and figure of merit, *zT*, are shown in Fig. 7.20. The sample with x = 0.1 Sc exhibits a high $\alpha^2\sigma$ and *zT*, due to the increased electrical conductivity and the reduced thermal conductivity.

The total thermal conductivity κ_{tot} of ZrNiSn exhibits a maximum at 30 K. At low temperatures the phonons mean free path *l* is temperature independent and comparable to the crystal dimensions and only influenced by boundaries and imperfections. Due to the temperature independence of the mean free path l the thermal conductivity is solely determined by the heat capacity and therefore follows a T^3 law. As the temperature increases Umklapp-processes appear (U-process) and will gradually reduce the mean free path, eventually being smaller than the crystal dimensions, where κ will reach a maximum. At high enough temperatures the heat capacity C_v is a constant and the thermal conductivity decays with a 1/T temperature dependence (in this case >150 K). These temperature trends can best be observed in the undopoed ZrNiSn sample. Substitution with Sc results in a reduction of κ and a suppression of the maximum at 30 K. This is associate with

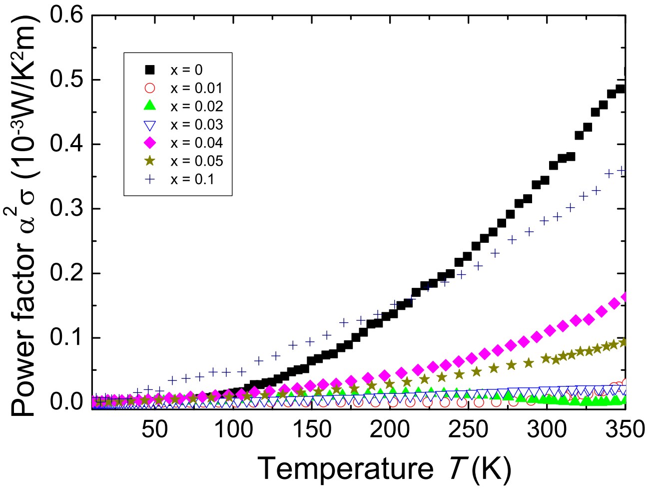

Figure 7.19: Temperature dependence of the power factor $\alpha^2\sigma$ of the Zr$_{1-x}$Sc$_x$NiSn (x = 0 - 0.1) solid solution measured from 10 to 350 K.

additional scattering at impurities caused by the higher Sc content, at higher temperatures κ still follows a 1/T temperature dependence.

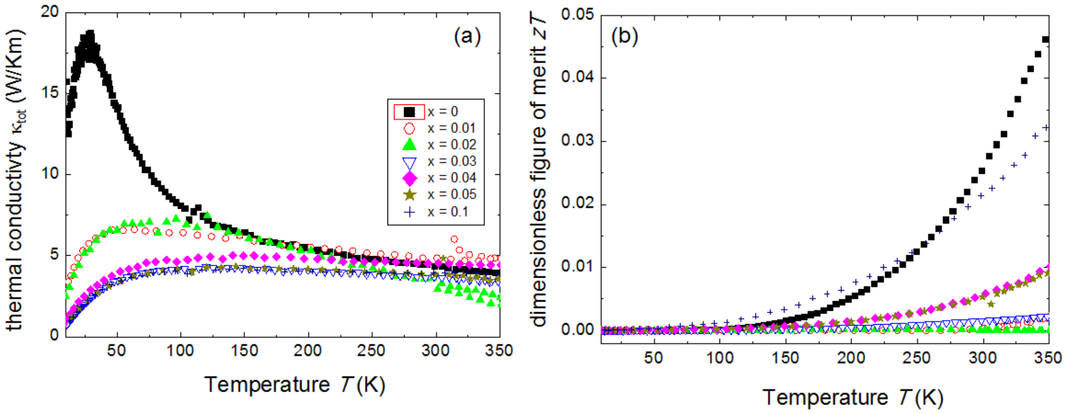

Figure 7.20: Temperature dependence of the total thermal conductivity κ_{tot} a) and the dimensionelss figure of merit, zT, b) in the Zr$_{1-x}$Sc$_x$NiSn (x = 0 - 0.1) solid solution from 10 to 350 K.

It is noticeable, that even substitution of small amounts of Sc for Zr leads to a sign inversion of the Seebeck coefficient, due to a reduction of electrons in the system. Sc substitution is the most promising *p*-type HH solid solution, with the highest measured Seebeck coefficients in *M*NiSn-based system. Therefore, this is the only series, which was chosen for further high temperature transport measurements. But before we take a closer look at the high temperature results, a short introduction of the influence of Sc on the electronic structure of ZrNiSn will be given.

$Zr_{1-x}Sc_x$NiSn (x = 0 - 0.1) Solid Solution and the Theoretical Point of View

Fig. 5.11 shows the calculated band structure and the density-of-states of ZrNiSn. As mentioned the thermoelectric *M*NiSn half-Heusler compounds, are semiconductor with a calculated indirect band gap of 500 meV. The valence band (VB) maximum appears at Γ and the conductions band maximum at *X*.

Most important for comprehending the transport properties is, to understand the behavior of the chemical potential μ with temperature and doping. Fig. 7.21 displays the temperature depend $\mu(T)$ for pue ZrNiSn and with *p*-type doping. ϵ_F is the Fermi level and defined as being the highest occupied energy state at T = 0 K. Its exact position depends on the occupancy of the DOS, which can be calculated through the expression for the Fermi-Dirac distribution. The influence of elemental substitution is shown in Fig. 7.22. As an example the substitution of Sc for Zr was taken. With increasing Sc content the Fermi level shifts below the valence band edge. For high substitution levels the $Zr_{1-x}Sc_x$NiSn (x = 0 - 0.10) solid solution becomes almost metallic.

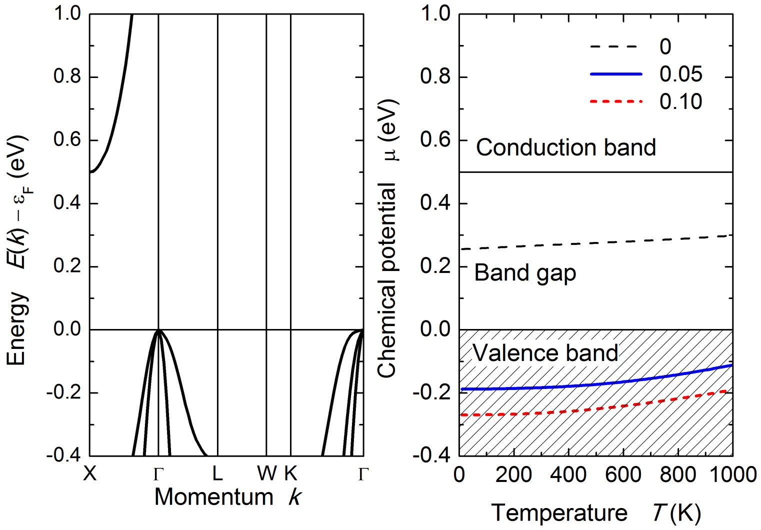

Figure 7.21: On the left side the band structure *E(k)* is shown on an enlarged scale, whereas the right side displays the chemical potential in pure and hole doped ZrNiSn for two doping levels. The *ab-initio* calculations were provided by Dr. G. Fecher from the Max-Planck Institute for Chemical Physics of Solids.

The transport properties were calculated from the Boltzmann transport theory within a relaxation time approximation. The calculations are based on the electronic structure calculations of perfect ZrNiSn compound and were done by Dr. G. Fecher from the Max-Planck Institute for Chemical Physics of Solids. According to this theory the Seebeck coefficient $\alpha(\mathsf{T}\tau)$ is a relaxation time independent quantity, whereas the electrical conductivity $\sigma(\mathsf{T})/\tau$ still contains a relaxation time dependence. The power factor is calculated using the following relation: $PF/\tau = \alpha(T)^2\sigma(T)\tau$. The calculated transport properties are shown in Fig. 7.22. For n = 0 ZrNiSn is a pure semiconductor. With increasing charge carriers the conductivity strongly increases, more so if electrons are the main charge carriers. Typical for semiconductors are their high Seebeck coefficients at low carrier concentrations. The Seebeck coefficient will decrease with the increasing amount of carriers (see Eq. 6.6). As the power factor is derived from $\alpha(T)^2\sigma(T)/\tau$ and related through σ with the carrier concentration (see Eq. 6.2) it will decrease with increasing carrier concentration as well. The position of its maximum depends on the kind of carriers and the temperature. Fig. 7.22 suggests, that *p*-type HH compounds exhibit higher a power factor than *n*-type. This is in disagreement with the experimental findings. The reasons are the different relaxation times for electrons and holes within the bands.

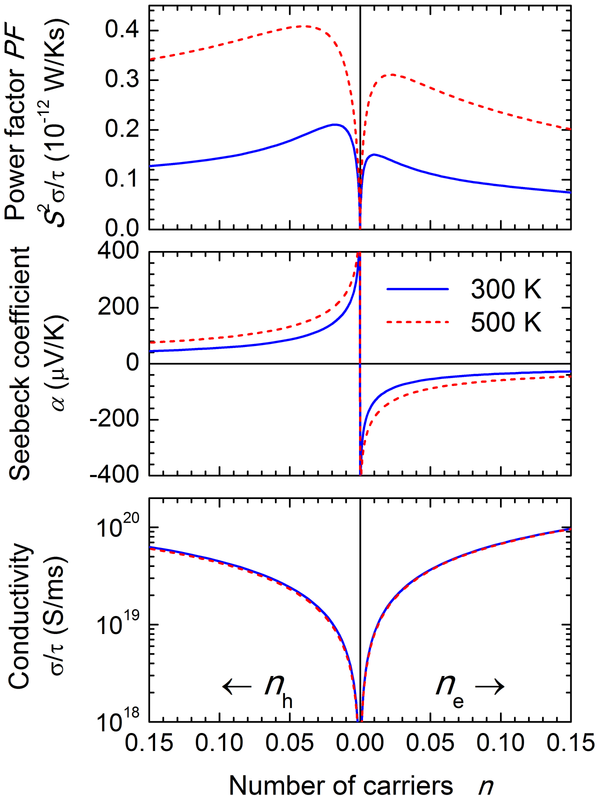

Figure 7.22: Electronic structure of Sc substituted ZrNiSn. Compared are in a) the pure and in b) the 10 at.% Sc subsituted samples. The *ab-initio* calculations were provided by Dr. G. Fecher from the Max-Planck Institute for Chemical Physics of Solids.

As seen from Fig. 7.21 ZrNiSn becomes *p*-type when Zr is partly substituted by Sc. The changes to the electronic band structure for the Zr$_{0.9}$Sc$_0$.1NiSn solid solution is displayed in Fig. 7.23 for a Sc amount of x = 0.1. It appears that Sc substitution causes a rigid band shift of the Fermi energy into the valence band. Compared to the band structure shown in Fig. 7.23 a) it can be seen, that several states undergo a distinct broadening. This is caused by the Sc *impurities*, which are destroying the lattice perfection making coherent electron waves impossible. The carriers are getting scattered at these atoms. The life time within the bands is inversely proportional to the energetically width of the states $(\tau(\Delta E)^-1)$. In a well ordered compound this width is zero and $\tau = \infty$. The conduction band is less influenced than the valence band. This is also affecting the high temperature transport in these compounds.

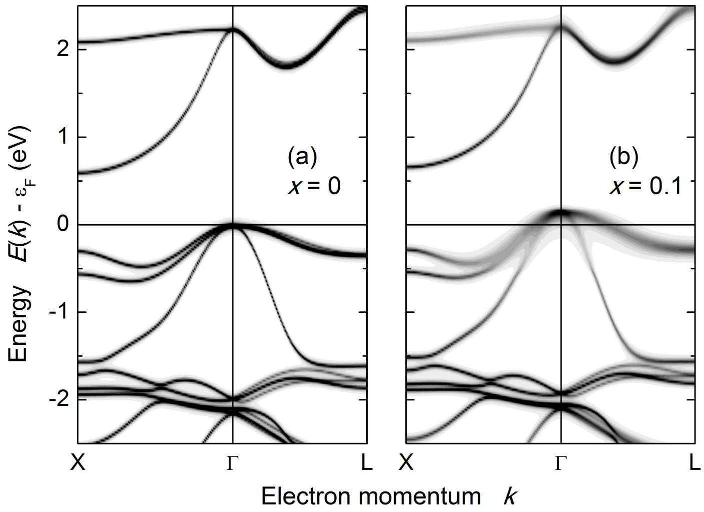

Figure 7.23: Illustrated are the transport properties of electron and hole doped ZrNiSn. From top to bottom panel are shown the relaxation time dependent power factor $\alpha^2\sigma$, Seebeck coefficient α and the relaxation time dependent conductivity σ/τ as a function of the number of holes n_h and electron n_e for two different temperatures. The *ab-initio* calculations were provided by Dr. G. Fecher from the Max-Planck Institute for Chemical Physics of Solids.

7.2.3 High Temperature Transport Properties of the Zr$_{1-x}$Sc$_x$NiSn (x = 0 - 0.1)

This section will extent the low temperature thermoelectric transport studies of *p*-type Zr$_{1-x}$Sc$_x$NiSn (x = 0 - 0.10) solid solution into the high temperature regime. Through Sc substitution, ZrNiSn was successfully converted into a *p*-type HH compound at room temperature.The high temperature transport properties were measured up to 850 K.

The investigation of the electrical properties of the Zr$_{1-x}$Sc$_x$NiSn (x = 0 - 0.1) solid solution are shown in Fig. 7.24 a). At room temperature, the samples exhibit high electrical resistivity, which decreases with increasing temperature for all the samples, indicating semiconducting behavior. For high substitution levels, both the room temperature value and the temperature dependence of the resistivity decreases pointing to a shift of the Fermi level towards the valance band (according to Fig. 7.21) as a result of an increasing *p*-type carrier concentration [58].

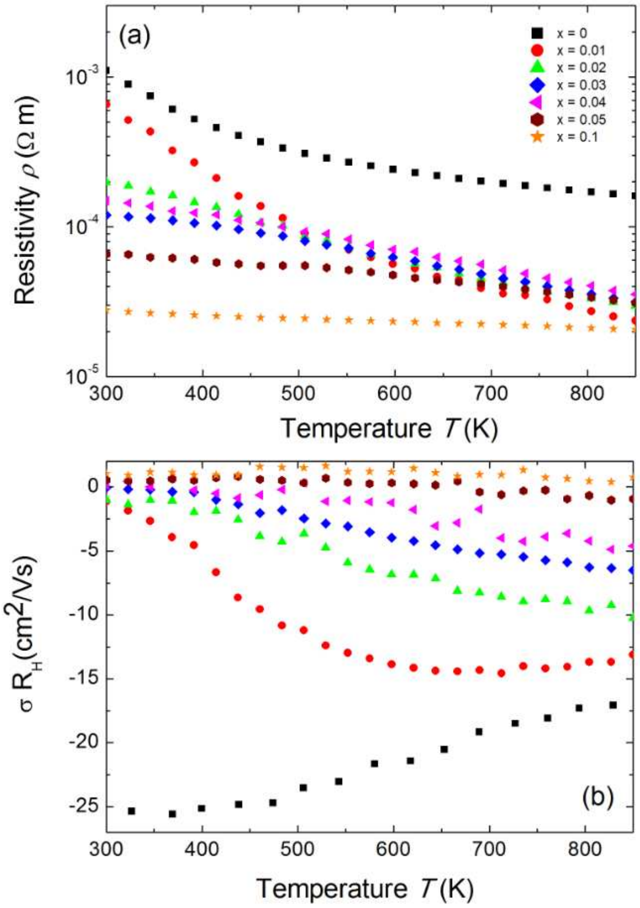

Figure 7.24: Temperature dependence of a) the electrical resistivity ρ and b) the σR_H product (in units of mobility) for the Zr$_{1-x}$Sc$_x$NiSn (x = 0 - 0.1) solid solution. The true Hall mobility at 300 K is largest for the *n*-type ZrNiSn sample b). With increasing the Sc content the magnitude of σR_H is reduced as a result of the influence of the holes [58].

For increasing Sc content in the Zr$_{1-x}$Sc$_x$NiSn solid solution it can be seen from Fig. 7.24 b) that the influence of σR_H (in units of mobility) of the electrons is suppressed (and eventually becomes positive) by the addition of holes. The parent compound *n*-type ZrNiSn exhibits the highest mobility, with a value at room temperature of 25 cm^2/V·s, which is a typical value for *X*NiSn based systems [37, 59]. This value is still significantly lower than the values for Bi$_2$Te$_3$ with 150 cm^2/V·s or 900-1400 cm^2/V·s for PbTe [60, 61]. If we assume that each replacement of Zr by Sc leads to one hole as a carrier, the room temperature electron concentration should be completely compensated when the Scandium concentration exceeds 5 at.%. At low Scandium content the samples with 0 $\leq$ x $\leq$ 0.04 possess a negative value for the σR_H, caused by the higher mobile electrons, which is consistent with a substitutional doping explanation [58].

The carrier mobility depends on the band effective mass m^* and the relaxation time τ roughly as $\mu = e\tau/m^*$ [1]. An estimate of *m** can be obtained from the *ab-initio* calculations of the electronic band structure [38] or from experimental Seebeck and Hall measurements (usually by applying the parabolic band approximation [13]). Since the effective mass varies inversely with the curvature of the bands, a high effective mass is a result of shallow or flat bands, whereas a small effective mass is typical for highly dispersed bands. Based on *ab-initio* calculations, a high mobility value for *n*-type ZrNiSn is expected due to their light conduction band (CB). The valence band (VB), however, has been shown to have a higher effective mass, so by substituting Zr by Sc one might expect generally lower mobilities for *p*-type materials as the Fermi energy gets shifted into the valance band (VB) at Γ [28, 62]. This is consistent with our experimental results shown in Fig. 7.24 b), the mobilities of heavily Sc doped samples are much lower in magnitude than the *n*-type ZrNiSn undoped sample [58]. In general, the transport properties of materials with small band gaps are influenced by both types of carriers [63] with a higher weight toward the ones with higher mobility:

$$R_H = \frac{n_p \mu_p^2 - n_n \mu_n^2}{e(n_p \mu_p - n_n \mu_n)^2} \text{ [63]}, \tag{7.1}$$

Here, n_n and n_p are the electron and hole concentration, respectively, and μ_n and μ_p are the electron and hole mobilities. If $\mu_n \geq \mu_p$, the sign for the Hall coefficient R_H can be negative even if $n_p \geq n_n$. In order to obtain a positive value for the Hall coefficient $n_p \mu_p$ needs to exceed $n_n \mu_n$ [63]. Because n_n and μ_n are unknown and difficult to determine, equ. 6.2 can be used assuming a single carrier type, but it will result in a value for that is greater than either the true n_p or n_n [58].

The Seebeck measurements for the Zr$_{1-x}$Sc$_x$NiSn solid solution are presented in Fig. 7.25. The pure ZrNiSn compound, without any Sc doping, displays a large negative Seebeck coefficient at room temperature, indicating a significant *n*-type defect concentration in ZrNiSn. With increasing Sc content, the value of α decreases, as compensating *p*-type defects (Sc on Zr site) are added to the naturally *n*-type material. It can be seen from the change in sign of the Seebeck coefficient from negative to positive that holes become the predominant charge carriers. This sign change of α occurs at lower Sc contents than observed for the sign change of the σR_H (Fig. 7.24 b)), indicating that in this region of mixed conduction, the holes probably outnumber electrons. However, because the electrons are more mobile, the Hall coefficient does not change sign until x > 0.05 (note that the mobilities are squared, shown in equation 7.1, whereas the Seebeck coefficient is weighted by mobility to the first power [64]. As observed in the Hall coefficient measurements, bipolar conduction of both electrons and holes is most likely responsible for the decrease in the thermopower at high temperatures [58].

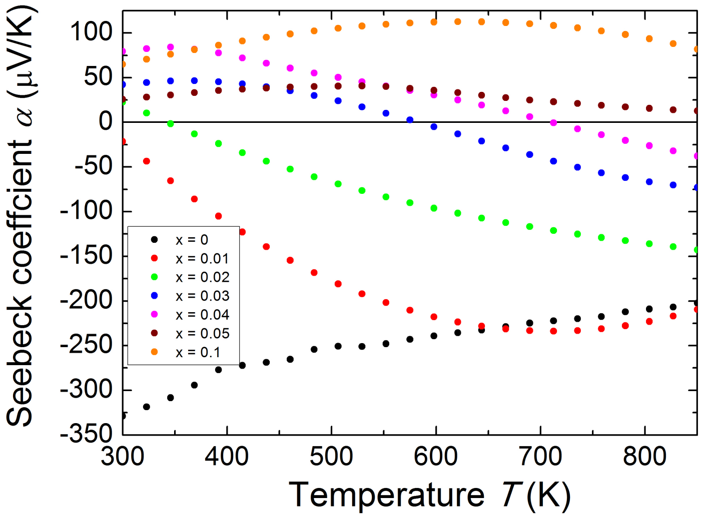

Figure 7.25: Shown is the temperature dependence of the Seebeck coefficent α for the Zr$_{1-x}$Sc$_x$NiSn (x = 0 - 0.1) solid solution. The Seebeck coefficient shows a roll-over, due to bipolar conduction [58].

In addition to indicating the onset of bipolar conduction, the maximum of the Seebeck coefficient can be used for the estimation of the band gap, E_g, according to Eq. 7.3, where values on the order of 0.05 eV were obtained. This is much smaller than the band gap suggested by Aliev *et al.* from electrical resistivity measurements (0.18 eV)[40]. The discrepancy between the estimation from our thermopower data and the literature estimates for the size of E_g in these compounds will be discussed in detail later.

$$E_g = 2S_{max}T_{max} \text{ [65]}, \tag{7.2}$$

where T$_{max}$ is the temperature at which the maximum of the absolute Seebeck coefficient occurs [65].

The total thermal conductivity was calculated from the thermal diffusivity (*D*) with $\kappa = C_pDd$, where C_p is assumed to be the Dulong-Petit heat capacity and *d* the density calculated from the molar mass and the lattice parameter for each sample obtained from *XRD*. As shown in Fig. 7.26, the room temperature thermal conductivity is reduced by 40% for Zr$_{0.9}$Sc$_{0.1}$NiSn compared with the undoped ZrNiSn. Because this is accompanied by a decrease in resistivity (Fig. 7.24 a), it is clear that this must be due to alloy scattering of phonons which reduces the lattice thermal conductivity (which is much greater than the electronic thermal conductivity at room temperature for all Sc compositions). The thermal conductivity of the undoped ZrNiSn is decaying with a 1/T relation but to 750 K, where bipolare effects set in. This behavior is characteristic of κ limited by phonon-phonon Umklapp process. For the doped samples other scattering mechanisms are adding to the Umklapp process as well as a stronger bipolar contribution. Above room temperature, we can see an increasing thermal conductivity for the doped samples consistent with the existence of both electrons and holes (as evidenced by Fig. 7.24 a) and Fig. 7.25). This effect occurs at lower and lower temperatures as the Sc content is increased. While this is less pronounced for the thermopower measurements, thermal conductivity is more sensitive, as it is getting effected by the overall decrease of the resistivity as well as by the bipolar term of the thermal conductivity. Although this is less pronounced for the Seebeck coefficient measurements, thermal conductivity is more sensitive, as it is affected by both the overall decrease of the resistivity and by the bipolar term of the thermal conductivity [58].

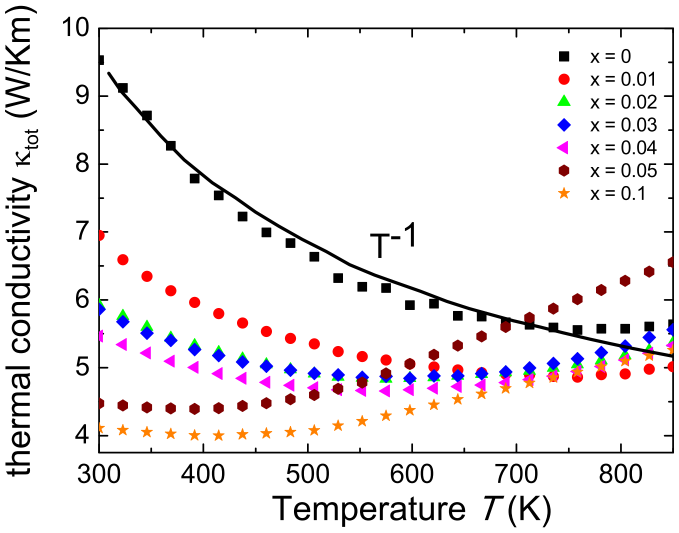

Figure 7.26: Total thermal conductivity of the $Zr_{1-x}Sc_xNiSn$ (x = 0 - 0.1) solid solution as a function of temperature [58].

Optical Properties and Band Gap Estimation

N-type *M*NiSn (*M* = Ti,Zr,Hf) half-Heusler compounds are successfully transitioning to prototype development in power generation systems because of their excellent thermoelectric properties which is believed to be attributed to their relatively high mobility. However *p*-type *M*NiSn systems have poor figure of merit, *zT* due to their diminished Seebeck coefficients and electrical conductivities, particularly compared to *M*CoSb compounds, as seen in the previous sections. This can be traced to the suppression of the magnitude of the Seebeck coefficient at high temperatures due to the excitation of minority carriers across the electronic band gap. To first order the band gap determines the temperature where the Seebeck coefficient reaches its maximum as described by the Sharp-Goldsmid formula [65], $E_g = 2S_{max}T_{max}$ (Seebeck band gap). However, from this formula one would conclude that the band gap for *p*-type *M*NiSn solid-solutions is only one third that of *n*-type *M*NiSn, which effectively prevents *p*-type *M*NiSn half-Heuslers from being useful thermoelectric materials. Studying the *p*-type HH $\text{Zr}_{1-x}\text{Sc}_x$NiSn solid-solutions revealed that the large mobility difference between electrons and holes in *M*NiSn results in a large corrections to the Sharp-Goldsmid formula. This finding explains the difference for the Seebeck band gap between *n*-type and *p*-type HH compounds with a true band gap of 0.13 eV based on optical absorption as well as transport data. The high electron to hole mobility ratio leads to an effective suppression of the bipolar effect in thermoelectric transport properties that is essential for the high *zT* values in *n*-type *M*NiSn (*M* = Ti,Zr,Hf) HH compounds. The influence of the high mobile electrons on the determination of the band gap and Seebeck coefficient will be described in further detail in this section [58].

Optical properties were measured to get information about the band structure, as displayed in Fig. 7.27. Undoped ZrNiSn was measured in diffuse reflectance at room temperature; the indirect optical band gap was extracted and the Tauc method was applied [66, 67].

$$ch\omega \propto (h\omega - E_g), \tag{7.3}$$

where *c* is the absorption coefficient, $h\omega$ is the photon energy, and E_g is the band gap. The estimated value of the indirect optical band gap is 0.13 eV. Aliev *et al.* measured similar samples previously, and and they reported a minimum in the absorption coefficient of approximately 2000 cm^{-1} (0.25 eV), a value that is slightly larger than those measured in this work, whereas electrical resistivity measurements gave gaps closer to 0.18 eV [34]. However, differences in results from those of Aliev *et al* and the ones measured in this work could be due to the difference in the measurement technique used. Here DRIFTS was used, whereas Aliev *et al.* used transmission/reflection measurements. Nonetheless, it is believed that the optical band gap (Fig. 7.27) reflects the true gap of the system.

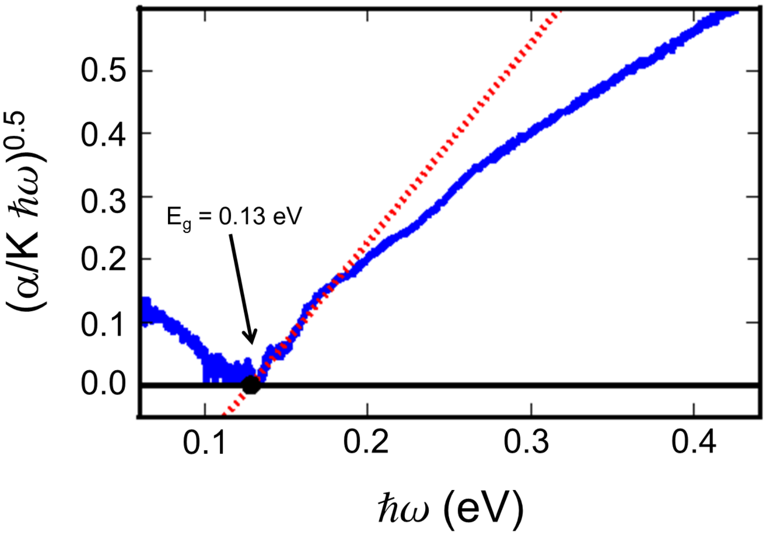

Figure 7.27: Normalized Kubelka Munk function of pure ZrNiSn is shown with the absorption coefficient including the linear fit (red dotted line) which was used to estimate the band gap from the Tauc method [58, 66, 67].

When considering the transition from heavily doped to intrinsically semiconducting behavior ($E_{g,th} < \sim 5\ k_BT$), the Seebeck coefficient is an important indicator of the excitation of minority charge carriers across the thermal band gap. In between these two regions the absolute Seebeck coefficient will reach its maximum (as shown in Fig. 7.25), which then can be used for estimation of the band gap size via the Goldsmid-Sharp formula 7.3. From this formula the band gaps for the $Zr_{1-x}Sc_xNiSn$ solid solution were estimated, using the Goldsmid-Sharp Eq. 7.3 and compared the results with a series of *n*-type *M*NiSn samples from the literature, as shown in Fig. 7.28 [58].

A large difference in the Goldsmid-Sharp thermopower band gap is apparent when comparing Sc-doped *p*-type samples from this work and *p*-type literature results; both of which are much smaller than those estimated by *ab-initio* calculations (∼0.5 eV) [28]. Although the difference might lead one to the conclusion that the choice of dopant will affect the size of the gap, it is important to consider the limitations of the simple Goldsmid-Sharp band gap estimation and the parameters that might affect the results. The Seebeck coefficient for a mixed semiconductor is given as

$$S = \frac{1}{1+\frac{\sigma_n}{\sigma_p}}\left(S_p + \frac{\sigma_n}{\sigma_p}S_n\right) \tag{7.4}$$

where $S_{n,p}$ and $S_{n,p}$ represent the thermopower and the electrical conductivities of the two different

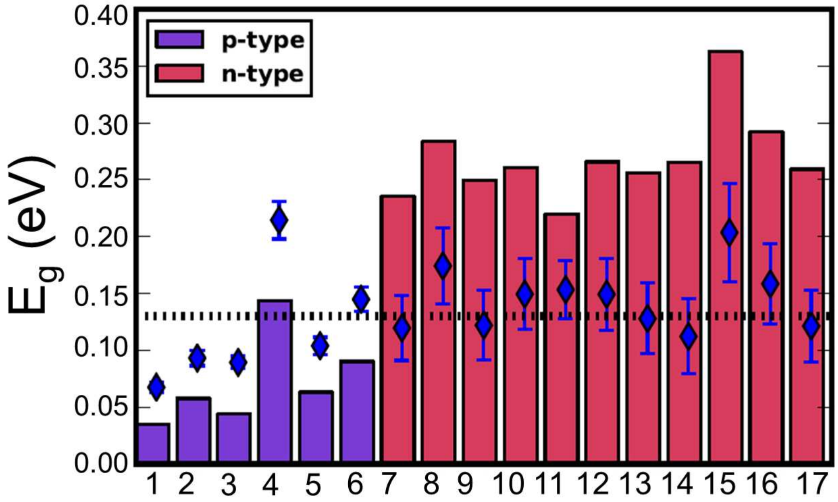

Figure 7.28: Estimation of the band gap for different *n*-type (red bars) and *p*-type (purple bars) half-Heusler compounds using the Goldsmid-Sharp formula ($E_g = 2_e S_{max} T_{max}$) in units of eV *versus*. the numerated HH compounds. The dotted line indicates the optical measured band gap of 0.13 eV for pure ZrNiSn from DRIFTS. The diamonds represent the estimated true band gap value that yields the experimental S_{max} and T_{max} when using the full relation derived by Goldsmid and Sharp for an electron-to-hole weighted mobility ratio of A=5. 1) $Sc_{0.03}Zr_{0.97}NiSn$, 2) $Sc_{0.04}Zr_{0.96}NiSn$, 3) $Sc_{0.05}Zr_{0.95}NiSn$, 4) $Sc_{0.1}Zr_{0.9}NiSn$, 5) $ZrCo_{0.08}Ni_{0.92}Sn$ [44], 6) $ZrCo_{0.12}Ni_{0.88}Sn$ [44], 7) $Zr_{0.75}Hf_{0.25}NiSn$ [68], 8) $Zr_{0.5}Hf_{0.5}NiSn$ [68], 9) $Zr_{0.25}Hf_{0.75}NiSn$ [68], 10) HfNiSn, 11) $Ti_{0.95}Hf_{0.05}NiSn$ [69], 12) $Ti_{0.95}Hf_{0.05}NiSn_{0.995}Sb_{0.005}$ [69], 13) $Ti_{0.95}Hf_{0.05}NiSn_{0.99}Sb_{0.01}$ [69], 14) $Ti_{0.95}Hf_{0.05}NiSn_{0.98}Sb_{0.02}$ [69], 15) $Hf_{0.75}Zr_{0.25}NiSn_{0.99}Sb_{0.01}$ [46], 16) $Hf_{0.5}Ti_{0.25}Zr_{0.25}NiSn_{0.99}Sb_{0.01}$ [46] and 17) $Hf_{0.25}Ti_{0.5}Zr_{0.25}NiSn_{0.99}Sb_{0.01}$ [46, 58].

carrier types, respectively. Goldsmid and Sharp derived a simple model assuming classical statistics [1], which estimates the electron-to-hole conductivity ratio as

$$\frac{\sigma_n}{\sigma_p} = Aexp\left(\eta_n - \eta_p\right) \tag{7.5}$$

where η_n and η_p are the electron and hole dimensionless chemical potentials ($\eta\mu/k_BT$) and μ is the chemical potential. With that, *A* is defined as the weighted mobility ratio.

$$A = \frac{\mu_n N_{v,n}}{\mu_p N_{v,p}} \left(\frac{m_n^*}{m_p^*}\right)^{3/2} \tag{7.6}$$

Where $\mu_{n,p}$ is the electron and hole mobility respectively, N$_{v,n,p}$ is the valley degeneracy of the electron and hole, and $m_{n,p}^*$ is the single valley effective mass (not including the degeneracy of the valence or conduction bands). By substituting equ. 7.5 into 7.6 and taking the classical limit for the Seebeck coefficient and determining its maximum, Sharp and Goldsmid obtain:

$$S = \frac{k_B^2}{e} \frac{\left(\eta_n - r - \frac{5}{2}\right)\left(\eta_g + 2r + 4\right) - \left(-\eta_n - \eta_g - r - \frac{5}{2}\right)}{1 + 2(\eta_g + 2r + 4} \tag{7.7}$$

and:

$$A\ exp\left(2\eta_n + \eta_g\right) = \left(\eta_g + 2r + 4\right)\left[1 \pm \sqrt{1 - \frac{1}{\left(\eta_g + 2r + 4\right)^2}}\right] \approx \left(\eta_g + 2r + 4\right)\left(1 \pm 1\right) \tag{7.8}$$

where η_g is the reduced band gap ($\eta_g = \frac{E_g}{k_BT}$) and *r* is the scattering exponent. In light of the large mobility difference between the *n*-type undoped sample (~25 cm^2/V·s) and the heavily Sc doped samples (*p*-type mobility approximately ~1-2 cm^2/V·s), a conductivity ratio parameter (*A*) that is larger than unity should be considered. In order to investigate this, we first gathered estimates of the Goldsmid-Sharp band gap for a series of of *p*- and *n*-type ZrNiSn samples, as shown by the bars in Fig. 7.28. A clear separation is observed between *p*-type samples ($>$ ~0.05 eV) in purple and *n*-type ones in red ($>$ ~0.2 eV). For reference, the results from the optical measurements are also plotted as a dashed line at ~ 0.13 eV. If for the moment we consider the optical result to represent the true gap, Eq. 7.7 and 7.8 with A = 5 (a reasonable value considering the large mobility difference between electrons and holes) were solved. Using this method, the required true band gap was determined, that would yield the experimental S$_{max}$ and T$_{max}$, the results which are shown as blue diamonds in Fig. 7.28 for a variety of *p*- and *n*-type ZrNiSn-based HH materials. All of these values are close to the measured optical results of 0.13 eV, indicating that the large weighted mobility ratio between electrons and holes is responsible for the large difference in the

Goldsmid-Sharp thermopower band gap when comparing *p*- and *n*-type samples [58].

Although Goldsmid and Sharp state that even with a large mobility ratio value (A = 10), the simple band-gap estimation should hold to within $\sim$ 20%, it should be noted, that they assume a band gap of 10 $k_B T_{max}$ to derive this relation. This is a poor assumption for most materials, as the band gap in ZrNiSn system (and many others) is less than 5 $k_B T_{max}$. In order to illustrate this point, $2eS_{max}T_{max}/E_g$ was plotted *versus* S_{max} for a mobility ratio parameter A = 5 using Eq. 7.6 and 7.8 (Fig. 7.29). The red line is the result for the *n*-type doping and the blue line displays the result for *p*-type doping. Data points in their corresponding colors were taken from their Goldsmid-Sharp band gap ratio to the optical band gap measured in this work (0.13 eV). The displayed error bars assume an error of $\mp$10% in the Seebeck coefficient and the optical band gap. Fig. 7.29 shows an increasing $2eS_{max}T_{max}/E_g$ for the *n*-type samples, whereas it decreases for *p*-types. Qualitatively, this is because the more mobile electrons dominate the Seebeck coefficient equation because it is weighted by their conductivity; this forces the Seebeck of the *p*-type samples to roll over at lower values, whereas *n*-type samples maintain higher Seebeck at higher temperatures. While the news of a very small mobility in *p*-type ZrNiSn may be disheartening, it beneficially results in suppressed bipolar effects in the *n*-type ZrNiSn system. Thus, the low mobility minority carrier enables the *n*-type material to maintain a high thermopower at high temperatures, despite its narrow band gap. This is contrary to the high band gaps found in other *p*-type HHs, like TiCoSb where the band gap estimated from the Goldsmid-Sharp formula is around 0.57 eV [58].

Both *p*-type data from this work and *n*-type literature data for the Seebeck band gap deviated significantly from the optical measurements (0.13 eV), it was shown that this can be simply explained by a large difference in the weighted mobility between electrons and holes. A high electron-to-hole weighted mobility ratio leads to a suppression of the bipolar effect in the thermoelectric transport properties which is essential for high *zT* values in *n*-type *M*NiSn (*M* = Ti, Zr, Hf) HH compounds. Mechanisms to suppress bipolar effects have been discussed to great length in a variety of systems that range from simply changing the band gap or carrier concentration [70], to preferential minority carrier scattering at grain boundaries or nano-inclusions [2, 42]. This work provides a strategy and method for characterizing bipolar suppression, given a material can be doped both *p*- and *n*-type. While there have been efforts to characterize band engineering in materials with a single carrier type, the quality factor analysis has not been extended to valence-conduction band systems. In systems such as Bi_2Te_3, the most common commercial thermoelectric material, both high and room temperature *zT* is limited due to minority carrier activation. Strategies to reduce the minority carrier weighted mobility could provide significant impact on the thermoelectric efficiency.

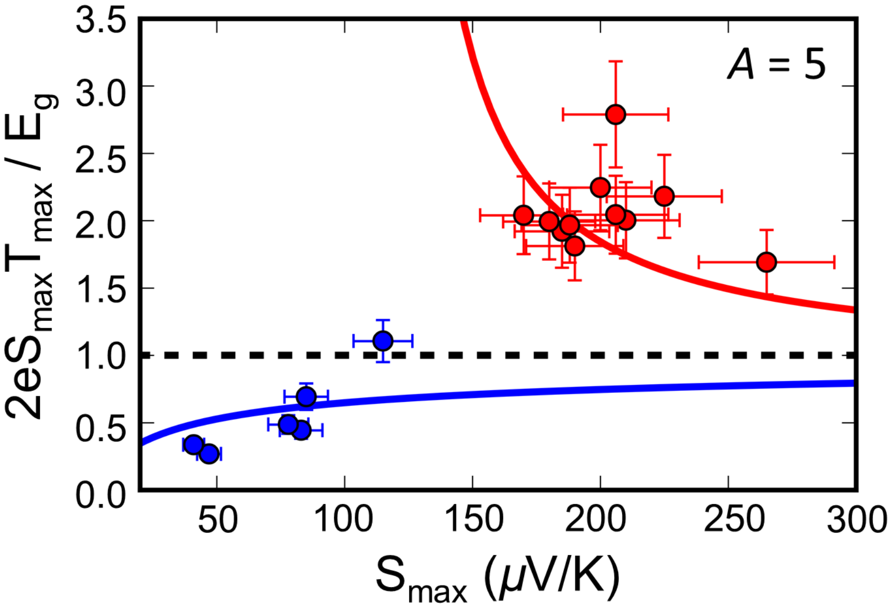

Figure 7.29: A plot of the ratio of the Goldsmid-Sharp band gap (2eS$_{max}$T$_{max}$/E$_g$) to the true band gap for different *n*- and *p*-type half-Heusler compounds in red and blue respectively for an electron-to-hole weighted mobility ratio of A = 5. The solid lines uses Goldsmid and Sharp's full derived equation (Eq. 7.8) to estimate this ratio. Experimental points use the observed maximum Seebeck coefficient (S$_{max}$) and temperature (T$_{max}$) and the optical band gap (E$_{g,optical}$). An error of ∓10% was assumed for the thermopower measurements and the band gap estimations [58].

7.3 La as Acceptor Dopant

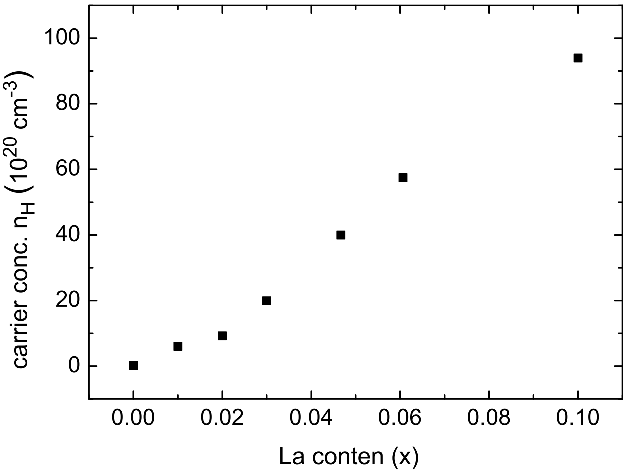

Figure 7.30: With increasing La content, the absolute Hall carrier concentration n_H at 300 K in La$_x$Zr$_{1-x}$NiSn increases.

La is a $5d$ element and with one VE less it can act as an acceptor dopant in ZrNiSn. The *XRD* pattern for the La$_x$Zr$_{1-x}$NiSn solid solutions conform to the well-defined cubic structure typical for the half-Heusler phase. The calculation of the lattice parameter and the crystal structure refinements were done using the Rietveld method. The radii for La and Zr are respectively 1.87 and 1.59 Å. With increasing La content a decline of the lattice parameter was measured, similar to doping with Al on the Sn position and a linear increase of the room temperature carrier concentration was measured (Fig. 7.30. This leads to the assumption that La was not substituted into the lattice.

The increase in the carrier concentration corresponds to an increase in the electrical resistivity for the La$_x$Zr$_{1-x}$NiSn substitutional series (see Fig. 7.31).

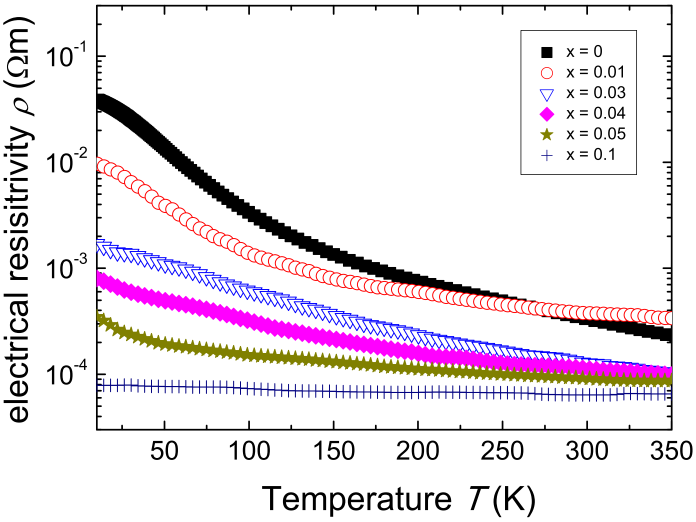

Figure 7.31: TTemperature dependence of the electrical resistivity in the $\mathrm{La}_x\mathrm{Zr}_{1-x}\mathrm{NiSn}$ (x = 0 - 0.1) solid solution from 10 to 350 K.

The temperature dependence of the Seebeck coefficient α for the La solid solutions is exemplified in Fig. 7.33 a). The Seebeck coefficient is negative over the whole temperature range, indicating that electrons are the major charge carriers. The maximum Seebeck coefficient of -290 μV/K was measured for the parent compound ZrNiSn. The unsubstituted La is responsible for the shift of the maximum Seebeck coefficient toward higher temperatures. While the electrical resistivity decreased with increasing La content, the absolute Seebeck coefficient was reduced, according to the Mott formula [54]. Due to the fast decrease in the electrical resistivity and the rather slow one of the absolute Seebeck coefficient the power factor of the x = 0.03; 0.04 and 0.05 samples exceeds the one of pure ZrNiSn (see Fig. 7.33). The highest power factor in the La-substitutional series could be measured for the 3 at.% sample. It is assumed that the power factor of these samples will continue to increase until bipolar effects will set in.

Fig. 7.32 a) shows the temperature dependence of the total thermal conductivity κ_{tot} with increasing La content. The slight decrease with increasing La content is associated with additional phonon scattering. For samples with $\geqslant$ 3 at.% La the room temperature value of the thermal conductivity increases. This is associated with an increase of the electrical part of the thermal conductivity induced by the increased electrical conductivity. κ_e is correlated to the electrical resistivity by the Wiedemann-Franz law (see Eq. 5.11). The calculated dimensionless figure of merit, zT, according to Eq. 5.3 is shown in Fig. 7.32 b). Due to the improved power factor, the zT values are improved

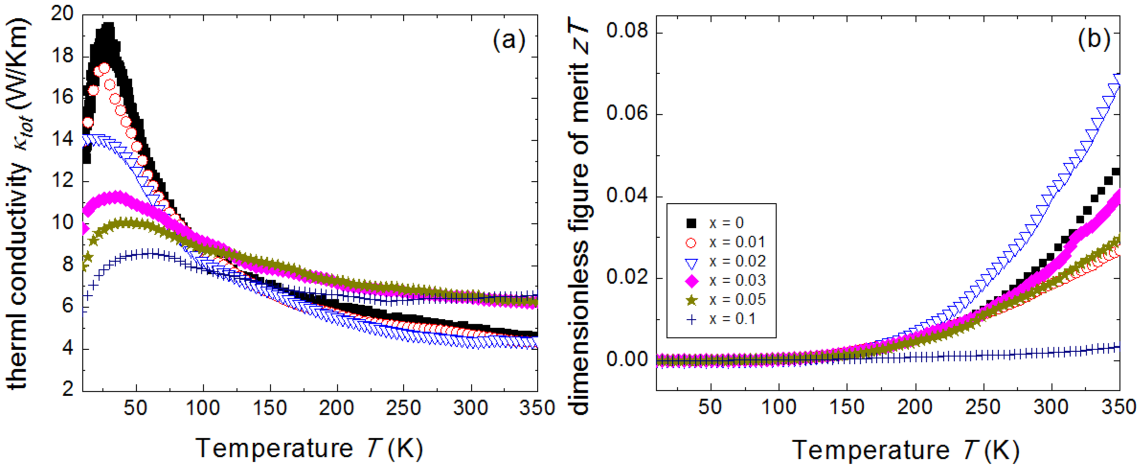

Figure 7.32: Temperature dependence of the total thermal conductivity κ_{tot} a) and the dimensionless figure of merit, zT, b) in the La$_x$Zr$_{1-x}$NiSn (x = 0 - 0.1) solid solution from 10 to 350 K.

as well. Even though the total thermal conductivity with high La condent influence zT negatively, the decrease in theelectrical resistivity was enough to compensate for it. The maximum zT value was reached for the undoped ZrNiSn sample.

The effect of La substitution on the thermoelectric properties of the La$_x$Zr$_{1-x}$NiSn (x = 0 - 0.1) (x = 0 - 0.1) were systematically studied. The decrease in the lattice parameter leads to the assumption that La was not completely substituted into the structure. The strong decrease in the electrical resistivity lead to the improvement of the power factor $\alpha^2\sigma$ and the dimensionless figure of merit, zT. La substitution did not lead to *p*-type behavior in the La$_x$Zr$_{1-x}$NiSn solid-solution. Even though $\alpha^2\sigma$ and zT were both improved bipolar effects will cause a roll-over in the thermoelectric properties around 500 K, due to the small band gap in substituted ZrNiSn compounds.

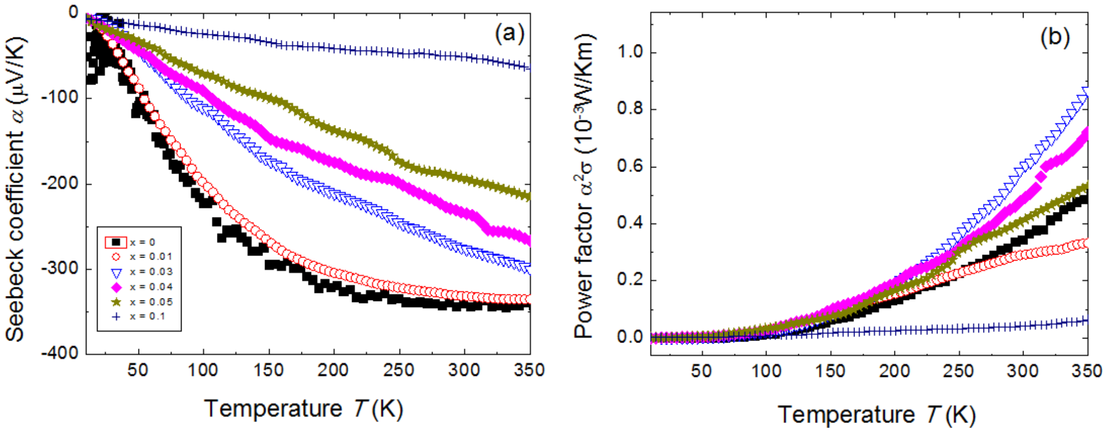

Figure 7.33: Temperature dependence of the Seebeck coefficient α a) and the power factor $\alpha^2\sigma$ b) in the $La_xZr_{1-x}NiSn$ (x = 0 - 0.1) solid solution measurend in the temperature range 10 to 350 K. Due to the improved electrical resistivity the power factor of the x = 0.03; 0.04 and 0.05 samples exceeds the measured values of pure ZrNiSn.

8 Phase Separating p-type Half-Heusler Compounds

8.1 Acceptor doping with Sc in Phase-separated Half-Heuslers

Previously the *M*NiSn system was used to study the influence of different acceptor elements and their thermoelectric properties. The best results could be achieved when using Sc as acceptor dopant (see chapter 7.2.2).

Pure *M*NiSn possess fairly high thermal conductivities and therefore inhibits the possibility of achieving high thermoelectric efficiencies for NiSn-based HH compounds. A new approach for a further improvement needs to be found, for the reduction of the thermal conductivity and with this enhancing the electrical properties. As proposed by *Dresselhaus* and *Slack* [29, 71, 72, 73] in the early nineties many efforts in improving the thermoelectric efficiencies have been driven towards nanostructuring and -inclusions [74, 75, 76]. However, the thermal stability and reproducibility has not been confirmed yet [72]. It would be beneficial to find a system, whose properties are thermally stable over many heating and cooling cycles. A system, that due to its structural peculiarities possesses a low thermal conductivity and a high thermoelectric efficiency, which are given to begin with. Phase-separated HH compounds comply with many of these requirements [77] and have been investigated in the recent past [22, 36, 78, 79]. $\text{Ti}_x\text{Zr}_y\text{Hf}_z$NiSn-based complex HH compounds exhibit an intrinsic phase separation, and the dentritic microstructure can be maintained under cycling conditions [77]. Most of the improvements in phase-separated HH materials have been attained, due to Sb substitution for Sn, leading toward high zT values of 1.5 at 700 K [36, 39]. As the system is NiSn-based it is expected that bipolar effects will have a significant impact on the thermoelectric properties. This chapter will focus on the introduction of Sc into these phase-separated HH and the resulting change in their TE properties. $\text{Ti}_{0.5}\text{Zr}_{0.25}\text{Hf}_{0.25}$NiSn [36] was chosen, because of its already low thermal conductivity, high Seebeck coefficient and the stability of the phase separation [77]. It was assumed that the introduction of Sc into the systems will lead to the formation of a *p*-type, which would be able to compete with other state-of-the-art *p*-type materials.

8.1.1 The Phase Separation

As ternary HH possess a fairly high thermal conductivity, which inhibits these systems to reach high thermoelectric efficiencies, research has shifted more and more towards multi-component [22, 23, 79, 78] or phase-separating HH compounds[17, 36, 39, 77, 80]. The low thermal conductivity in these systems is a result of multiple scattering effects, like mass and strain effects, as well as boundary scattering at different interfaces, leading to a low thermal conductivity and with that to a high TE efficiency.

HH typically separate into two phases: a Zr-Hf-rich primory phase (HH1) and a Ti-rich secondary phase (HH2) shown in Fig. 8.1. The interested reader is referred to secondary literature on phase separating HH [77, 36, 39, 17, 80, 56].

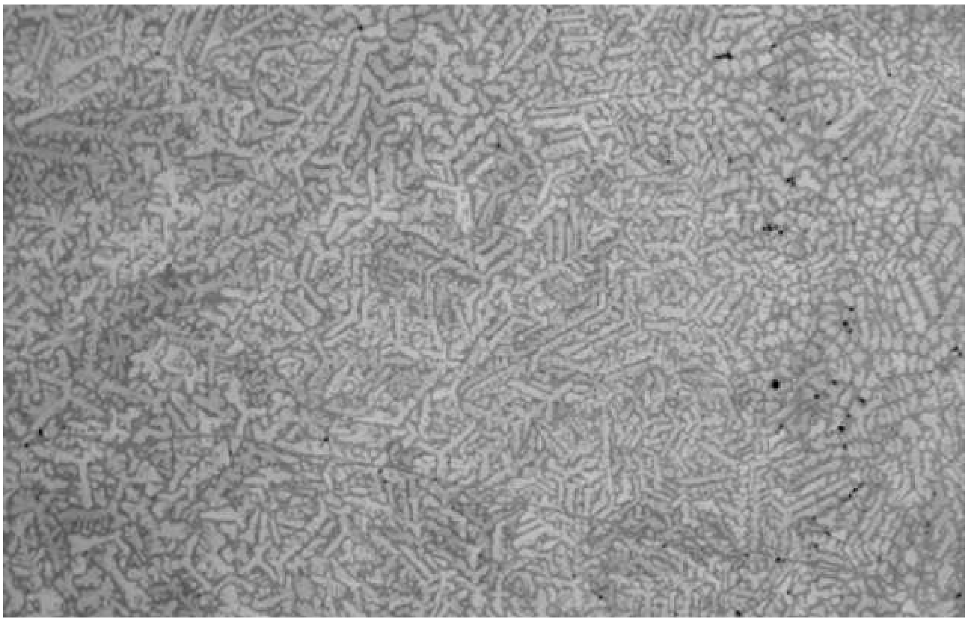

Figure 8.1: The back scattering image of $Ti_{0.5}Zr_{0.25}Hf_{0.25}NiSn$ shows a clear phase separation into two HH compounds (HH1 (grey) and HH2 (dark grey)).

8.1.2 Transport Properties of $Ti_{0.5}Zr_{0.25}Hf_{0.25}NiSn$

The investigation of the **low temperature transport properties** of $(Ti_{0.5}Zr_{0.25}Hf_{0.25})_{1-x}Sc_xNiSn$ (x = 0 - 0.05) are shown in Fig. 8.2. The total thermal conductivity of undoped $Ti_{0.5}Zr_{0.25}Hf_{0.25}NiSn$ exhibits a maximum at 30 K, resulting from long wavelength phonons. At high enough temperatures the thermal conductivity decays with a 1/T temperature dependence, due to phonon-phonon scattering. These temperature trends can be observed best in the undoped sample. Substitution with Sc results in a reduction of κ and a suppression of this maximum at 30 K. The Seebeck coefficient α (Fig. 8.2 b) switches signs for 2 at.% Sc from -235 μV/K to + 190 μV/K, where +190 μV/K is a remarcabley high value for a *p*-type material. As observed in ternary HH systems as well, even small amounts of Sc lead to a sign inversion of the Seebeck coefficient, due to a reduction of electrons in the system. This confirms again, that Sc is the most promising dopant to create a *p*-type HH in the *M*NiSn-based system. For a substitution level of 3 at.% Sc the Seebeck coefficient stays positive over the whole temperature range, indicating that holes are the dominant charge carriers, with a maximum at 180 K. This maximum gets shifted to high temperatures, with increasing Sc content, which leads to the appearance of an almost linear Seebeck coefficient. The power factor and figure of merit are shown in Fig. 8.2 c) and d). The sample with 2 at.% Sc exhibits a unusually high $\alpha^2\sigma$ and *zT* for a *p*-type material, due to the increased electrical conductivity and the reduced thermal conductivity. However, even though the absolut Seebeck coefficient could be improved, all *p*-type materials show a less ample thermoelectric efficiency, due to bipolar contributions. This bipolar conduction should be even more pronounced in $(\text{Ti}_{0.5}\text{Zr}_{0.25}\text{Hf}_{0.25})_{1-x}\text{Sc}_x\text{NiSn}$ substitutional series, due to the decreased band gap size of $\text{Ti}_{0.5}\text{Zr}_{0.25}\text{Hf}_{0.25}\text{NiSn}$ (see Fig. 8.3) comparedto ZrNiSn.

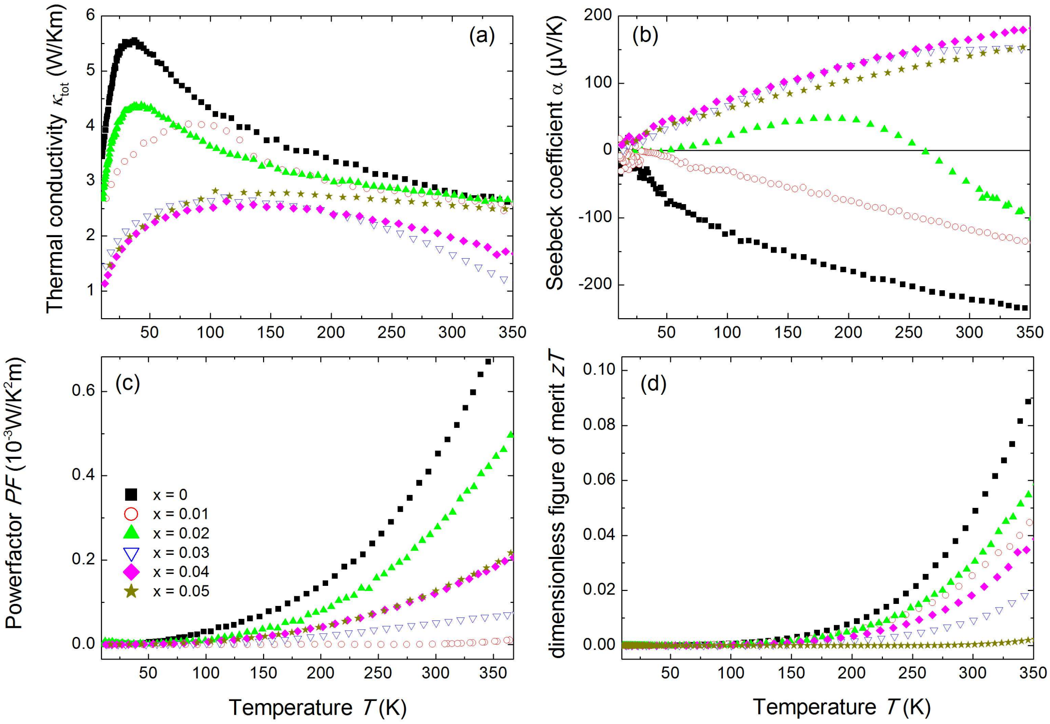

Figure 8.2: Low temperature dependence of phase-separated $(\text{Ti}_{0.5}\text{Zr}_{0.25}\text{Hf}_{0.25})_{1-x}\text{Sc}_x\text{NiSn}$ (x = 0 - 0.05) half-Heusler compounds. a) shows the total thermal conductivity κ, b) Seebeck coefficient α, c) the power factor $\alpha^2\sigma$ and d) the dimensionless figure of merit, *zT*. The introduction of Sc leads to a reduction of the total thermal conductivity and to an inversion of the Seebeck coefficient with the highest value for the 4% Sc sample of $+190\ \frac{\mu V}{K}$ at 350 K.

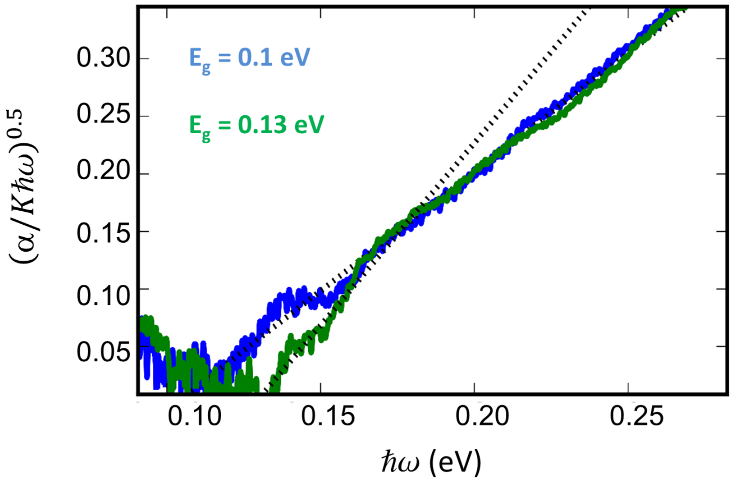

Figure 8.3: Optical diffuse reflectance data plotted as the indirect band gap transformation of the Kubelka Munk function for pure ZrNiSn and the phase-separated HH compounds. A linear fit (black dotted line) was used to estimate the band gap by extrapolating to zero absorption, indicating the band gap is 0.13 eV for ZrNiSn and 0.1 eV for phase-separated compound. The band gap measurements were done by Zachary M. Gibbs at the California Institute of Technology in Pasadena, CA, USA.

8.1.3 Comparison of the p-type ZrNiSn Solid Solution with its Phase-Separated Counterpart

From the investigation of the TE properties of the $Zr_{1-x}Sc_xNiSn$ (x = 0 - 0.10) solid solution and the phase-separated $(Ti_{0.5}Zr_{0.25}Hf_{0.25})_{1-x}Sc_xNiSn$ (x = 0 - 0.05) system the *p*-type samples with the best overall performance are compared. The result of the comparison are shown in Fig. 8.4 and 8.5 in the temperature range from 300 K to 850 K. At RT all samples exhibit a high electrical resistivity, which decreases with increasing temperature for all the samples, indicating semiconducting behavior. For the substituted samples the temperature dependence of the resistivity decreases compared to the undoped samples, pointing to a shift of the Fermi energy towards the valence band as a result of increasing *p*-type carriers. The Hall mobility is suppressed and becomes positive by the addition of holes. The parent compound *n*-type ZrNiSn and $Ti_{0.5}Zr_{0.25}Hf_{0.25}NiSn$ exhibit the highest mobilities, with a value at room temperature of -25 cm^2/Vs and -30 cm^2/Vs, which is a typical value for *n*-type *M*NiSn-based systems [66, 68]. This value is still significantly lower than 150 cm^2/Vs for Bi_2Te_3 or 900 1400 cm^2/Vs for PbTe [60, 61].

Since the effective mass varies inversely with the curvature of the bands, a high effective mass is the result of shallow or flat bands, whereas a small effective mass is typical for highly dispersed bands. Based on *ab initio* calculations, a high mobility value for *n*-type ZrNiSn and $Ti_{0.5}Zr_{0.25}Hf_{0.25}NiSn$ is expected owing to their light conduction band. The valence band, however, has been shown to have a higher effective mass, and so by substituting Zr with Sc, one might expect a lower mobility (in magnitude) for *p*-type materials as the Fermi level gets shifted into the valence band at Γ [28, 81]. This is consistent with the experimental results, shown in Fig. 8.4; the Hall mobilities of the heavily Sc-doped samples are much lower in magnitude than the undoped samples. In general, the transport properties of materials with small band gaps are influenced by both types of carriers [63], with a higher weight given for the carriers with higher mobility (see Fig. 8.3). Thes bipolar effects are caused by the rather small band gaps of ZrNiSn and $Ti_{0.5}Zr_{0.25}Hf_{0.25}NiSn$ of 0.13 eV and 0.1 eV respectively. Hence, these bipolar effects cause a strong increase of the carrier concentration above 600 K (see Fig. 8.4). This multiple carrier conduction leads to a corruption of the estimated carrier desitiy. Because the individual carrier contributions, $n_{n,p}$ and $\mu_{n,p}$, are unknown and difficult to determine, using the expression for a single carrier type (Eq. 6.2) will result in a value that is greater than the true value for n_p or n_n.

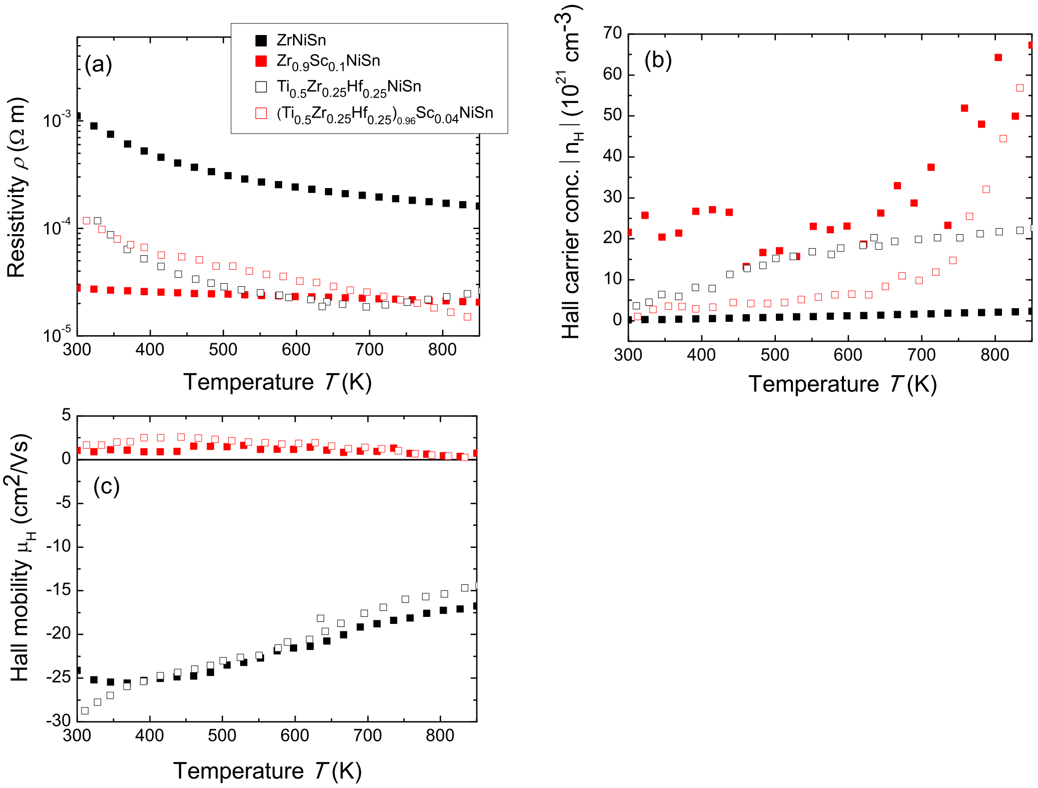

Figure 8.4: Comparision of the high temperature dependence of the Sc subsituted ternary and phase-separated half-Heusler compounds. a) shows the electrical resistivity, b) Hall carrier concentration and c) the Hall mobility. The Hall mobility is largest for the undoped samples, the magnitude of the mobility decreases as a result of the influence of the introduced holes.

As expected the ternary HH solid solutions are the ones with the highest thermal conductivity. Through introduction of Sc into ZrNiSn the total thermal conductivity could be lowered, owing to additional scattering centers. The minimum κ_{tot} is shifted toward lower temperatures, due to a stronger bipolar contribution, consistent with the coexistence of both electrons and holes (as evident from Fig. 7.24 a). The shift of the onset of bipolar conduction to lower temperatures is assumed to be caused by the higher sensitivity of the thermal conductivity to bipolar effects and can be observed for the phase-separated HH systems as well. The low thermal conductivity of the phase-separated HH is caused by an intrinsic phase separation into two HH phases (a Zr-Hf-rich primary phase (HH1) and a Ti-rich phase (HH2)), with additional phonon scattering, reducing the overall thermal conductivity significantly (for comparision see the black curves in Fig. 8.5 a).

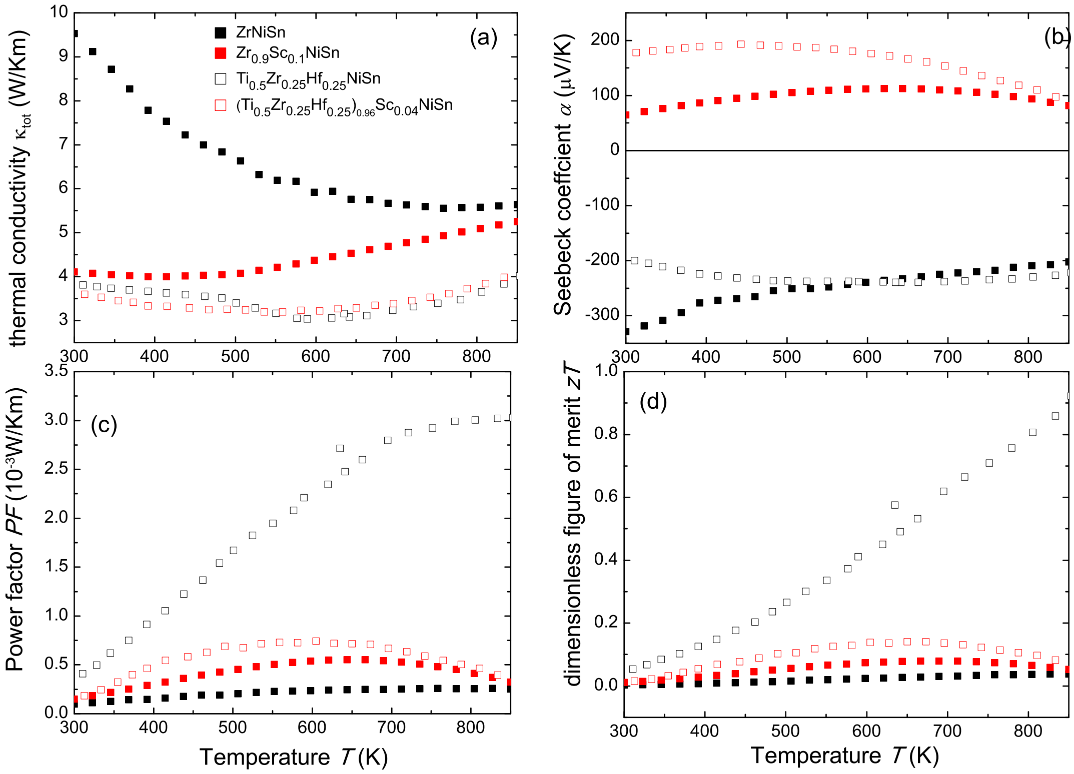

Figure 8.5: Comparision of the high temperature dependence of the Sc subsituted ternary and phase-separated half-Heusler compounds. a) shows the total thermal conductivities κ, b) the Seebeck coefficients α, c) the power factors and d) the dimensionless figure of merits. The introduction of Sc leads to a reduction of the total thermal conductivity and an inversion of the Seebeck coefficients form *n*- to *p*-type for both systems.

For both samples the Sc doping causes a sign inversion for the Seebeck coefficient from *n*-type to *p*-type, where holes become the predominant charge carriers. Whereas for the ternary compound 10 at.% Sc were needed for a sufficiently high Seebeck coefficient, only 4 at.% Sc were used for the phase-separated HH compound. This is believed to be caused by the different influence of the Sc on the two different half-Heusler phases (HH1 and HH2) and by the fact that the contribution of both phases adds up to a cumulative Seebeck coefficient, according to following equations:

$$\alpha_{total} = \frac{\alpha_{HH1}\sigma_{HH1} + \alpha_{HH2}\sigma_{HH2}}{\sigma_{HH1} + \sigma_{HH2}} \tag{8.1}$$

with

$$\alpha_{HH1} = \frac{\alpha_{HH1,n}\sigma_{HH1,n} + \alpha_{HH1,p}\sigma_{HH1,p}}{\sigma_{HH1,n} + \sigma_{HH1,p}} \tag{8.2}$$

and

$$\alpha_{HH2} = \frac{\alpha_{HH2,n}\sigma_{HH2,n} + \alpha_{HH2,p}\sigma_{HH2,p}}{\sigma_{HH2,n} + \sigma_{HH2,p}} \tag{8.3}$$

where $\sigma/\alpha_{HH1/2,n/p}$ are the electrical conductivities and Seebeck coefficients of the two different HH phases and the two carriers. This is similar to the equation for mixed conduction 7.1. Whereas here, the contribution of two carrier types of each individual half-Heusler phase (HH1 and HH2) contributes to the overall thermoelectric properties.

Fig.8.5 shows, that the power factor of the ternary ZrNiSn system could be improved through Sc substitution. $\alpha^2\sigma$ was lowered in the case of the phase-separated system, caused by the diminished electrical conductivity. Similar is the observation for *zT*, where it could be improved for ZrNiSn, due to the decreased thermal conductivity and improved electrical conductivity. Yet the phase-separated system, shows no enhancement of the figure of merit. The most important reason for this is the early onset of the bipolar conduction caused by the even smaller band gap (see Fig. 8.3), which effects both Seebeck coefficient and thermal conductivity strongly at high temperatures. Both quantities decline significantly leading to low values for *zT* and $\alpha^2\sigma$ (see Fig. 8.3).

8.2 Optimization of Acceptor Doped Samples

The experimental transport data for *p*-type doped HH were analayzed using the common solution to the Boltzmann transport equation (see chapter 6.3) within a relaxation time approximation. Assuming that the transport properties are generated by a single heavy hole conduction band. With this assumption the Seebeck coefficient for $Sc_{0.10}Zr_{0.9}NiSn$ and $(Ti_{0.5}Zr_{0.25}Hf_{0.25})_{0.96}Sc_{0.04}NiSn$ was modeled, by assuming an effective mass for the VB of 6 m_e.

The temperature dependence of the Seebeck coefficients for Sc substituted ternary and phase-separated HH compounds are exemplified in Fig. 8.6. The solid green line represents the calculated values for the temperature dependent Seebeck coefficient assuming a SPB model. It can be seen that α deviates strongly from the experimental data above 500 K for both samples, signaturing the the onset of bipolar effects and the invalidity of a SPB model for *p*-type samples.

As it is known from chapter 7.2.2, the transport properties of *p*-type samples are influenced by two carrier types (holes and electrons) owing to the introduction of holes into intrinsic *n*-type ZrNiSn and $Ti_{0.5}Zr_{0.25}Hf_{0.25}NiSn$. Thus, the transport properties are dominated by the high mobility of the electrons over that of the holes, which can be seen from the Hall mobility in fig 8.4.

Hence, a two parabolic band model for two non-degenerate bands was used, where the different effective masses and mobilities for the CB and VB were taken into account. A two band model was used despite the band structure being more complicated (see Fig. 5.11). The results of these calculations are shown in Fig. 8.6 as solid blue lines. As the temperature increases the used two band model tends to underestimate the Seebeck coefficient, caused by bipolar effects at high temperatures, signaturing the invalidity of a two parabolic band model. The deviation for both models is caused by the non-parabolicity of the valence band.

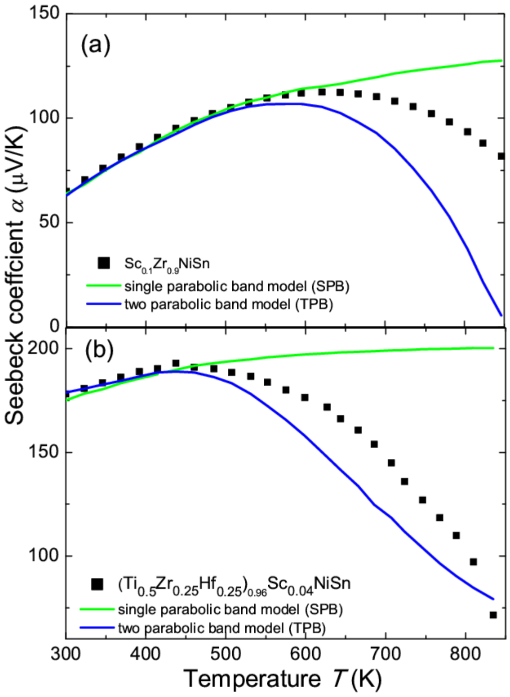

Figure 8.6: Comparision of the high temperature dependence of the measured and the calculated Seebeck coefficient for $Sc_{0.10}Zr_{0.9}NiSn$ and $(Ti_{0.5}Zr_{0.25}Hf_{0.25})_{0.96}Sc_{0.04}NiSn$. The solid lines where calculated using a effective mass for the valence band of $m^* = 6\ m_e$ and for the conduction band $m^* = 3\ m_e$ under acoustic phonon scattering dominated assumption of the SPB (green) and two band model (blue).

The low and high temperature thermoelectric transport properties of Sc substituted phase-separated HHs showed, that the substitution of Ti/Zr/Hf by Sc lead to a successful introduction of holes into the system. The phase-separated HH compound showed a maximum Seebeck coefficient of $+190$ $\frac{\mu V}{K}$ at 350 K, reaching almost $+\ 200$ $\frac{\mu V}{K}$ at elevated temperatures. At high temperatures the higher mobile electrons are thermally activated across the band gap, causing a role over of the Seebeck coefficient in temperature for both systems. Generally the transport properties are dominated by the high mobility of the electrons over that of the holes (see section 7.2.3). Due to a low thermal conductivity, phase-separated HH compounds provide a promising starting material for the investigation of a competitive *p*-type for TE applications. The obtained results show, that a further improvement of the *p*-type properties could be achieved. The Seebeck coefficient at room temperature of the phase-separated HH system could be doubled compared to the ternary one. The experimental data from both systems were analyzed within a SPB and two band model approach. Fig. 8.6 showed that α deviates strongly from the experimental data above 500 K for both samples, signaturing the the onset of bipolar effects and the invalidity of the SPB and two band model model for *p*-type samples. It is assumed, that a non-parabolic Kane band model would describe the results obtained for *p*-type HH more effectively, under the consideration that the transport properties are influenced by four bands (see Fig. 8.7).

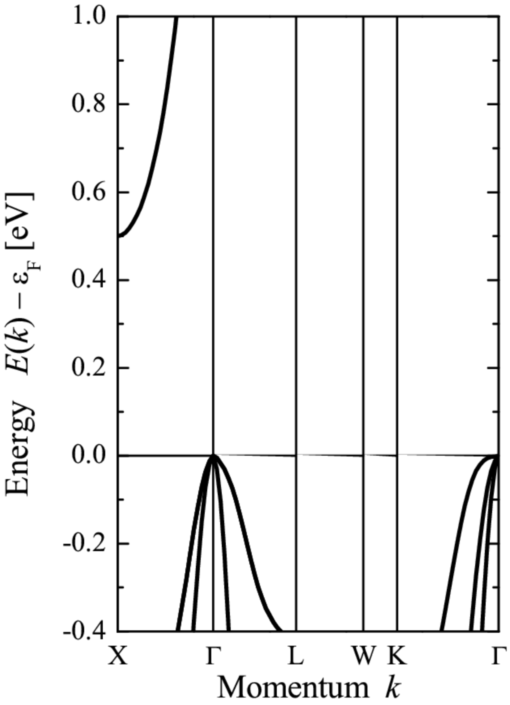

Figure 8.7: Shown is the electronic structure of NiSn-based HH on an enlarged scale to accentuate, that the thermoelectric properties are effected by multiple bands. The *ab-initio* calculations were provided by Dr. G. Fecher from the Max-Planck Institute for Chemical Physics of Solids.

In general it is reasonable to speculate that the introduction of Sc into a half-Heusler system with a bigger band gap, for instance the *M*CoSb compounds, would lead to *p*-type materials where the onset of bipolar effects is shifted to much higher temperatures compared to *M*NiSn compounds. Also an introduction of a phase separation in *M*CoSb could proof to be the key for efficient high temperature *p*-types.

9 Modeling the High Temperature Thermoelectric Properties of Half-Heuslers

Introduction

Theoretical evaluations of the thermoelectric transport properties of half-Heusler alloys from *ab-initio* calculations and the Boltzmann transport theory can be used as an origin for the investigation of existing and new materials [82]. Of more importance for any experimentalist is a layout for analyzing their thermoelectric transport data at any given temperature. Since Jeffery G. Snyder's work [9] a high interest has sparked in the prediction of a materials transport properties within a conventional transport theory, which is a powerful tool when analyzing the materials properties. The model used is most accurate in the region of a single carrier type and when the Fermi level is situated in a relatively parabolic and isotropic region of the electronic band structure. The results of such an analysis might give more insight into more complex behavior affecting the transport properties. As this is the case for *p*-type doped HH. Not only are there mulit-band effects with varying band masses present in these compounds (see Fig. 5.11), additionally the valance band is non-parabolic making the modeling of the transport data rather complicated. Hence, the focus of this chapter lies on analyzing the high temperature thermoelectric transport properties of various *n*-type half-Heusler compounds. For *n*-type HH a simple parabolic dispersion relationship (free electron behavior) can be assumed.

Inspired by the promising thermoelectric properties of *n*-type phase-separated half-Heusler materials from the pervious chapter, the influence of electron doping in the $\mathrm{Ti}_{0.3-x}\mathrm{Zr}_{0.35}\mathrm{Hf}_{0.35}\mathrm{NiSn}$ compound was investigated. The measurement of the high temperature data (Seebeck coefficient, thermal conductivity and electrical resistivity) were done by Julia Krez, as well as the sample preparation.

As mentioned before, phase-separated HH fulfill many requirements on modern thermoelectric materials, like low thermal conductivities, thermal stability, reproducibility and environmentally friendliness. The improvements in TE performance in these compounds is mainly due to the reduction of the thermal conductivity caused by an intrinsic phase separation [21, 80, 83, 36]. Therefore, this material class builds the ideal origin for further improvement of their *n*-type TE properties and has been intensively studied since their discovery [22, 79, 78]. An intrinsic phase separation can be obtained in most complex $\mathrm{Ti}_x\mathrm{Zr}_y\mathrm{Hf}_z\mathrm{NiSn}$-based HH, with a stable microstructure through different heating and cooling cycles [77]. It has been shown, that their transport properties can be enhanced even further, by electron doping, pushing the zT above unity [36, 80]. However, their high temperature transport properties are limited as well by their band gap (0.15-0.23 eV [34]) and the onset of bipolar conduction. To suppress the contribution of bipolar conduction the influence of Nb on the TE properties was investigated with the hope to shift the onset of bipolar conduction to higher temperatures.

The $Ti_{0.3-x}Nb_xZr_{0.35}Hf_{0.35}NiSn$ (x = 0 - 0.05) system was synthesized and an intrinsic phase separation was observed as a result of the intermixing of Ti, Zr and Hf. The TE properties were measured up to 850 K. Electron probe microanalysis (EPMA) and XRD measurements of the samples revealed a Zr-Hf rich main phase (HH1), which was dendritically interlaced with a Ti-rich phase (HH2) [80, 41] along with homogeneously distributed Nb inclusions. An average effective mass model was developed for the phase-separated The $Ti_{0.3-x}Nb_xZr_{0.35}Hf_{0.35}NiSn$ (x = 0 - 0.05) system and compared with other Nb substituted HH compounds. Within the framework of the used transport model the optimized carrier concentration was found for this system. The data presented in this work has been submited to the journal of Material Chemistry A and can be viewed online [17].

9.1 Characterization of n-type Phase-Separated HH

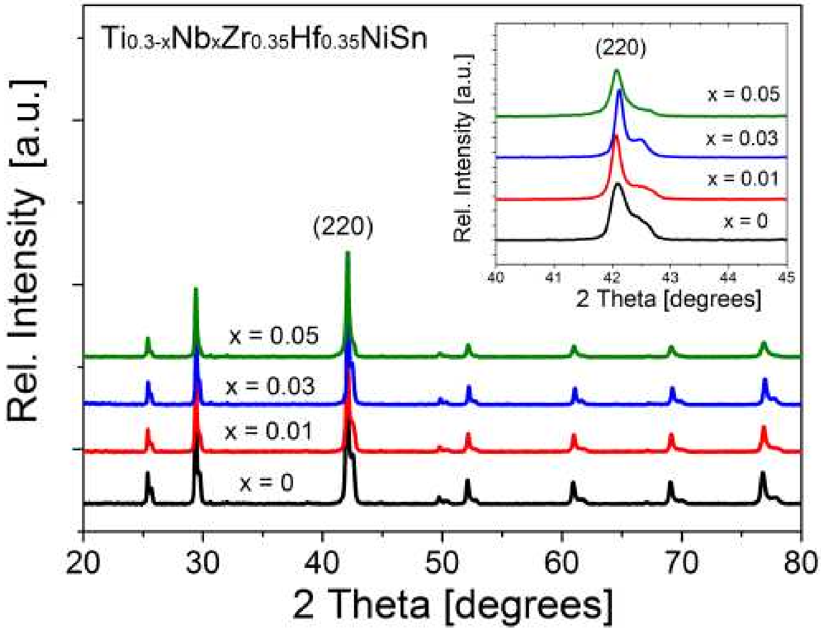

Figure 9.1: *XRD* pattern of $Ti_{0.25}Nb_{0.05}Zr_{0.35}Hf_{0.35}NiSn$. The inset shows the splitting of the (220)-reflex, caused by the intrinsic phase separation into a Zr-Hf rich phase (HH1) and a Ti-rich phase (HH2) [17].

XRD measurements verified the crystalline structure in the $Ti_{0.3-x}Nb_xZr_{0.35}Hf_{0.35}NiSn$ (x = 0, 0.01, 0.03 and 0.05) with a splitting of the Bragg reflection peaks caused by coexistence of two HH phases (HH1 and HH2) due to the intrinsic phase separation [80, 41] (see Fig. 9.1). The lattice constant a of $Ti_{0.25}Nb_{0.05}Zr_{0.35}Hf_{0.35}NiSn$ was estimated by a refinement of the peak positions and found to be 6.068 Å and 6.001 Å respectively. The *XRD* measurements and the refinement was done by Julia Krez. A decrease in the lattice parameter could be observed with increasing Nb content, leading to the assumption that a successful substitution of Nb into the lattice was not attained. The radii of Ti and Nb are 1.44 Å and 1.43 Å, thus a substitution of Nb for Ti should not cause a change of the lattice constant, leading to assumption that Nb was not substituted into the lattice [17].

The electron probe microanalysis (EPMA) of the samples revealed a seperation into a Zr-Hf rich main phase (HH1), dendritically interlaced by a Ti-rich phase (HH2) [80, 41] along with homogeneously distributed Nb inclusions. To emphasize the presence of Nb, the samples were etched with a HCl:HNO_3:HF:H_2O solution as shown in (Fig.9.2 a). The EPMA analysis confirmed, that Nb was not substituted into the lattice.

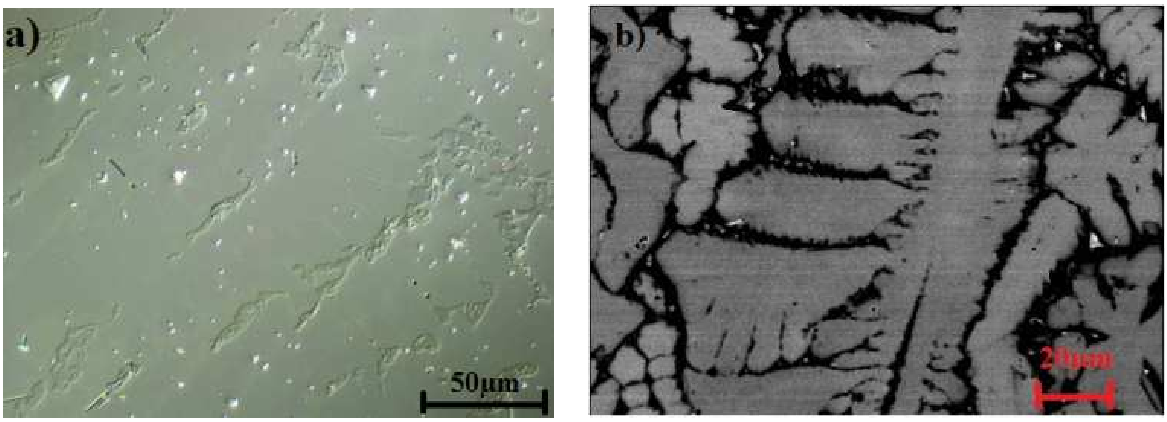

Figure 9.2: a) shows the light microscope image of the $Ti_{0.25}Nb_{0.05}Zr_{0.35}Hf_{0.35}NiSn$ etched with a HCl:HNO3:HF:H_2O solution to highlight the metallic Nb inclusions and b) the BSE image of the phase-separated microstructure in the $Ti_{0.3}Zr_{0.35}Hf_{0.35}NiSn$ HH system, consisting of the Zr-Hf-rich main phase (HH1, grey) with the dendritically interlaced Ti-rich phase (HH2, black) [17].

9.2 High temperature transport measurements of $Ti_{0.3-x}Nb_xZr_{0.35}Hf_{0.35}NiSn$

The results of the electrical conductivity σ measurements of $Ti_{0.3-x}Nb_xZr_{0.35}Hf_{0.35}NiSn$ (x = 0, 0.01, 0.03 and 0.05) are shown in Fig. 9.3. The parent compound, $Ti_{0.3}Zr_{0.35}Hf_{0.35}NiSn$, exhibits an intrinsically semiconducting behavior, as σ increases with temperature. The addition of Nb drastically increases the value of σ at room temperature and facilitates the transition from intrinsically conducting to a metal-like behavior. The increase of the electrical conductivity with the addition of Nb is compensated by a systematic decrease of the room temperature Seebeck coefficient α.

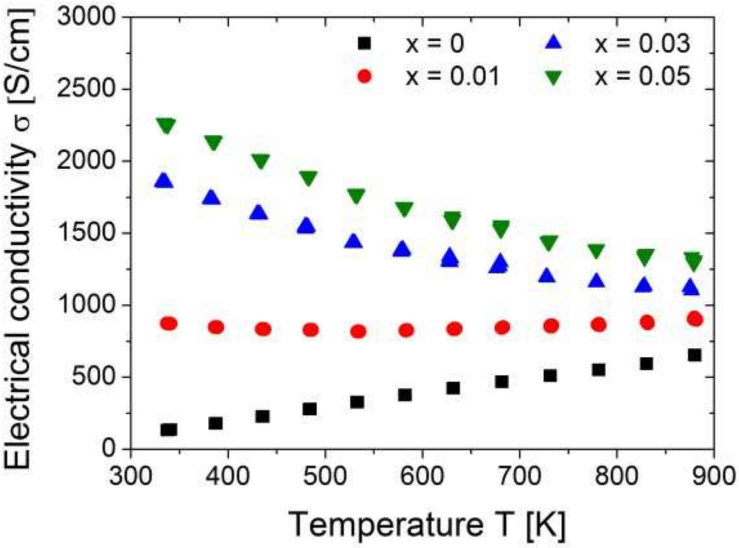

Figure 9.3: Temperature dependence of the electrical conductivity σ in the Ti$_{0.3-x}$Nb$_x$Zr$_{0.35}$Hf$_{0.35}$NiSn (x = 0, 0.01, 0.03 and 0.05) system from 300 to 900 K. The electrical conductivity becomes more metallic with increasing Nb concentration [17].

The temperature dependence of α for all samples exemplified in Fig. 9.4, revealed negative values over the whole temperature range, which indicated that electrons are the majority carriers. The maximum Seebeck coefficient of -240 $\frac{\mu V}{K}$ was measured for the parent compound Ti$_{0.3}$Zr$_{0.35}$Hf$_{0.35}$NiSn. The metallic inclusions were responsible for attaining the maximum Seebeck coefficient at higher temperatures than before. Caused by the suppression of the minority carrier conduction above the usual temperature of around 600 K [79].

While, σ increased with increasing Nb concentration, the absolute value of the Seebeck coefficient was reduced, though not at a similarly fast rate, leading to an improvement of the power factor (Fig. 9.5). The power factors were calculated from the relation $PF = \alpha^2\sigma$ and are shown in Fig. 9.5. By comparing the samples with Nb content to the parent compound without Nb, it can be seen that the ones with metal inclusions exhibit a significant enhancement of the power factor. The highest power factor was obtained for the sample with 5 % Nb content.

Fig. 9.6 shows the temperature dependence of the thermal conductivity ($\kappa = \kappa_e + \kappa_l$) with increasing Nb content (according to the Wiedemann-Franz Law 5.11=. Therefore, the observed increase of the total thermal conductivity can only be explained by an increase in κ_e, induced by the metallic Nb inclusions observed in the system. The influence of bipolar conduction, which is derived from the thermal excitation of minority carriers, can only be observed in the parent compound

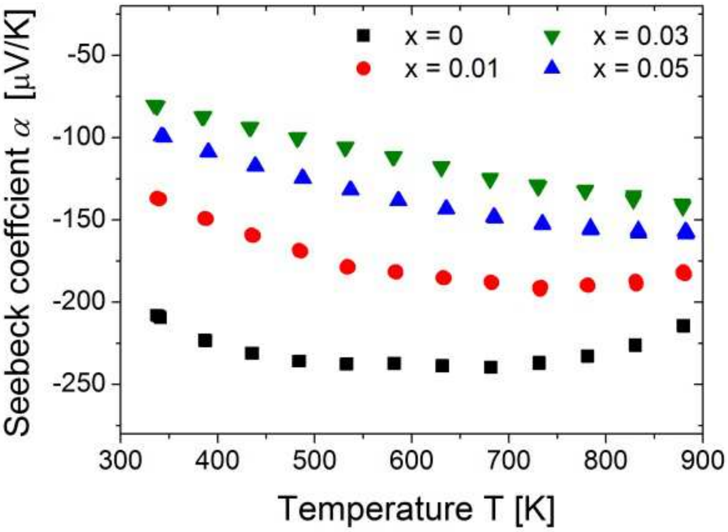

Figure 9.4: Temperature dependence of the Seebeck coefficient α in the $\text{Ti}_{0.3-x}\text{Nb}_x\text{Zr}_{0.35}\text{Hf}_{0.35}\text{NiSn}$ (x = 0, 0.01, 0.03 and 0.05) system from 300 to 900 K [17].

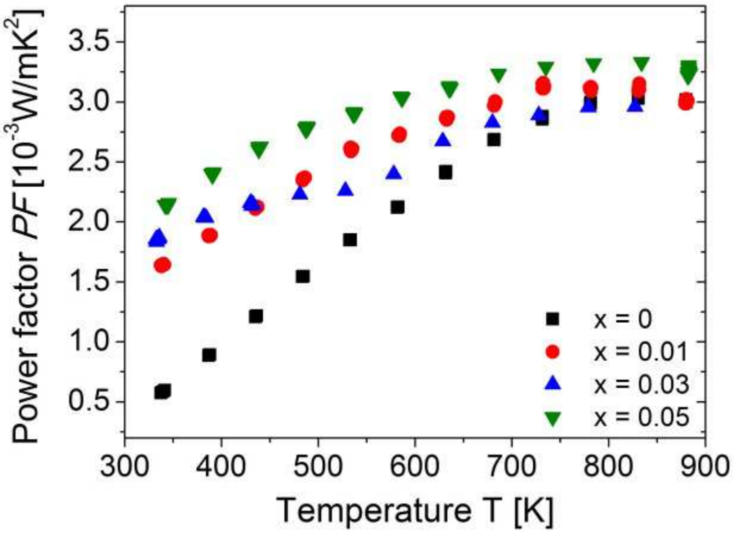

Figure 9.5: Temperature dependence of the power factor $\alpha^2\sigma$ in the $\text{Ti}_{0.3-x}\text{Nb}_x\text{Zr}_{0.35}\text{Hf}_{0.35}\text{NiSn}$ (x = 0, 0.01, 0.03 and 0.05) system from 300 to 900 K [17].

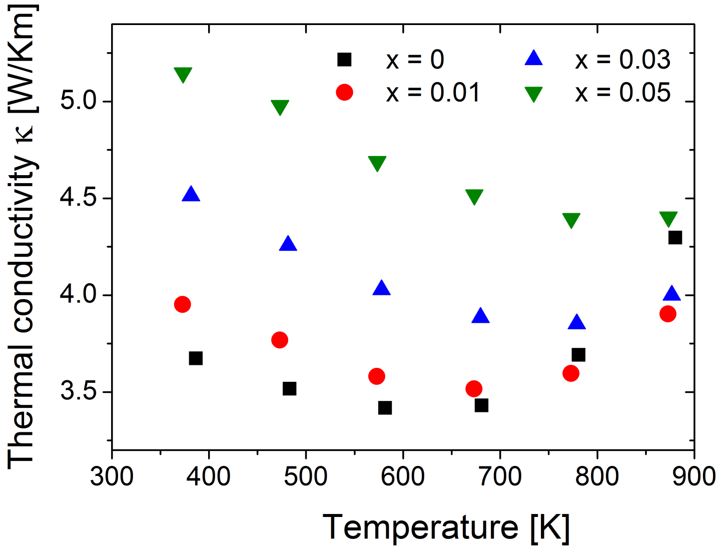

Figure 9.6: Temperature dependence of the thermal conductivity κ in the $Ti_{0.3-x}Nb_xZr_{0.35}Hf_{0.35}NiSn$ (x = 0, 0.01, 0.03 and 0.05) system from 300 to 900 K. It can bee seen that with increasing Nb content, the onset of the bipolar effects are shifted toward higher temperatures [17].

$Ti_{0.3}Zr_{0.35}Hf_{0.35}NiSn$. The aforementioned electron doping of Nb suppresses bipolar conduction, shifting it toward higher temperatures.

The figure of merit, *zT*, was also enhanced with Nb addition (Fig. 9.7). This is an important point, as most improvements in HH compounds are achieved as a result of a drastic reduction in the lattice thermal conductivity. The metal inclusions influence the transport properties strongly because of the introduction of electrons into the HH system, the factor responsible for the significant increase in the electrical conductivity σ. The observed decrease in the absolute Seebeck coefficient does not impact the TE efficiency as dramatically as the increase in the electrical conductivity does. In this study, the highest *zT* obtained was for a Nb concentration of 5%.

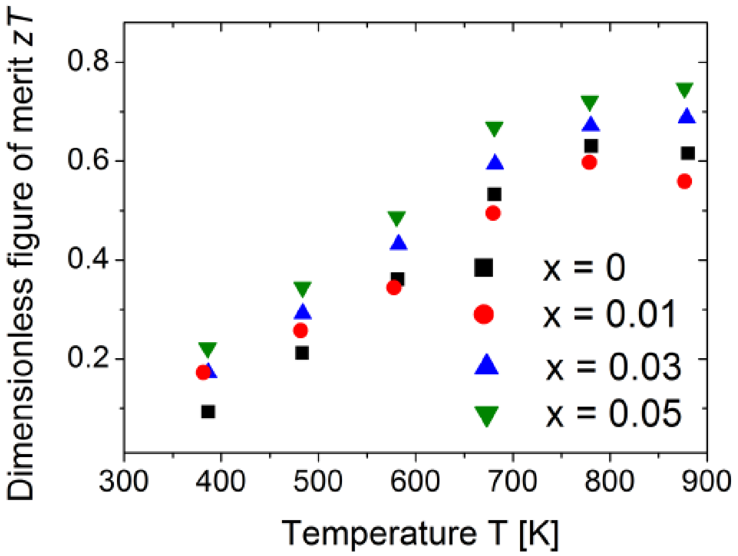

Figure 9.7: The temperature dependence of *zT*, for the $Ti_{0.3-x}Nb_xZr_{0.35}Hf_{0.35}NiSn$ (x = 0, 0.01, 0.03 and 0.05) system from 300 to 900 K [17].

9.3 High temperature Hall measurements of $Ti_{0.3-x}Nb_xZr_{0.35}Hf_{0.35}NiSn$

Fig. 9.8 a) shows the Hall carrier concentration of the $Ti_{0.3-x}Nb_xZr_{0.35}Hf_{0.35}NiSn$ system, which increased significantly with an increase in the Nb concentration. For samples with high Nb content, it could be observed that the carrier concentration remained constant and no intrinsic excitation occurred at high temperatures. The Hall mobility, μ_H (Fig. 9.8 b) decreased with increasing Nb concentration, which may be caused by the scattering of the charge carriers as a result of the additional metal inclusions. The variation in mobility with temperature can be described by a power law equation: $\mu \propto T^{-\nu}$, where the value of ν is an indicator of the most dominant scattering mechanism in the system. For phase-separated HH compounds, Xie *et al.* were able to show that the major mechanism is alloy scattering [23].

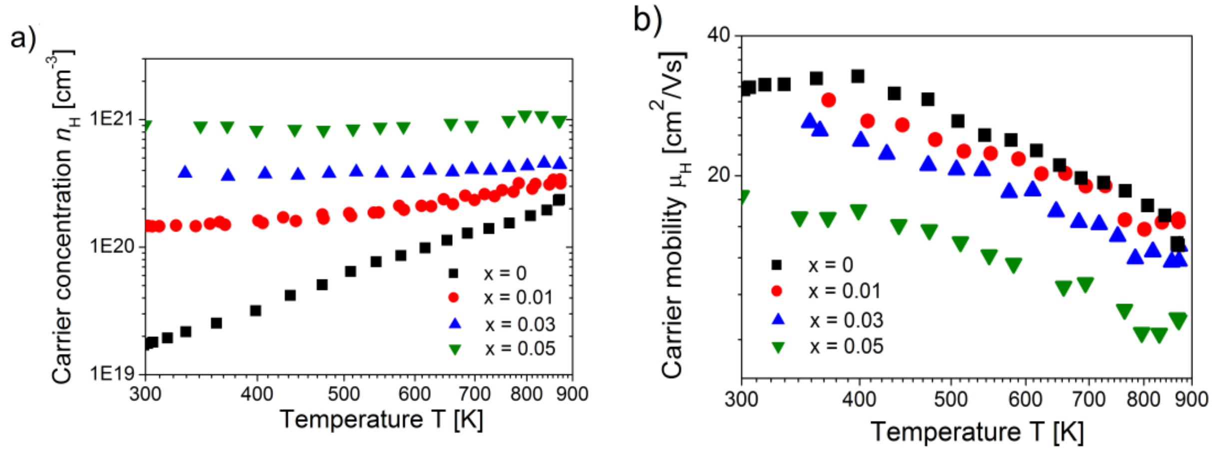

Figure 9.8: Temperature dependence of a) the Hall carrier concentration n_H and b) the Hall mobility μ_H for the $Ti_{0.3-x}Nb_xZr_{0.35}Hf_{0.35}NiSn$ (x = 0, 0.01, 0.03 and 0.05) system from 300 to 900 K [17].

9.4 Modeling the high temperature thermoelectric properties of $Ti_{0.3-x}Nb_xZr_{0.35}Hf_{0.35}NiSn$

The experimental transport data of $Ti_{0.3-x}Nb_xZr_{0.35}Hf_{0.35}NiSn$ (x = 0, 0.01, 0.03 and 0.05) were analyzed using an average effective mass model. To obtain a mean value for the effective mass m^*, it was assumed that electron conduction occurs only within the conduction band for each HH phase. In this theory the Seebeck coefficient and carrier concentration can be calculated from Eq. 6.6 and 6.7 (see section 6.3). It was assumed that, the phonon mean free path is limited by acoustic phonon scattering [84]. The Seebeck coefficient derived from the experimental values versus an optimized carrier concentration is given in Fig. 9.9. For this evaluation, it was assumed that the onset of the contribution of minority carriers sets in above 460 K. Considering this with the calculation from the above mentioned theory, we obtained an average effective mass value of $m^* = 2.1m_e$ for both phases. The agreement between the experimental results [85, 86] and the theoretical calculation justifies the use of an average effective mass model for the estimation of the effective mass and the prediction of the optimum carrier concentration.

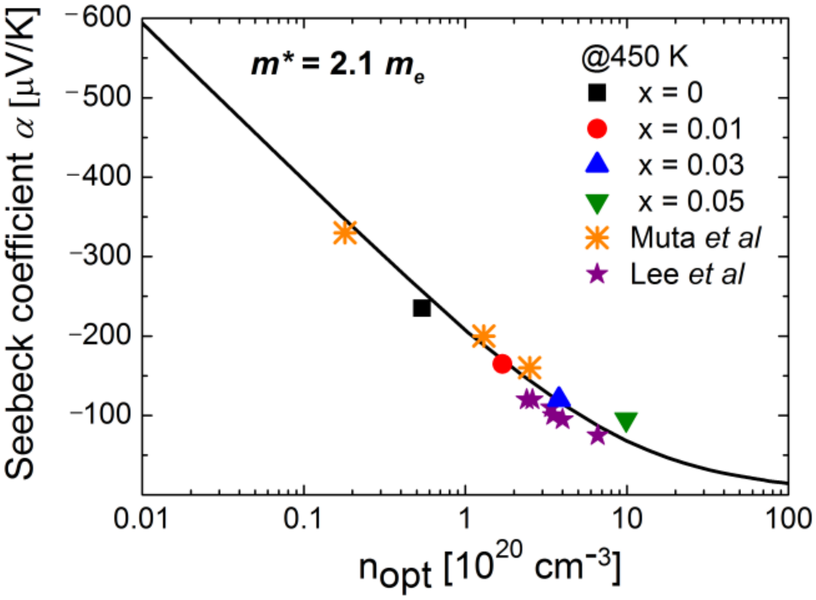

Figure 9.9: Seebeck coefficient, α, *versus* optimized carrier concentration n_{opt} together with a comparison of other Nb subsituted HH compounds [85, 86, 17].

The optimization of *zT* with carrier concentration was confirmed within the framework of the applied model. From the results of the transport measurements, an average effective mass model was developed to determine the optimum carrier concentration. Fig. 9.10 shows that the results obtained are in good agreement with the data presented in the literature [85, 86]. The metallic inclusions generate more electrons in the system which influences the electrical conductivity as well as the magnitude of the Seebeck coefficient, resulting in an enhancement of the power factor (see Fig. 9.5) and leads to an increase of the figure of merit, *zT* (see Fig. 9.7).

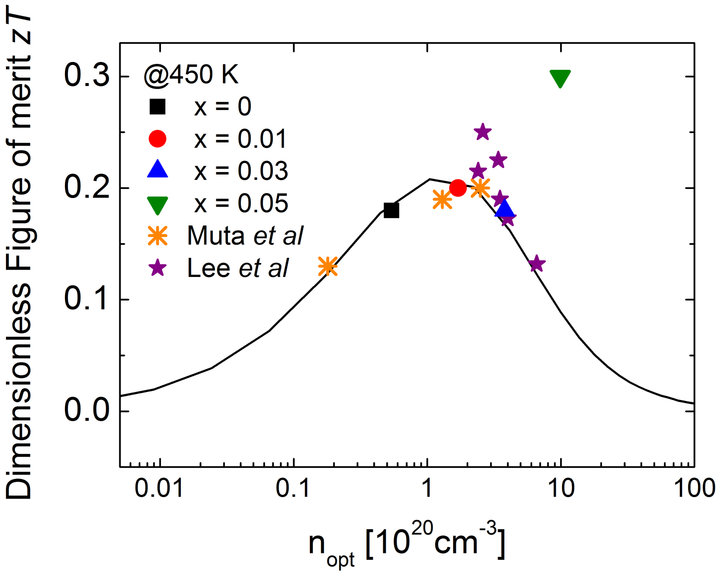

Figure 9.10: Optimized carrier concentration predicted by the average effective mass model for $Ti_{0.3-x}Nb_xZr_{0.35}Hf_{0.35}NiSn$. The triangles and stars represent the values used from [85, 86]. The values for the $Ti_{0.3-x}Nb_xZr_{0.35}Hf_{0.35}NiSn$ system obtained from the transport measurements are color coded. The solid line represents the estimate of the optimized carrier concentration predicted by the average effective mass model, assuming $m^* = 2.1m_e$, $\mu_0 = 25\frac{cm^2}{Vs}$ and $\kappa_l = 3\frac{W}{Km}$ [17].

Conclusions

The thermally stable phase-separated half-Heusler (HH) compounds exhibit excellent thermoelectric performance [77]. The influence of Nb on the high temperature thermoelectric properties on $Ti_{0.3-x}Nb_xZr_{0.35}Hf_{0.35}NiSn$ (x = 0, 0.01, 0.03 and 0.05) was investigated. The obtained results confirmed the exceptional performance of this phase-separated HH materials. The Nb inclusions are responsible for the significant increase in the electrical conductivity and the shift to higher temperatures for the maximum Seebeck coefficient. Both parameters lead to an enhancement of the power factor and the dimensionless figure of merit. To calculate the optimization of zT with carrier concentration, the Boltzmann transport theory was used. From the results of the transport measurements, an average effective mass of $m^* = 2.1m_e$ for both HH phases was calculated, which is in good agreement with the values reported in the literature [85, 86]. These results justify the use of an average effective mass model to describe the carrier transport within the conduction band of these *n*-type HH compounds. The high electron mobility leads to an effective suppression of the bipolar effect in thermoelectric transport properties that is essential for the high zT values in this *n*-type *M*NiSn (*M* = Ti/Zr/Hf) HH compounds [17].

10 Chemical and Physical Models for Engineering Half-Heusler Thermoelectric Materials

10.1 Chemical and Physical models for Engineering half-Heusler Thermoelectric Materials

Theoretical evaluations of the thermoelectric transport properties of half-Heusler alloys from *ab-initio* calculations and the Boltzmann transport theory can be used as an origin for the investigation of existing and new materials [82]. Of more importance for any experimentalist is a layout for analyzing their thermoelectric transport data at any given temperature. Since Jeffery G. Snyder's work [9] a high interest has sparked in the prediction of a materials transport properties within conventional transport theory, which is a powerful tool when analyzing the materials properties. It can be used to guide future work on enhancing and optimizing the thermoelectric efficiency of various systems. By applying a universal model for the transport properties of HH alloys it can be suggested how to enhance these materials to boost their efficiency. The model used is most accurate in the region of a single carrier type and when the Fermi level is situated in a relatively parabolic and isotropic region of the electronic band structure. However, it should be brought to the reader's attention, that there have been many cases where this theory failed, due to multi-band effects [87] or a deviation of a parabolic behavior [61].

For the development of an universal transport theory it is necessary to be in a region where minority carriers can be neglected, before the excitation of intrinsic charge carriers will influence the transport properties at high temperatures. These excitations are revealed through the maximum of the temperature dependent Seebeck-coefficient and for those data sets which showed these maxima around 770 K only their room temperature data were taken into account. In general there is a lack of high temperature data available for the *M*NiSn and *M*CoSb systems. For a better insight on the high temperature behavior of these systesmes, it was assumed that the carrier density is independent of the temperature, where only low temperature Hall data was available, although some thermal activation might occur at high temperatures.

For the development of a transport theory and estimation of the desity of states effective mass m^* Eq. 6.6, 6.7 and 6.8 were used. For simplicity reasons, only acoustic phonon scattering is assumed ($\lambda = 0$), even though recent results by Xie *et al.* [23] suggested, that alloy disorder might play an important role in half-Heusler alloys. From the experimental Seebeck coefficients the chemical potential η can be derived by using eq.n 6.7. And if the carrier concentration n_H is know from Hall measurements m^* can be evaluated as well. From Eq. 6.6-6.9 and by assuming a constant lattice thermal conductivity the figure of merit and the power factor can be calculated as a function of the chemical potential. This method is often used to identifying potentially good thermoelectric materials.

In order to determine μ_H, n_H and m^* sophisticated measurement techniques are usually required. Based on simple Boltzmann statistics, Rowe and Min [88] used a different approach, the so called $\alpha - ln\sigma$ plot as a thermoelectric material performance indicator. This data analysis is also known as Jonker-plot [27]. From the plot Rowe and Min were able to obtain μ_H and m^* indirectly from the measurement of the Seebeck coefficient and the electrical conductivity.The relationship between α and σ is as follows:

$$\alpha = m(b - ln\ \sigma) \tag{10.1}$$

where

$$m = \frac{k}{e} \approx 86.14 \frac{\mu V}{K} \tag{10.2}$$

From Eq. 10.2 it is clear that a plot of α versus ln σ will yield in a straight line, with the slope being *m* and an intercept *b* on the x-axis. Fig. 10.1 shows the room temperature data for several *n*- and *p*-type HH compounds. The slope *m* is not equal to *k/e* and varies for *n*- and *p*-type materials. The values of the interception *b* are 12 or 16 for *p*- and *n*-type HH compounds. The corresponding power factors can be estimated from Fig. 10.1.

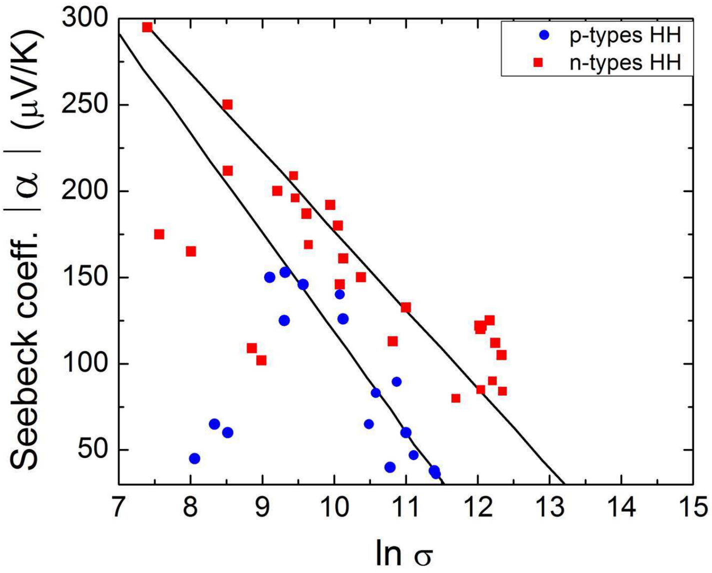

Figure 10.1: $\alpha - ln\sigma$ plot for selected *n*- and *p*-type *M*NiSn and *M*CoSb systems [89, 58, 90, 44, 91, 92, 93, 75, 27, 94].

The optimum electrical conductivity and power factor are given by:

$$\sigma_{opt} = exp(b-2) \tag{10.3}$$

$$(\alpha^2\sigma_{opt})_{max} = 4m^2 exp(b-2) \tag{10.4}$$

The maximum value of the power factor can be determined by the interception derived from a Rowe and Min analysis. For *p*-type samples the maximum value for the power factor is approximately 0.2 mW/K^{2}m and 5 mW/K^{2}m *n*-types at room temperature. For a more detailed discussion on this topic the reader is referred to the work of Rowe and Min [88], as well as the one from Zhu *et al.* [95].

If Hall data is available a transport theory can be used to give a more detailed insight on the dependency of the transport coefficients on the carrier concentration. For half-Heusler alloys the carrier densities lie within the range of 10^{19}- 10^{21} cm^{-3} [23, 46, 19, 96]. From the theory of electrical transport described in many publications the power factor and the figure of merit can be modeled if κ_l, m^* and μ_H of the examined material are known.

The potency of manipulating different sub-lattices in half-Heusler alloys to improve their thermoelectric efficiency and alter their carrier concentration has been demonstrated successfully for several systems [18, 37]. An overview of the most promising alloys and the results from our calculations are shown in Fig. 10.2 and 10.3.

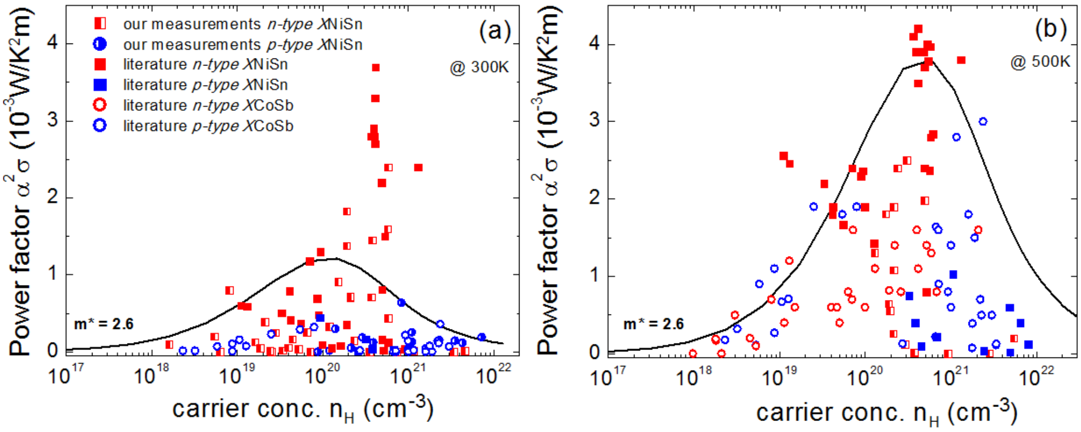

Figure 10.2: Calculated power factors $S^2\alpha$ as a function of carrier concentration for 300 K and 500 K for various *p*- and *n*-type half-Heusler alloys [23, 27, 58, 90, 92, 93, 75, 94, 19, 96]. For the calculation carried out a carrier effective mass m^* of 2.6 m_e for one representative *n*-type HH alloy was used. This value is in good agreement with the results published so far for *n*-type HH materials [27, 44, 37].

Fig. 10.2 shows the computed power factors and experimental data for different half-Heuslers. The power factor is in general a more superior parameter for the comparison of the thermoelectric performances of various materials. Since, both the Seebeck coefficient and the electrical conductivity strongly depend on the carrier density, than the figure of merit where the thermal conductivity κ is involved as well. Whereupon κ is less dependent on the carrier concentration, than on the lattice contribution of the thermal conductivity. Thus, the carrier concentration defining the maximum power factor for a given material is usually close to the one for the maximum *zT*.

The analysis of the data is in good agreement with the results obtained from a Rowe and Min analysis (Fig.10.1). For the $Ti_x(ZrHf)_{0.99-x}V_{0.01}Ni_{0.9}Pd_{0.1}Sn_{0.99}Sb_{0.01}$ solid solution [97] the power factor is ~4 mW/K^{2}m, which is close to the maximum value predicted from Fig. 10.1. The general trend is that *n*-type materials have higher power factors due to their high Seebeck coefficients. The room temperature values of the power factor are very scattered and no clear trend is visible. Some of the HHs, which are assumed to be multi-phase [97, 98, 92, 69], have very high power factors and seem to be an exception. If comparing the room temperature data with the data at 770 K a more distinct trend is visible. The calculated dependency of the power factor versus carrier concentration is less scattered for samples with a low carrier concentration. The highest density of data is accumulated between carrier concentrations of 10^{20} - 10^{21} cm^{-3}. Still the highest values are found for *n*-type HH, where Ti$_x$(ZrHf)$_{0.99-x}$V$_{0.01}$Ni$_{0.9}$Pd$_{0.1}$Sn$_{0.99}$Sb$_{0.01}$ [97] optimizes at $5 * 10^{20}$ cm^{-3}. Research of Culp *et al.* [79] showed that an unusual high content of Sb is able to suppress the effect of bipolar conduction in *n*-type *M*NiSn solid solutions, caused by the small band gap in these HH compounds. The substitution of Sb shifts the maximum of the Seebeck coefficient to higher temperatures with an increase in the electrical conductivity leading to an improvement of the power factor.

Although half-Heusler solid solutions have exceptional large power factors, their potential in thermoelectric applications is damped due to their high thermal conductivities, which is responsible for their relatively low figure of merits *zT*. For these systems usually a large increase in *zT* appears more to be from a significant reduction of the lattice thermal conductivity κ_l than an increase in $\sigma^2 S$. Therefore, many efforts have been ventured to obtain a low thermal conductivity while maintaining high power factors without scattering the charge carriers [75, 94, 99]. Figure 10.3 shows the dependence of the figure of merit *zT* on the carrier concentration for two different temperatures. The experimental data appears to maximize at slightly higher carrier concentrations than predicted by the conventional theory. The data peaking out in this figure are assumed to be multi-phase HHS [97, 98, 92, 69]. For 770 K the optimum carrier concentration is predicted to be $3 * 10^{20}$ cm^{-3}.

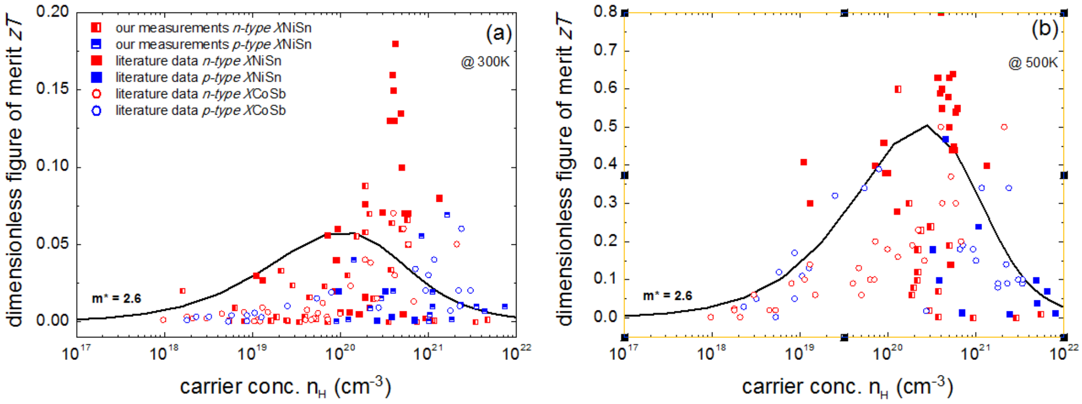

Figure 10.3: Calculated figure of merit *zT* as a function of carrier concentration for 300 K and 500 K for various *p*- and *n*-type half Heusler alloys [23, 27, 58, 90, 92, 93, 75, 94, 19, 96].

From Fig. 10.2 and 10.3 it appears that the description of the dependence of the transport properties on the carrier concentration by using a conventional theory fails. However, Xie *et al.* [23] were able to proof that a dependence on the carrier density can be described by a rigid band approach if other scattering mechanisms are considered as well. Especially for *n*-type half Heuslers alloy scattering seems to play an important role.

The deviation of the transport data from a conventional theory can have various origins. It is well known that HH alloys are prone to impurity phases. This can be caused by different synthesis processes, where the final composition deviates from it's original value, depending on the process [22]. Besides various impurity phases, especially the *M*NiSn system faces the problem of excess Ni, which influence the carrier concentration strongly. Depending on the amount of excess Ni, it will enter the empty sub-lattice to form full Heusler inclusions [100, 101, 102]. Larson *et al.* [38] observed that Ni stabilizes the structure and is responsible of the formation of the band gap, similar to the reports by Pomrehn *et al.* about the phase-stability in thermoelectric Zr_3Sb_4 [103]. Besides this, the deviation of the experimental data from the calculated values for $\sigma^2 S$ and zT can indicate that the electronic conduction occurs either in non-parabolic bands or that it can be dominated by multi-band effects, which is true for the explanation of the transport behavior for *p*-type HH alloys (see chapter 8.1).

Conspicuous, when looking at Fig. 10.2 and 10.3 is also that most of the existing studies on HH alloys focus on the determination of the thermoelectric properties of *n*-type *M*NiSn systems. Studies on *p*-type solid-solutions are far fewer in number. The most promising *p*-type half-Heusler alloy was found within the *M*NiSn system by Schmitt [58] and Krez et al. [77]. It is believed that the substitution of Sc might lead to a high density of states near the Fermi level resulting in a large Seebeck coefficient for these systems. This can be the explanation why Sc seems to be the only sufficient dopant for high *p*-type Seebeck coefficients within the *M*NiSn systems, but with their high thermal conductivities only low figure of merits are achieved [44]. The general problem is that *M*NiSn alloys have small band gaps (see Fig. 5.11), where the onset of bipolar conduction limits the transport in these systems especially for *p*-types. As described in chapter 7.2.2 their transport properties are dominated by higher mobile electrons causing extremely low carrier mobilities. More promising are the investigations of *p*-types in the *M*CoSb half Heusler alloys. As published by Yan *et al.* [89] the highest peak zT for *p*-type HH was found in the $Zr_{0.5}Hf_{0.5}CoSb_{0.8}Sn_{0.2}$ solid solution. Still the problem of the low mobilities for *p*-types remains [90].

In conclusion it can be said that most recent trend to improve the thermoelectric performance of various thermoelectric materials, has been a nano-structure approach. This approach has gained success not only in the class of HH materials, but also for other thermoelectric materials like PbTe [104] and BiTeSe [11, 105]. Due to nano-structuring [41] or intrinsic phase separations [92, 97], the thermoelectric performance of half-Heuslers could be enhanced by significantly decreasing the thermal conductivity. Work by Yu *et al.* [106] shows that a further reduction of the thermal conductivity is still possible, as long as the Cahill limit is not reached. The concept of nano-structuring provides a good start for improving HH alloys beyond their bulk limits. So the solution might lie in the controlled synthesis of thermally stable multi-phase HH compounds.

Other approaches to improve the thermoelectric performance have been explored by Pei and Snyder *et al.* [25]. They used the approach of band structure engineering in PbTe, such as the distortion of the DOS for PbTe with Tl [107]. Also a possibility might be the introduction of resonant levels, which has already worked for PbTe based systems [108]. In half-Heusler V-doped $\mathrm{Hf_{0.75}Zr_{0.25}NiSn}$ was investigated by Simonson *et al.* [27]. Also other transition metal dopants could prove themselves as a successful strategy to improve the thermoelectric performance of HH and other thermoelectric materials. The general focus for improving thermoelectric HH alloys, should be laid on controlling their synthesis and with that their carrier concentrations. Work done by Snyder *et al.* showed, that a careful control of the carrier concentration leads to an optimization of the overall thermoelectric performance, especially for $\mathrm{Bi_2Te_3}$ [9]. It is therefore very important to understand and investigated the electron and phonon transport features. It seems, that the inevitably connection of the Seebeck coefficient and electrical conductivity will lead to a compromise between a large thermopower and a high electrical conductivity to maximize the thermoelectric figure of merit, zT. As the evaluation of the literature data showed (Fig. 10.2 and 10.3) a conventional theory was not able to describe the dependence on the carrier concentration for all investigated HH alloys. The theory however describes well the behavior for *n*-type HH according to the results of chapter 9 and to Xie *et al.* [23], where the conduction of the majority carrier takes place in the conduction band and the influence of the minority carriers is neglectable. For an accurate evaluation of the transport properties in *p*-type half-Heusler alloys, where the transport is dominated by the higher mobile electrons [58], the higher effective mass of the valance band as well as multi-band effects have to be considered. For example, the determination of the chemical potential requires the knowledge of the exact value for the band gap, the electronic band features for the holes and electrons and the carrier concentration of the extrinsic dopant. Therefore, an advanced transport theory needs to be developed for the appropriate description of the transport properties for *p*-type materials. The overview of zT versus carrier concentration (Fig. 10.3) at room temperature for the *M*NiSn and *M*CoSb solid solution should provide a guideline to undertake research in the field of carrier optimization. It seems that the optimum carrier concentration and therefore the maximum zT and power factors are different for the two solid solutions, due to their difference in the band gap of 0.5 eV.

It is important to continue the efforts to understand and optimize the transport in *M*NiSn and *M*CoSb alloys. The focus should be laid on synthesis, sample purity and the enhancement of the electrical transport while maintaining a low thermal conductivity. A chemical manipulation will help to enhance their performance due to alloy or point defect scattering [23]. And again, the approach of an artificially induced thermally stable phase separation can turn out to be the key to raise their thermoelectric performance above known limits.

11 Summary and Outlook

Half-Heusler (HH) compounds with the general formula *M*NiSn (M = Ti, Zr, Hf) are a promising class of materials for thermoelectric applications because of their high Seebeck coefficients [18, 19] and the possibilities for compositional variations at each of the three lattice sites. Besides, HH are comprised of earth abundant elements, giving them a cost advantage over conventional thermoelectric materials.

Much of the existing literature on HH deals with thermoelectric characterization of *n*-type *M*NiSn and *p*-type *M*CoSb solid solutions. Studies on *p*-type *M*NiSn-based HHs are far fewer in number. To fabricate high efficient thermoelectric modules based on HH, high performance *p*-type *M*NiSn systems need to be developed that are compatible with the existing *n*-type HH [43]. This thesis explores synthesis strategies for *p*-type *M*NiSn based alloys. In particular, the efficacy of transition metals (Sc, La) and main group elements (Al, Ga, In) as acceptor dopants on the Sn-site in ZrNiSn, was investigated by evaluating their thermoelectric performance.

The introduction of main group acceptor dopants like Ga or In resulted in a change in the nature of conduction in ZrNiSn from *n*- to *p*-type. The best *p*-type, using main group acceptors, was achieved for 1 at.% Ga, where a Seebeck coefficient of $+65$ μV/K at 150 K could be reached. However, the onset of bipolar conduction above 150 K reduced the effective carrier mobility and led to a subsequent increase in the electrical resistivity. This led to a decreased thermoelectric efficiency of Ga/In doped *M*NiSn-based samples. The substitution of Al for Sn was not successful either, since Al segregated as metal inclusions and decreased of the Seebeck coefficient. In effect, substitution with main group elements did not result in acceptable p-type materials for high temperature applications, since all samples showed a roll-over in the Seebeck coefficient below room temperature.

Turning to transition metals, the substitution of Zr by Sc resulted in a high temperature *p*-type HH, making it the most promising one for further investigation. The Seebeck coefficient was positive (on account of hole conduction) and increased with increasing temperature, reaching a maximum of $+115$ μV/K at 650 K. This is the highest value reached for the *p*-types in ternary HH compounds so far. With further increase in temperature, the concentration of electrons - possessing higher mobility - started to increase, which led to a rollover thereafter. Apart from Sc, high temperature *p*-types have been achieved by other groups using Y [18, 56, 55] and Co for Ni [44]. Thus, transition metals seem to be the most efficient dopants to achieve high temperature *p*-types.

The band gaps for Sc substituted samples were obtained from S_{max} using the Goldschmid-Sharp formula. The values, however, deviated significantly from the band gap obtained through optical measurements (0.13 eV) and from *ab intio* calculations (0.5 eV) [28]. The discrepancy was explained by a large difference of the mobility between electrons and holes. The obtained results confirmed that the narrow band gap in NiSn-based HH compounds is the reason for the early onset of bipolar conduction, resulting in low *zT* values for *p*-type materials and that the high mobility of the electrons is responsible for the inhibition of the early onset of bipolar conduction (< 500 K). This is the reason, why *n*-type HH are successful TE materials for high temperature applications.

N-type $Ti_{0.5}Zr_{0.25}Hf_{0.25}NiSn$ exhibit an intrinsic phase separation into two HH phase (a Zr-Hf rich primary phase and a Ti-rich secondary phase). The phase separation causes a distinct reduction of the total thermal conductivity and leads to high TE efficiencies in phase-separated HH. The fact that Sc is a great *p*-dopant was applied to this phase-separated system. Which already possess a great TE efficiency with the aim to gain a high efficient *p*-type. Thus, a Seebeck coefficient of $+190$ μV/K was achieved for 4 at.% Sc substitution at 650 K, the highest value for a *p*-type reported in this thesis. It is striking that the Seebeck coefficient for phase-separated samples is almost twice as high as for the ternary HH compounds, and that a much lesser acceptor substitution level led to this result compared to the ternary system.

To complement the experimental investigations on different metal dopants and their influence on the TE properties of HH compounds, numerical solutions to the Boltzmann transport equation were used to predict the optimum carrier concentration where the maximum TE efficiency occurs for *p*-type HH. The results for Sc substituted ternary and phase-separated samples showed that the conduction band of HH treated within single parabolic band (SPB) model deviates strongly from the experimental data above 500 K, indicating the onset of bipolar effects and the invalidity of a SPB model for *p*-type HH. From Hall Effect measurements it was known that the transport properties of *p*-type HH are dominated by the high mobility of the electrons. Thus, a two band model was employed for a more accurate prediction of the optimum carrier concentration. Within this theory both, CB and VB, were treated as parabolic bands.

The results showed that even a two band model approach is insufficient to describe the transport properties of *p*-type HH. The parabolic band model is commonly used for bulk TE materials. It is most accurate when the transport properties are dominated by one single carrier type and when the Fermi energy is situated within a relatively parabolic region of the band structure. Neither is true in the case of *p*-type HH, since the transport is dominated by two carrier types and the VB can not be assumed to be parabolic. Even though the VB does not fulfill the requirements to use the two band model, the CB can be assumed as being parabolic. Since the transport properties of *n*-type HH is dominated by only one carrier type, the use of a parabolic model should lead to a successful description of the transport properties. To this end, the influence of Nb on the thermoelectric properties of $\text{Ti}_{0.3-x}\text{Nb}_x\text{Zr}_{0.35}\text{Hf}_{0.35}\text{NiSn}$ (x = 0, 0.01, 0.03 and 0.05) was investigated. In this compound Nb does not enter the lattice and segregates out as metal inclusions homogenously distributed through both HH phases. Thus, the Nb inclusions are responsible for a significant increase in the carrier concentration, the electrical conductivity and a shift of the maximum Seebeck coefficient to higher temperatures. This lead to an enhancement of the *zT* (0.78 at 900 K) as well as the power factor. To optimize *zT* with carrier concentration, a universal transport theory was used to describe this phase-separated system. Based on transport measurements, an average effective mass of $m^* = 2.1m_e$ for both HH phases was calculated, in good agreement with the values reported in the literature for ternary HH [85, 86]. These results justify the use of a universal transport theory to predict the optimum carrier concentration at which the best TE performance occurs. It also confirmed that only one type of carrier is responsible for the transport properties within a parabolic conduction band for *n*-type HH. The high electron mobility of *n*-type HH leads to an effective suppression of the bipolar effects, which is essential for the high *zT* values in this *n*-type *M*NiSn (*M* = Ti/Zr/Hf) HH compounds. The model thus provides the prediction of the optimum carrier concentration for *n*-type $\text{Ti}_{0.3-x}\text{Zr}_{0.35}\text{Hf}_{0.35}\text{NiSn}$ compounds.

The transport theory was also used to compare various *n*- and *p*-type HH compounds found in the literature and to identify trends in carrier concentration and TE efficiencies. It was found (figure 10.2 and 10.3) that a simple theory is not able to describe the dependence on the carrier concentration for all HH compounds investigated. The results indicated that the optimum carrier concentration and thus the maximum *zT* and power factor are different for NiSn- and CoSb-based HH compounds, due to their difference in the band gap of 0.5 eV and CB.

Thus, to improve the accuracy of the prediction of the transport properties, especially for *p*-type HH, a higher effective mass of the VB, bipolar effects and multiple bands have to be considered. This could be achieved by applying the Kane band model, which takes the non-parabolicity of the triply degenerate CB into account lead to a better evaluation of the optimum carrier concentration of *p*-type HH.

It is important to continue the efforts to understand the complex electronic and phononic transport parameters in ternary HH to further engineer more promising HH, like the phase-separated systems with their proven temperature stability [77, 17, 56]. In order to be able to understand the role and influence of the dopant on the transport properties the local structure should be examined more closely. Techniques such as X-ray absorption fine structure spectroscopy (EXAFS) could reveal important information about the degree of disorder in HHs, the local structure around a dopant and how these features manifest for transition metals *versus* main group dopants. Thus, a systematic study of the correlation between the band structure and the dopant through ab initio calculations could provide fundamental insights at an atomistic scale, which is difficult to obtain through conventional thermoelectric characterization tools. Total energy calculations based on DFT could also provide thermodynamically favorable lattice sites for different dopants.

Bibliography

[1] J. H. Goldsmid. *Introduction to thermoelectrics*. Springer, Heidelberg, 2010.

[2] A. J. Minnich, M. S. Dresselhaus, Z. F. Ren, and G. Chen. Bulk nanostructured thermoelectric materials: current research and future prospects. *Energy Environ. Sci.*, 2:466–479, 2009.

[3] F. Casper, T. Graf, S. Chadov, B. Balke, and C. Felser. Half-heusler compounds: novel materials for energy and spintronic applications. *Semiconductor Science and Technology*, 27(6):063001, 2012.

[4] C. Mahan, B. Sales, and J. Sharp. Thermoelectric materials: New approaches to an old problem. *Physics Today*, 50:42–47, 1997.

[5] A. F. Ioffe. *Semiconductor Thermoelements and Thermoelectric Cooling*.

[6] G. J. Snyder. *Thermoelectrics Handbook: Macro to Nano, Chapter 9*. CRC Press, New York, 2005.

[7] Terry M. Tritt and M. A. Subramanian. Thermoelectric materials, phenomena, and applications: A bird's eye view. *MRS Bulletin*, 31:188–198, 3 2006.

[8] JPL Agrum A. and NASA website. Voyager the interstellar mission.

[9] G. J. Snyder and E. S. Toberer. Complex thermoelectric materials. *Nat Mater*, 7, 2008.

[10] M˙ Functionally graded materials for sensor and energy applications. *Materials Science and Engineering: A*, 362(12):17 – 39, 2003. Papers from the German Priority Programme (Functionally Graded Materials).

[11] Joseph P. Heremans, Vladimir Jovovic, Eric S. Toberer, Ali Saramat, Ken Kurosaki, Anek Charoenphakdee, Shinsuke Yamanaka, and G. Jeffrey Snyder. Enhancement of thermoelectric efficiency in pbte by distortion of the electronic density of states. *Science*, 321(5888):554–557, 2008.

[12] P. Larson, S. D. Mahanti, J. Salvador, and M. G. Kanatzidis. Electronic structure of the ternary zintl-phase compounds zr$_3$ni$_3$sb$_4$, hf$_3$ni$_3$sb$_4$, and zr$_3$pt$_3$sb$_4$ and their similarity to half-heusler compounds such as zrnisn. *Phys. Rev. B*, 74:035111, Jul 2006.

[13] P. H. M. Bẗtger, G. S. Pomrehn, G. J. Snyder, and T. G. Finstad. Doping of p-type znsb: Single parabolic band model and impurity band conduction. *physica status solidi (a)*, 208(12):2753–2759, 2011.

[14] S. R. Elliot. *The Physics and Chemistry of Solids*. John Wiley & Sons: Chister, 1998.

[15] H. J. Goldsmid J. R. Drabble. *Thermal conductions in Semmiconductors*. Pergamon Press, New York, 1961.

[16] Alexandra Zevalkink. *Chain-Forming Zintl Antimonides as Novel Thermoelectric Materials*. PhD thesis, California Institute of Technology Pasadena, California, 2013.

[17] J. Krez, J. Schmitt, G.J. Synder, C. Felser, W. Hermes, and M. Schwind. Optimization of the carrier concentration in phase-separated half-heusler compounds. *accepted*, 2014.

[18] C. Uher, J. Yang, S. Hu, D. T. Morelli, and G. P. Meisner. Transport properties of pure and doped mnisn (m=zr, hf). *Phys. Rev. B*, 59:8615–8621, Apr 1999.

[19] Slade R. Culp, J. W. Simonson, S. Joseph Poon, V. Ponnambalam, J. Edwards, and Terry M. Tritt. (zr,hf)co(sb,sn) half-heusler phases as high-temperature p-type thermoelectric materials. *Applied Physics Letters*, 93(2):–, 2008.

[20] W. Xie, A. Weidenkaff, W. Tang, Q. Zhang, J. Poon, and T.M. Tritt. Recent advances in nanostructured thermoelectric half-heusler compounds. *Nanomaterials*, (2):379–412, 2012.

[21] Tanja Graf, Claudia Felser, and Stuart S.P. Parkin. Simple rules for the understanding of heusler compounds. *Progress in Solid State Chemistry*, 39(1):1 – 50, 2011.

[22] Shuo Chen and Zhifeng Ren. Recent progress of half-heusler for moderate temperature thermoelectric applications. *Materials Today*, 16(10):387 – 395, 2013.

[23] Hanhui Xie, Heng Wang, Yanzhong Pei, Chenguang Fu, Xiaohua Liu, G. Jeffrey Snyder, Xinbing Zhao, and Tiejun Zhu. Beneficial contribution of alloy disorder to electron and phonon transport in half-heusler thermoelectric materials. *Advanced Functional Materials*, 23(41):5123–5130, 2013.

[24] S.K. Mishra, S. Satpathy, and O. Jepsen. Electronic structure and thermoelectric properties of bismuth telluride and bismuth selenide. *Journal of Physics: Condensed Matter*, 9(2):461, 1997.

[25] Y. Pei, X. Shi, A. LaLonde, H. Wang, L. Chen, and G. J. Snyder. Convergence of electronic bands for high performance bulk thermoelectrics. *Nature*, 473(66), 2011.

[26] J. P. Heremans, B. Wiendlocha, and A. M. Chamoire. Resonant levels in bulk thermoelectric semiconductors. *Energy Environ. Sci.*, 5:5510–5530, 2012.

[27] J. W. Simonson, D. Wu, W. J. Xie, T. M. Tritt, and S. J. Poon. Introduction of resonant states and enhancement of thermoelectric properties in half-heusler alloys. *Phys. Rev. B*, 83:235211, Jun 2011.

[28] S. Ouardi, G. H. Fecher, B. Balke, X. Kozina, G. Stryganyuk, C. Felser, S. Lowitzer, D. Ködderitzsch, H. Ebert, and E. Ikenaga. Electronic transport properties of electron- and hole-doped semiconducting c1b heusler compounds: Niti1-xmxsn (m=sc,v). *Phys. Rev. B*, 82:085108, Aug 2010.

[29] G. Slack. *CRC Handbook of Thermoelectrics*. 1995.

[30] G. S. Nolas, G. Fowler, and J. Yang. Assessing the role of filler atoms on the thermal conductivity of filled skutterudites. *Journal of Applied Physics*, 100(4):–, 2006.

[31] S. B. Schujman, G. S. Nolas, R. A. Young, C. Lind, A. P. Wilkinson, G. A. Slack, R. Patschke, M. G. Kanatzidis, M. Ulutagay, and S.-J. Hwu. Structural analysis of sr8ga16ge30 clathrate compound. *Journal of Applied Physics*, 87(3), 2000.

[32] Tunable multifunctional topological insulators in ternary heusler compounds. *nature mater.*, 9:541 – 545, 2010.

[33] S. Ouardi, G. H. Fecher, C. Felser, M. Schwall, S. S. Naghavi, A. Gloskovskii, and B. Balke. Electronic structure and optical, mechanical, and transport properties of the pure, electron-doped, and hole-doped heusler compound cotisb. *Phys. Rev. B*, 86:045116, Jul 2012.

[34] F.G. Aliev, N.B. Brandt, V.V. Moshchalkov, V.V. Kozyrkov, R.V. Skolozdra, and A.I. Belogorokhov. Gap at the fermi level in the intermetallic vacancy system rbisn(r=ti,zr,hf). *Zeitschrift fr Physik B Condensed Matter*, 75(2):167–171, 1989.

[35] H. Xie, J. Mi, L. Hu, N. Lock, M. Chirstensen, C. Fu, B. B. Iversen, X.-B. Zhao, and T.-J. Zhu. Interrelation between atomic switching disorder and thermoelectric properties of zrnisn half-heusler compounds. *CrystEngComm*, 14:4467–4471, 2012.

[36] S. Sakurada and N. Shutoh. Effect of ti substitution on the thermoelectric properties of (zr,hf)nisn half-heusler compounds. *Applied Physics Letters*, 86(8):–, 2005.

[37] Cui Yu, Tie-Jun Zhu, Rui-Zhi Shi, Yun Zhang, Xin-Bing Zhao, and Jian He. High-performance half-heusler thermoelectric materials hf1-x zrxnisn1-ysby prepared by levitation melting and spark plasma sintering. *Acta Materialia*, 57(9):2757 – 2764, 2009.

[38] P. Larson, S. D. Mahanti, and M. G. Kanatzidis. Structural stability of ni-containing half-heusler compounds. *Phys. Rev. B*, 62:12754–12762, Nov 2000.

[39] Michael Schwall and Benjamin Balke. Phase separation as a key to a thermoelectric high efficiency. *Phys. Chem. Chem. Phys.*, 15:1868–1872, 2013.

[40] X. Yan, Weishu Liu, Hui Wang, Shuo Chen, Junichiro Shiomi, Keivan Esfarjani, Hengzhi Wang, Dezhi Wang, Gang Chen, and Zhifeng Ren. Stronger phonon scattering by larger differences in atomic mass and size in p-type half-heuslers hf1-xtixcosb0.8sn0.2. *Energy Environ. Sci.*, 5:7543–7548, 2012.

[41] S. Populoh, M.H. Aguirre, O.C. Brunko, K. Galazka, Y. Lu, and A. Weidenkaff. High figure of merit in (ti,zr,hf)nisn half-heusler alloys. *Scripta Materialia*, 66(12):1073 – 1076, 2012. Viewpoint Set no. 50: Twinning Induced PlasticitySteels.

[42] Jihui Yang and T. Caillat. Thermoelectric materials for space and automotive power generation. *MRS Bulletin*, 31:224–229, 3 2006.

[43] S. Populoh, o. C. Brunko, K. Galazka, W. Xie, and A. Weidenkaff. Half-heusler (tizrhf)nisn unileg module with high powder density. *Materials*, 6(4):1326–1332, 2013.

[44] Han-Hui Xie, Cui Yu, Bin He, Tie-Jun Zhu, and Xin-Bing Zhao. Thermoelectric properties and n- to p-type conversion of co-doped zrnisn-based half-heusler alloys. *Journal of Electronic Materials*, 41(6):1826–1830, 2012.

[45] A Horyn, O Bodak, L Romaka, Yu Gorelenko, A Tkachuk, V Davydov, and Yu Stadnyk. Crystal structure and physical properties of (ti,sc)nisn and (zr,sc)nisn solid solutions. *Journal of Alloys and Compounds*, 363(12):10 – 14, 2004.

[46] G. Joshi, X. Yan, H. Wang, W. Liu, G. Chen, and Z. Ren. Enhancement in thermoelectric figure-of-merit of an n-type half-heusler compound by the nanocomposite approach. *Advanced Energy Materials*, 1(4):643–647, 2011.

[47] Wenjie Xie, Qiao Jin, and Xinfeng Tang. The preparation and thermoelectric properties of ti0.5zr0.25hf0.25co1-xnixsb half-heusler compounds. *Journal of Applied Physics*, 103(4):–, 2008.

[48] Siham Ouardi, Gerhard H. Fecher, Claudia Felser, Christian G. F. Blum, Dirk Bombor, Christian Hess, Sabine Wurmehl, Bernd Bchner, and Eiji Ikenaga. Transport and thermal properties of single- and polycrystalline nizr0.5hf0.5sn. *Applied Physics Letters*, 99(15):–, 2011.

[49] Kasper A. Borup, Eric S. Toberer, Leslie D. Zoltan, George Nakatsukasa, Michael Errico, Jean-Pierre Fleurial, Bo B. Iversen, and G. Jeffrey Snyder. Measurement of the electrical resistivity and hall coefficient at high temperatures. *Review of Scientific Instruments*, 83(12):–, 2012.

[50] Shiho Iwanaga, Eric S. Toberer, Aaron LaLonde, and G. Jeffrey Snyder. A high temperature apparatus for measurement of the seebeck coefficient. *Review of Scientific Instruments*, 82(6):–, 2011.

[51] H. Hecht W. Wendlandt. *Reflectance spectroscopy*. Interscience, New York, 1966.

[52] G. Jeffery Snyder Andrew F. May. Introduction to modeling thermoelectric transport at high temperatures.

[53] W. Jeitschko. Transition metal stannides with mgagas and mncu2al type structure. *Metallurgical Transactions*, 1(11):3159–3162, 1970.

[54] K. Ikeda, R. Fletcher, J. C. Maan, and J. Kossut. Thermopower, entropy, and the mott relation in hgse:fe. *Phys. Rev. B*, 65:035201, Dec 2001.

[55] Jens OOestereich. *Untersuchungen an neuen thermoelektrischen Materialien*. PhD thesis, Universität Konstanz, Konstanz, Germany, 2011.

[56] Julia Krez. *Thermoelectric properties in phase-separated half-Heusler materials*. PhD thesis, Johannes Gutenberg-Universität, Mainz, Germany, 2014.

[57] E.K. Hlil, Yu Stadnyk, Yu Gorelenko, L. Romaka, A. Horyn, and D. Fruchart. Synthesis, electronic transport and magnetic properties of zr1-xyxnisn, (x=00.25) solid solutions. *Journal of Solid State Chemistry*, 183(3):521 – 526, 2010.

[58] J. Schmitt, Z. M. Gibbs, G. J. Snyder, and C. Felser. Resolving the true band gap of zrnisn half-heusler thermoelectric materials. *submitted*.

[59] Yoshisato Kimura, Toshiyasu Tanoguchi, and Takuji Kita. Vacancy site occupation by co and ir in half-heusler zrnisn and conversion of the thermoelectric properties from n-type to p-type. *Acta Materialia*, 58(13):4354 – 4361, 2010.

[60] J L Wang, H Wang, G J Snyder, X Zhang, Z H Ni, and Y F Chen. Characteristics of lattice thermal conductivity and carrier mobility of undoped pbse-pbs solid solutions. *Journal of Physics D: Applied Physics*, 46(40):405301, 2013.

[61] A. F. Ravich, B. A. Efimova, and I. A. Smirnow. *Semiconducting Lead Chalcogenides*. Plenum, New York, 1970.

[62] V.A. Romaka, Yu.V. Stadnyk, M.G. Shelyapina, D. Fruchart, V.F. Chekurin, L.P. Romaka, and Yu.K. Gorelenko. Specific features of the metal-insulator conductivity transition in narrow-gap semiconductors of the mgagas structure type. *Semiconductors*, 40(2):131–136, 2006.

[63] E. H. Putley. *The hall effect and its applications*. Contemporary Physics, 1975.

[64] Christopher M. Jaworski, Michele D. Nielsen, Hsin Wang, Steven N. Girard, Wei Cai, Wally D. Porter, Mercouri G. Kanatzidis, and Joseph P. Heremans. Valence-band structure of highly efficient p-type thermoelectric pbte-pbs alloys. *Phys. Rev. B*, 87:045203, Jan 2013.

[65] H.J. Goldsmid and J.W. Sharp. Estimation of the thermal band gap of a semiconductor from seebeck measurements. *Journal of Electronic Materials*, 28(7):869–872, 1999.

[66] Z.M. Gibbs, A. LaLonde, and G.J. Snyder. Optical band gap and the bursteinmoss effect in iodine doped pbte using diffuse reflectance infrared fourier transform spectroscopy. *New Journal of Physics*, 15(7):075020, 2013.

[67] J. Tauc. Optical properties and electronic structure of amorphous ge and si.

[68] C. Yu, H. Xie, C. Fu, T. Zhu, and X. Zhao. High performance half-heusler thermoelectric materials with refined grains and nanoscale precipitates. *Journal of Materials Research*, 27:2457–2465, 10 2012.

[69] Sung-Wng Kim, Yoshisato Kimura, and Yoshinao Mishima. High temperature thermoelectric properties of tinisn-based half-heusler compounds. *Intermetallics*, 15(3):349 – 356, 2007.

[70] L. D. Zhao, H. J. Wu, S. Q. Hao, C. I. Wu, X. Y. Zhou, K. Biswas, J. Q. He, T. P. Hogan, C. Uher, C. Wolverton, V. P. Dravid, and M. G. Kanatzidis. All-scale hierarchical thermoelectrics: Mgte in pbte facilitates valence band convergence and suppresses bipolar thermal transport for high performance. *Energy Environ. Sci.*, 6:3346–3355, 2013.

[71] Hicks L. D. and Dresselhaus M. S. Thermoelectric figure of merit of a one-dimensional conductor. *Physical review. B, Condensed matter*, 47(24):16631–16634, 1993. eng.

[72] Yi Ma, Richard Heijl, and AndersE.C. Palmqvist. Composite thermoelectric materials with embedded nanoparticles. *Journal of Materials Science*, 48(7):2767–2778, 2013.

[73] Weishu Liu, Xiao Yan, Gang Chen, and Zhifeng Ren. Recent advances in thermoelectric nanocomposites. *Nano Energy*, 1(1):42 – 56, 2012.

[74] Julien P. A. Makongo, Dinesh K. Misra, Xiaoyuan Zhou, Aditya Pant, Michael R. Shabetai, Xianli Su, Ctirad Uher, Kevin L. Stokes, and Pierre F. P. Poudeu. Simultaneous large enhancements in thermopower and electrical conductivity of bulk nanostructured half-heusler alloys. *Journal of the American Chemical Society*, 133(46):18843–18852, 2011.

[75] W.J. Xie, J. He, S. Zhu, X.L. Su, S.Y. Wang, T. Holgate, J.W. Graff, V. Ponnambalam, S.J. Poon, X.F. Tang, Q.J. Zhang, and T.M. Tritt. Simultaneously optimizing the independent thermoelectric properties in (ti,zr,hf)(co,ni)sb alloy by in situ forming insb nanoinclusions. *Acta Materialia*, 58(14):4705 – 4713, 2010.

[76] C. Yu, H. Xie, C. Fu, T.J. Zhu, and X. Zhao. High performance half-heusler thermoelectric materials with refined grains and nanoscale precipitates. *Journal of Materials Research*, 27:2457–2465, 10 2012.

[77] J. Krez, B. Balke, C. Felser, W. Hermes, and M. Schwind. Long term stability of phase separated half-heusler compounds. *to be published*.

[78] Cui Yu, Tie-Jun Zhu, Kai Xiao, Jun-Jie Shen, Sheng-Hui Yang, and Xin-Bing Zhao. Reduced grain size and improved thermoelectric properties of melt spun (hf,zr)nisn half-heusler alloys. *Journal of Electronic Materials*, 39(9):2008–2012, 2010.

[79] Slade R. Culp, S. Joseph Poon, Nicoleta Hickman, T.M. Tritt, and J. Blumm. Effect of substitutions on the thermoelectric figure of merit of half-heusler phases at 800c. *Applied Physics Letters*, 88(4):042106–042106–3, Jan 2006.

[80] Michael Schwall and Benjamin Balke. Phase separation as a key to a thermoelectric high efficiency. *Phys. Chem. Chem. Phys.*, 15:1868–1872, 2013.

[81]

[82] Jiong Yang, Huanming Li, Ting Wu, Wenqing Zhang, Lidong Chen, and Jihui Yang. Evaluation of half-heusler compounds as thermoelectric materials based on the calculated electrical transport properties. *Advanced Functional Materials*, 18(19):2880–2888, 2008.

[83] Tanja Graf, Joachim Barth, Christian G. F. Blum, Benjamin Balke, Claudia Felser, Peter Klaer, and Hans-Joachim Elmers. Phase-separation-induced changes in the magnetic and transport properties of the quaternary heusler alloys. *Phys. Rev. B*, 82:104420, Sep 2010.

[84] Eric S. Toberer, Alex Zevalkink, and G. Jeffrey Snyder. Phonon engineering through crystal chemistry. *J. Mater. Chem.*, 21:15843–15852, 2011.

[85] Hiroaki Muta, Takanori Kanemitsu, Ken Kurosaki, and Shinsuke Yamanaka. High-temperature thermoelectric properties of nb-doped Mnisn (m = ti, zr) half-heusler compound. *Journal of Alloys and Compounds*, 469(12):50 – 55, 2009.

[86] Ping-Jen Lee and Long-Sun Chao. High-temperature thermoelectric properties of ti0.5(zrhf)0.5-xnbxni0.9pd0.1sn0.98sb0.02 half-heusler alloys. *Journal of Alloys and Compounds*, 504(1):192 – 196, 2010.

[87] D. J. Singh and I. I. Mazin. Calculated thermoelectric properties of la-filled skutterudites. *Phys. Rev. B*, 56:R1650–R1653, Jul 1997.

[88] D.M. Rowe and Gao Min. a-in s plot as a thermoelectric material performance indicator. *Journal of Materials Science Letters*, 14(9):617–619, 1995.

[89] Xiao Yan, Giri Joshi, Weishu Liu, Yucheng Lan, Hui Wang, Sangyeop Lee, J. W. Simonson, S. J. Poon, T. M. Tritt, Gang Chen, and Z. F. Ren. Enhanced thermoelectric figure of merit of p-type half-heuslers. *Nano Letters*, 11(2):556–560, 2011.

[90] V. Ponnambalam, Paola N. Alboni, J. Edwards, T.M. Tritt, Slade R. Culp, and S. Joseph Poon. Thermoelectric properties of p-type half-heusler alloys $\mathrm{zr}_{1-x}\mathrm{ti}_x\mathrm{cosn}_y\mathrm{sb}_{1-y}$($0.0 \ll x \ll 0.5$; y = 0.15 and 0.3). *Journal of Applied Physics*, 103(6):063716–063716–5, Mar 2008.

[91] M. Zhou, C. Feng, L. Chen, and X. Huang. Effects of partial substitution of co by ni on the high-temperature thermoelectric properties of ticosb-based half-heusler compounds. *Journal of Alloys and Compounds*, 391(12):194 – 197, 2005.

[92] Ping-Jen Lee and Long-Sun Chao. High-temperature thermoelectric properties of ti0.5(zrhf)0.5-xnbxni0.9pd0.1sn0.98sb0.02 half-heusler alloys. *Journal of Alloys and Compounds*, 504(1):192 – 196, 2010.

[93] M. Zhou, L. Chen, C. Feng, D. Wang, and J.-F. Li. Moderate-temperature thermoelectric properties of ticosb-based half-heusler compounds $\mathrm{ti}_{1-x}\mathrm{ta}_x\mathrm{cosb}$. *Journal of Applied Physics*, 101(11):–, 2007.

[94] P. Maji, J. Makongo, X. Zhou, H. Chi, C. Uher, and P. Poudeu. Thermoelectric performance of nanostructured p-type zr0.5hf0.5co0.4rh0.6sb1-xsnx half-heusler alloys. *Journal of Solid State Chemistry*, 202(0):70 – 76, 2013.

[95] Q. Zhu, E. M. Hopper, B. J. Ingram, and T. O. Mason. Combined jonker and ioffe analysis of oxide conductors and semiconductors. *Journal of the American Ceramic Society*, 94(1):187–193, 2011.

[96] T. Wu, W. Jiang, X. Li, S. Bai, S. Liufu, and L. Chen. Effects of ge doping on the thermoelectric properties of ticosb-based p-type half-heusler compounds. *Journal of Alloys and Compounds*, 467(12):590 – 594, 2009.

[97] P. Lee, S. Tseng, and L. Chao. High-temperature thermoelectric properties of tix(zrhf)0.99-xv0.01ni0.9pd0.1sn0.99sb0.01 half-heusler alloys. *Journal of Alloys and Compounds*, 496(12):620 – 623, 2010.

[98] Various p- and n-type half-heusler solid solutions.

[99] W.J. Xie, Y.G. Yan, S. Zhu, M. Zhou, S. Populoh, K. Galazka, S.J. Poon, A. Weidenkaff, J. He, X.F. Tang, and T.M. Tritt. Significant zt enhancement in p-type ti(co,fe)sbinsb nanocomposites via a synergistic high-mobility electron injection, energy-filtering and boundary-scattering approach. *Acta Materialia*, 61(6):2087 – 2094, 2013.

[100] C. S. Birkel, J. E. Douglas, B. R. Lettiere, G. Seward, N. Verma, Y. Zhang, T. M. Pollock, R. Seshadri, and G. D. Stucky. Improving the thermoelectric properties of half-heusler tinisn through inclusion of a second full-heusler phase: microwave preparation and spark plasma sintering of tini$_{1+x}$sn. *Phys. Chem. Chem. Phys.*, 15:6990–6997, 2013.

[101] V.V. Romaka, P. Rogl, L. Romaka, Y. Stadnyk, A. Grytsiv, O. Lakh, and V. Krayovskii. Peculiarities of structural disorder in zr- and hf-containing heusler and half-heusler stannides. *Intermetallics*, 35(0):45 – 52, 2013.

[102] H. Hazama, M. Matsubara, R. Asahi, and T. Takeuchi. Improvement of thermoelectric properties for half-heusler tinisn by interstitial ni defects. *Journal of Applied Physics*, 110(6):–, 2011.

[103] G. S. Pomrehn, E. S. Toberer, G. J. Snyder, and A. van de Walle. Entropic stabilization and retrograde solubility in zn4sb3. *Phys. Rev. B*, 83:094106, Mar 2011.

[104] B. Poudel, Q. Hao, Y. Ma, Y. Lan, A. Minnich, B. Yu, X. Yan, D. Wang, A. Muto, D. Vashaee, X. Chen, J. Liu, M. S. Dresselhaus, G. Chen, and Z. Ren. High-thermoelectric performance of nanostructured bismuth antimony telluride bulk alloys. *Science*, 320(5876):634–638, 2008.

[105] P. F. P. Poudeu, J. D'Angelo, H. Kong, A. Downey, J. L. Short, R. Pcionek, T. P. Hogan, C. Uher, and M. G. Kanatzidis. Nanostructures versus solid solutions:? low lattice thermal conductivity and enhanced thermoelectric figure of merit in pb9.6sb0.2te10-xsex bulk materials. *Journal of the American Chemical Society*, 128(44):14347–14355, 2006.

[106] C. Yu, T.-J. Zhu, K. Xiao, J.-J. Shen, S.-H. Yang, and X.-B. Zhao. Reduced grain size and improved thermoelectric properties of melt spun (hf,zr)nisn half-heusler alloys. *Journal of Electronic Materials*, 39(9):2008–2012, 2010.

[107] X. Shi, J. Yang, S. Bai, J. Yang, H. Wang, M. Chi, J. R. Salvador, W. Zhang, L. Chen, and W. Wong-Ng. On the design of high-efficiency thermoelectric clathrates through a systematic cross-substitution of framework elements. *Advanced Functional Materials*, 20(5):755–763, 2010.

[108] K. Ahn, M.-K. Han, J. He, J. Androulakis, S. Ballikaya, C. Uher, V. P. Dravid, and M. G. Kanatzidis. Exploring resonance levels and nanostructuring in the pbte-cdte system and enhancement of the thermoelectric figure of merit. *Journal of the American Chemical Society*, 132(14):5227–5235, 2010. PMID: 20235578.